MODAL DECOMPOSITION OF THERMAL CONDUCTANCE

A Dissertation
Presented to
The Academic Faculty

by

Kiarash Gordiz

In Partial Fulfillment
of the Requirements for the Doctor of Philosophy in the
Mechanical Engineering

Georgia Institute of Technology
May 2017

MODAL DECOMPOSITION OF THERMAL CONDUCTANCE

Approved by:

Dr. Asegun Henry, Advisor
George W. Woodruff School of Mechanical Engineering,
Georgia Institute of Technology

Dr. Shannon Yee
George W. Woodruff School of Mechanical Engineering,
Georgia Institute of Technology

Dr. Kurt Wiesenfeld
School of Physics
Georgia Institute of Technology

Dr. Samuel Graham
George W. Woodruff School of Mechanical Engineering,
Georgia Institute of Technology

Dr. Martin Maldovan
School of Chemical and Biomolecular Engineering
Georgia Institute of Technology

Date Approved: [01/01/2017]

To my parents

ACKNOWLEDGEMENTS

Firstly, I would like to express my sincere gratitude to my advisor Prof. Asegun Henry for the continuous support of my PhD study and for his patience, kindness, and immense knowledge. His guidance helped me in all the time of research and writing of this thesis, and his passion for science helped me learn to always be hopeful and stay focused on my dreams even if the path forward is challenging. I could not have imagined having a better advisor and mentor for my PhD study.

Besides my advisor, I would like to thank the rest of my thesis committee: Prof. Samuel Graham, Prof. Kurt Wiesenfeld, Prof. Shannon Yee, and Prof. Martin Maldovan for their insightful comments and encouragement, but also for the valuable questions which incented me to widen my research from various perspectives.

My sincere thanks also go to Misha Rodin and Sampath Kommandur from Prof. Shannon Yee's group, Luke Yates from Prof. Samuel Graham's group, and Dr. Thomas Bougher from Prof. Baratunde Cola's group, who helped us in our efforts to experimentally measure the interface conductance using various techniques.

I also sincerely thank all my past and present fellow labmates in Atomistic Simulation & Energy (ASE) Laboratory, Dr. Diane England, Dr. Cansheng Yuan, Dr. Wei Lv, Colby Jarrett, Freddy DeAngelis, Greg Wilk, Hamidreza Seyf, Drew Rohskopf, Caleb Amy, Malavika Bagepalli, and Daniel Budenstien for the stimulating discussions, for the long nights we were working or studying together before deadlines or exams, and for all the fun we had in the last five years

Last, but not least, I would like to thank my parents for their endless love and continuous support as I could not be even close to receiving my PhD in Mechanical Engineering from Georgia Tech if I did not have their presence in my life.

TABLE OF CONTENTS

LIST OF TABLES

LIST OF FIGURES

LIST OF SYMBOLS AND ABBREVIATIONS

$\hbar$	Planck's constant divided by 2π
k_B	Boltzmann's constant
ω	Frequency of the mode of vibration
k	Phonon wave vector
λ	Phonon wave length
v_g	Phonon group velocity
τ	Phonon lifetime
l	Phonon mean free path
f	Phonon distribution function
τ_{AB}	Phonon transmission probability between materials A and B
G	Thermal interface conductance
K	Thermal conductivity
Q	Instantaneous interfacial heat flux
T	Temperature
A	Interface cross-section area
N	Total number of atoms in the system
$\mathbf{f}_{ij}$	Pairwise exchanged force between atoms i and j
Φ	Potential energy
H	Hamiltonian
$\mathbf{p}$	Atom momentum

$\mathbf{x}$	Atom displacement
$\dot{\mathbf{x}}$	Atom velocity
X	Modal displacement coordinate
$\dot{X}$	Modal velocity coordinate
m	Atomic mass
$\mathbf{e}_{n,i}$	eigen vector for mode n assigning the direction and displacement magnitude of atom i
C	Heat capacity per volume
v	Particle velocity
n	Particle concentration
c	Phonon (particle) heat capacity
j	net flux of energy in the system
MD	Molecular dynamics
EMD	Equilibrium molecular dynamics
NEMD	Non-equilibrium molecular dynamics
TIR	Thermal interface resistance
TIC	Thermal interface conductance
TC	Thermal conductivity
PGM	Phonon gas model
WP	Wave packet
DMM	Diffuse mismatch model
AMM	Acoustic mismatch model
FC	Force constant

SUMMARY

Reliably and quantitatively calculating the conductance of phonons across an interface between two materials has been one of the major unresolved questions in thermal transport physics for the last century. Theories have been presented in this regard, but their predictive power is limited. In this thesis, a new formalism to extract the modal contributions to thermal interface conductance, termed interface conductance modal analysis (ICMA) is developed. ICMA can fully include the temperature dependent anharmonicity and atom level topography around the interface in the calculations. In addition, compared to all the previous techniques that are based on the phonons gas model (PGM) and can only be applied to crystalline interfaces, ICMA is not based on preexisting assumptions; thus, it can be applied to the interface of disordered/amorphous solids as well.

The obtained results indicate that when two materials are joined a new set of vibrational modes are required to correctly describe the transport across the interface. The new set of vibrational modes is inconsistent with the physical picture described by the PGM, because some of the most important modes are localized and non-propagating and therefore do not have a well-defined velocity nor do they impinge on the interface. Among these new modes, certain classifications emerge, as most modes extend at least partially into the other material. Localized interfacial modes are also present and exhibit a high conductance contribution on a per mode basis by strongly coupling to other types of vibrational modes. ICMA formalism is applied to different interfaces to present thermal interface conductance accumulation functions, two-dimensional cross-correlation matrices, and a quantitative determination of the contributions arising from inelastic

effects. Moreover, the results show that ICMA present a physical explanation for interfacial heat transafer that is based on correlation and that is different and independent of the dominant scattering viewpoint followed by the PGM. The provided new perspective on interface thermal transport can open new gates towards deeper understanding of phonon-phonon and electron-phonon interactions around interfaces.

CHAPTER 1. INTRODUCTION: THE THEORY OF PHONON TRANSPORT ACROSS INTERFACES

When heat flows across an adjoining interface between two different materials there will be a temperature discontinuity at the interface (see Figure 1). The interfacial heat flow (Q), can be written as the product of the thermal interface conductance (TIC), denoted by G, which is the inverse of the thermal interface resistance (TIR), and the temperature difference across the interface (ΔT) (*i.e.*, $Q = G\Delta T$). Interfaces play a key role in the thermal behavior of nanostructures.[1,2] Due to tremendous advances in nanostructuring in recent years,[3,4] exquisite structures with characteristic lengths on the order of nanometers can be fabricated for applications in nanoelectronics [5] and nanoscale energy conversion.[1] In these small scales, interfaces can become the dominant resistance to heat transfer, which on one side impedes the progress towards achieving improved performance in nano-electronics,[6] nano-optoelectronics,[7] or energy conversion devices such as multi-junction solar cells,[8,9] and on the other side sets interface engineering as a promising path to reach higher ZT thermoelectric materials through reducing thermal conductivity (e.g., by making grain boundaries [10] or superlattices [10]).

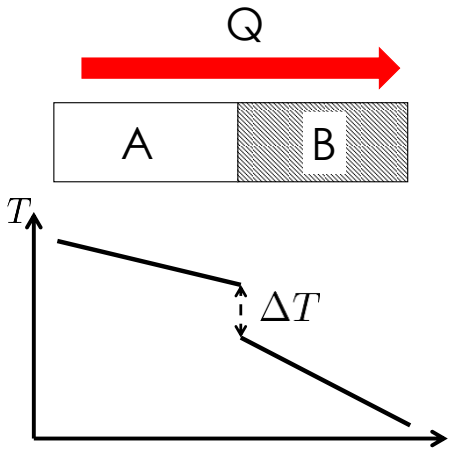

Figure 1 – Heat flow (Q) causes a temperature jump (ΔT) at the interface of two solid materials labeled A and B. Q is proportional to ΔT, and the constant of proportionality is the interface conductance G (*i.e.*, $Q = G\Delta T$).

The heat flow across the interface can be carried primarily by electrons in electrically conducting materials, but the contribution from the atomic motions is present in all materials. For solids and rigid molecules, these atomic motions correspond to vibrations around an equilibrium site, which can be decomposed into a series of eigen modes via the lattice dynamics (LD) formalism [11] where the actual anharmonic (*i.e.*, inelastic) dynamics manifest as the modes having time varying amplitudes. At a given instant, by knowing the amplitudes of these eigen modes of vibration, one can sum the contributions of all the different eigen modes to recover the vibrations of each atom.[11] The eigen modes are termed phonons in crystalline materials, since they generally correspond to propagating waves such as sound waves. However, in disordered/amorphous solids or molecules many eigen modes may not propagate or resemble the usual definition of a phonon. This has prompted our use of the term eigen mode in the presented thesis to retain generality.

Since the first experimental observations of TIR,[12,13] different theoretical models have been proposed to explain the transfer of heat across interfaces and to predict TIC.[22-25,27,28,36] The acoustic mismatch model (AMM),[14,15] the diffuse mismatch model (DMM),[16-18] the atomistic Green's function (AGF) approach,[19-23] the harmonic LD based approaches,[24-26] wave packet (WP) method,[27-30] and frequency domain perfectly matched layer (FD-PML) method [31,32] are notable examples of these models. Although each of these techniques is devised for different sets of operating conditions (*e.g.*, temperature range, interface quality, etc.), they are all based on the phonon gas model (PGM) and usually invoke some version of the Landauer formalism.[33-35]

1.1 Phonon gas model

The Fourier's law of heat conduction, proposed in 1822 by Joseph Fourier,[36,37] defines the thermal conductivity (K) of a solid with respect to the steady flow of heat along the specimen (j) and the imposed temperature gradient $\left(dT/dx\right)$ using the following formula,

$$j = -K\frac{dT}{dx} \tag{1}$$

The above equation is a solution to the diffusion equation, which based on the mathematical descriptions for Markov process [38] is a manifestation that thermal energy transfer in solid materials is based on a random process. To describe this random transfer of energy in solid materials, in 1929, Peierls [39] introduced the main idea of the PGM. According to the PGM, similar to gas molecules contained in a vessel (see Figure 2) that exhibit random

movements and collisions (*i.e.*, Brownian motion),[40] the modes of vibration in a solid material (*i.e.*, phonons) can also be envisioned as travelling quasi-particles, where they have associated velocities, direction of movement and can get scattered by other phonons.

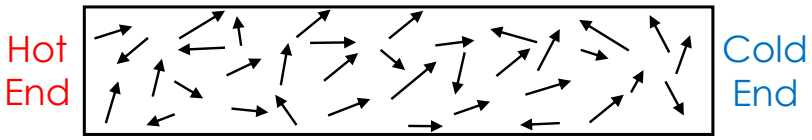

Figure 2 – Gas molecules contained in a vessel under a temperature gradient. The thermal conductivity for such a system can be described by kinetic theory of gases (see Eq. (2)).

After assuming the general similarity between gas molecules and phonons, PGM likens the energy transfer by phonons in solid materials to energy transfer by gas molecules, too. Energy transfer by gas molecules can be explained by elementary kinetic gas theory.[41] The thermal conductivity of a gas inside a vessel can be expressed as,

$$K = \frac{1}{3} C v l \tag{2}$$

where C is the heat capacity per unit volume, v is the average particle velocity, and l is the mean free path of a particle between collisions with other particles. Equation (2) can be derived using elementary kinetic theory.[34,41] The flux of particles along the x-direction is $\frac{1}{2} n \langle |v_x| \rangle$, where n is the concentration of molecules, and $\langle \cdots \rangle$ shows the averaged value. Coefficient $1/2$ comes from the fact that in equilibrium there is a flux of equal magnitude in the opposite direction. If c is the heat capacity of one particle, then by moving

from a region with temperature $T+\Delta T$ to another region with temperature T, a particle will release $c\Delta T$ energy. At the end of a free path of particle, ΔT can be written as,

$$\Delta T = \frac{dT}{dx} l_x = \frac{dT}{dx} v_x \tau \tag{3}$$

where τ is the average time between collisions. The net flux of energy in the system is

$$\begin{aligned} j &= \left(\frac{1}{2} n \left\langle |v_x| \right\rangle\right) c \left(-\frac{dT}{dx} v_x \tau\right) - \left(\frac{1}{2} n \left\langle |v_x| \right\rangle\right) c \left(\frac{dT}{dx} v_x \tau\right) \\ &= -n \left\langle {v_x}^2 \right\rangle c\tau \frac{dT}{dx} = -\frac{1}{3} n \left\langle v^2 \right\rangle c\tau \frac{dT}{dx} \end{aligned} \tag{4}$$

If we consider constant propagation velocity for all phonons, Eq. (4) can be written as,

$$j = -\frac{1}{3} Cvl \frac{dT}{dx} \tag{5}$$

Considering $l \equiv v\tau$ and $C \equiv nc$, $K = \frac{1}{3} Cvl$ can be obtained. Equation (5) describes the net flux of energy by gas molecules, and according to PGM it can be readily modified to explain energy transfer by phonons. This is possible if one replaces the velocity (v), heat capacity (c), and concentration of the particles in Eq. (5) with the phonon group velocity (v_g), phonon energy $(\hbar\omega)$, and phonon distribution function (*e.g.*, Bose-Einstein distribution function denoted by f), respectively. Here, $\hbar$ is Planck's constant divided by 2π, and ω is the frequency of vibration. The result would be the net heat flux transfer by phonons and can be written as,

$$j \propto f\left(\hbar\omega\right) v_g l \frac{dT}{dx} \tag{6}$$

Equation (6) is the cornerstone for all the PGM based models that are utilized to explain heat transfer in solid materials. The main difference between these models, however, is how each model calculates the mean free path of different phonons.

When it comes to interfacial heat transfer, the PGM follows a similar viewpoint formulated in Eq. (6), where it depicts phonons as travelling quasi-particles with energies ($\hbar\omega$) and well-defined velocities, which are determined by the group velocity (v_g), that are incident on the interface. According to the PGM, the incident phonons on the interface undergo scattering events (see Figure 3 for a schematic representation of this idea). By accounting for these scattering events, the Landauer formalism then describes interfacial heat flux in terms of what fraction of the energy of each incident phonon is transmitted to the other side of the interface. Mathematically, the Landauer formalism for phonon heat flux going from material A to material B is formulated as,[16,33]

$$Q_{A\to B} = \sum_{p_A}\left[\frac{1}{V_A}\sum_{k_{x,A}=-k_{max}}^{k_{max}}\sum_{k_{y,A}=-k_{max}}^{k_{max}}\sum_{k_{z,A}=0}^{k_{max}} v_{z,A}\hbar\omega\tau_{AB} f(\omega,T_A)\right] \tag{7}$$

where the summations are performed over different polarizations (p) and allowed wave vectors ($k_{x,y,z}$) in material A so that only phonons with velocities incident on the interface are counted,[33] and in addition to $\hbar$ and ω which were previously defined, V_A is the volume of side A, $v_{z,A}$ is the phonon group velocity normal to the interface, τ is the transmission

probability for the mode of vibration, T is the temperature, and f is the Bose-Einstein distribution function. The net heat flux from material A into material B is the difference of the two,

$$Q = \sum_{p_A}\left[\frac{1}{V_A}\sum_{k_{x,A}=-k_{max}}^{k_{max}}\sum_{k_{y,A}=-k_{max}}^{k_{max}}\sum_{k_{z,A}=0}^{k_{max}} v_{z,A}\hbar\omega\tau_{AB} f(\omega,T_A)\right] - \sum_{p_B}\left[\frac{1}{V_B}\sum_{k_{x,B}=-k_{max}}^{k_{max}}\sum_{k_{y,B}=-k_{max}}^{k_{max}}\sum_{k_{z,B}=0}^{k_{max}} v_{z,B}\hbar\omega\tau_{BA} f(\omega,T_B)\right] \tag{8}$$

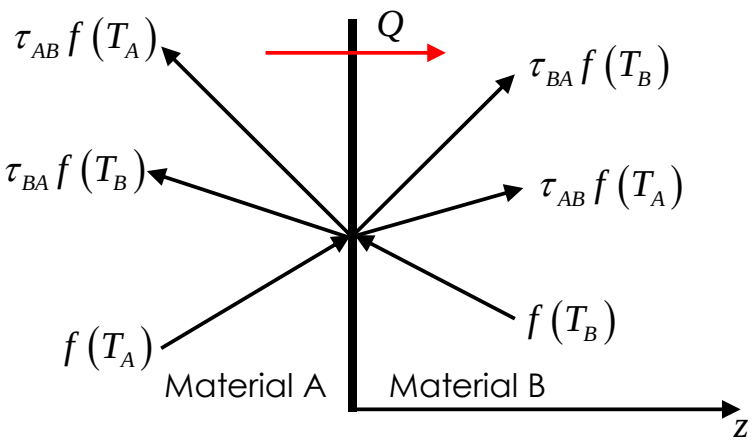

Figure 3 – Scattering of incident phonons (transmission and reflection) at the interface of two materials A and B.

At thermal equilibrium (*i.e.*, $T_A = T_B$), the net heat flux is zero, so that

$$\sum_{p_A}\left[\frac{1}{V_A}\sum_{k_{x,A}=-k_{max}}^{k_{max}}\sum_{k_{y,A}=-k_{max}}^{k_{max}}\sum_{k_{z,A}=0}^{k_{max}} v_{z,A}\hbar\omega\tau_{AB} f(\omega,T_A)\right] = \sum_{p_B}\left[\frac{1}{V_B}\sum_{k_{x,B}=-k_{max}}^{k_{max}}\sum_{k_{y,B}=-k_{max}}^{k_{max}}\sum_{k_{z,B}=0}^{k_{max}} v_{z,B}\hbar\omega\tau_{BA} f(\omega,T_A)\right] \tag{9}$$

The above equation is an instance of detailed balance, which requires that no heat flux crosses the interface if the system is at equilibrium. Using Eq. (9) we can rewrite Eq. (8) as,

$$Q = \sum_{p_A} \left[\frac{1}{V_A} \sum_{k_{x,A}=-k_{max}}^{k_{max}} \sum_{k_{y,A}=-k_{max}}^{k_{max}} \sum_{k_{z,A}=0}^{k_{max}} v_{z,A} \hbar\omega \tau_{AB} \left[f(\omega, T_A) - f(\omega, T_B) \right] \right] \tag{10}$$

The above formula shows that, using the principle of detailed balance, the Landauer formalism can describe the interfacial heat flux with properties of only one of the two materials and with transmission probably. When the difference between T_A and T_B is small, using the definition of $Q = G\left(T_A - T_B\right)$, Eq. (10) can be written as,

$$G = \sum_{p_A} \left[\frac{1}{V_A} \sum_{k_{x,A}=-k_{max}}^{k_{max}} \sum_{k_{y,A}=-k_{max}}^{k_{max}} \sum_{k_{z,A}=0}^{k_{max}} v_{z,A} \hbar\omega \tau_{AB} \frac{df(\omega, T)}{dT} \right] \tag{11}$$

It should be noted that in the Landauer formulation (Eq. (11)), v_g needs to be calculated for all modes of vibration in the system and rigorously, such a calculation is only possible for crystalline solids. Therefore, application of PGM based methods to the interfaces of amorphous materials and alloys is highly questionable, since v_g cannot be defined for most of the vibrational modes, as most of the modes of vibration in amorphous materials are not of propagating nature.[42-47] This situation has limited the application of the PGM based methods to the interface of crystalline solids.

The reason that v_g cannot be defined for most of the modes in alloyed and amorphous materials can be understood from its definition. Qualitatively, v_g is the velocity

based on which any phase in a travelling wave moves. For instance, the velocity according to which the pinnacle of a wave travels in a medium (*e.g.*, the pinnacles of waves generated after throwing a stone in a stationary water) is equal to the v_g for that wave (see Figure 4). Mathematically, v_g for a mode of vibration can be dined as,

$$v_g = \frac{\partial \omega}{\partial k} \tag{12}$$

where ω and k are frequency and wave vector (*i.e.*, proportional to the inverse of wave length (see Figure 4)) for the mode of vibration, respectively. Equation (12) shows that v_g is a measure for the degree of variation in frequency for the mode of vibration with respect to its wave vector. Therefore, the calculation of v_g for a mode of vibration in the system requires well-defined definitions for both frequency and wave vector for that mode of vibration. Frequency is a characteristic for all the modes of vibration in the system and can be calculated using LD. However, as Seyf and Henry discuss in a recent study,[48] most of the vibrational modes in alloyed and amorphous solids do not have well-defined wave vectors which consequently makes the definition of group velocity for them impossible.

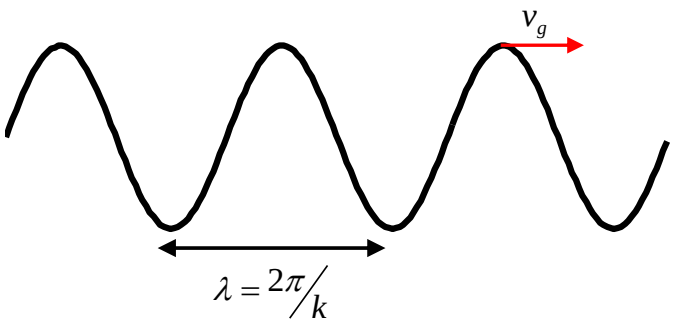

Figure 4 – Schematic representation of group velocity (v_g) and wave vector (k) for a travelling wave. Wave length (λ) measures the distance between two equal phases in travelling wave (*e.g.*, the distance between two pinnacles).

Despite being only applicable to crystalline interfaces, the main difference between all the PGM based techniques such as AMM, DMM, AGF, and WP method is how the transmission probability (τ) for the incident phonon on the interface is calculated. The AMM and DMM take the limit of purely specular and diffuse scattering respectively. Many improvements have been made to these methods,[16,49-53] but neither can include the atomic level detail of the interface quality (*e.g.*, roughness, interatomic diffusion, stress, imperfections etc.) and therefore they are fundamentally limited. The development of the AGF method was a major step forward, as it incorporated the atomic level details and also accounts for quantum effects.[22,54] However, most applications of the AGF method have been limited to small system sizes and harmonic interactions, due to analytical complexity and computational expense.[22] Mingo nonetheless has shown that, in principle, anharmonicity can be included in the AGF.[22] To our knowledge, however, the anharmonic AGF has not yet been widely used. Although exceptions exist,[55] the majority of the literature using DMM have also only been able to evaluate elastic scattering interactions where the transmission of a mode's energy across the interface is purely governed by whether or not other modes with similar frequency exist on the other side of the

interface.[1,23] The WP method allows the calculation of a mode's transmissivity in the context of a molecular dynamics (MD) simulation, however, it requires that all other modes have zero amplitude.[22,54,56,57] This effectively corresponds to the $T = 0K$ limit and therefore is unable to examine the effects of temperature dependent anharmonicity. As a result, the WP method simply reproduces the same results as the harmonic AGF approach.[1]

1.2 The importance of anharmonicity

Within the last decade, techniques have been developed to accurately calculate the individual eigen mode contributions to TC from first principles.[58-60] These techniques now allow for predictive calculations of the modal contributions to thermal conductivity (TC) for materials and nanostructures that have yet to be synthesized.[61,62] Compared to the tremendous advancements in predicting TC for crystalline materials over the last decade, predicting TIC still faces many challenges. The central issue is that we lack quantitative understanding of the underlying processes that occur at interfaces, because we currently have no way of determining the modal contributions with full inclusion of anharmonicity. Interactions/coupling of modes of vibration with different frequencies is the result of anharmonicity.

To better understand anharmonicity, we need to first define lattice energy. Lattice energy of a solid structure is the energy of formation for the structure from infinitely separated atoms. The origin for lattice energy is the interaction between all the atoms in the system, and it can be theoretically calculated from electronic calculations. Using force constants (FC), which are defined as derivate of the potential energy with respect to atomic

displacements about their equilibrium positions, lattice energy can be written as summation of all the atom-atom interactions,[63]

$$V = V_0 + \sum_i \Pi_i u_i + \frac{1}{2!}\sum_{ij} \Phi_{ij} u_i u_j + \frac{1}{3!}\sum_{ijk} \Psi_{ijk} u_i u_j u_k + \frac{1}{4!}\sum_{ijkl} \chi_{ijkl} u_i u_j u_k u_l \tag{13}$$

where indexes i, j, k, l refer to triplets defined by (R, τ, α), with R being a translation vector pointing to a primitive basis in the lattice, τ being an atom within that primitive basis, and α being the Cartesian coordinate for the atomic displacement u. Φ, Ψ, and χ are the harmonic, cubic, and quartic FCs, respectively. If the potential energy V is expanded around its minimum energy or equilibrium configuration, Π would be zero. Following the potential energy in Eq. (13), the force on atom i would then be,

$$F_i = -\frac{\partial V}{\partial u_i} = -\Pi_i - \sum_j \Phi_{ij} u_j - \frac{1}{2}\sum_{jk} \Psi_{ijk} u_j u_k - \frac{1}{3!}\sum_{jkl} \chi_{ijkl} u_j u_k u_l \tag{14}$$

Harmonic interactions in Eqs. (13) and (14) are described by Φ_{ij} FCs. The calculations based on purely harmonic energies and forces are called harmonic approximation and are the basis of many reasonable results, such as frequencies of vibrational modes, mean-squared atomic displacements, elastic constant.[11] However, in explaining a number of properties such as,

- Temperature dependence of equilibrium properties (*e.g.*, temperature dependence of thermal expansion or vibrational frequencies).
- Occurrence of phase transitions.

- Transport properties (*e.g.*, TC).

harmonic approximation fails and higher order interactions based on *e.g.*, cubic and quartic FCs are needed to describe the observed physics. These higher order interactions are generally referred to as anharmonicity or anharmonic interactions.

It has been argued that anharmonic interactions (*i.e.*, inelastic scattering) may not be important at room temperature, particularly in systems with nanoscale features,[20] while others have argued that anharmonicity can have notable contributions to TIC at high temperatures.[16,56,57,64-66] English *et al.* [67] and Stevens *et al.* [56] have shown that the increase in TIC at higher temperatures can be attributed to anharmonic interactions between phonons across interfaces. Thus, there are conflicting reports and beliefs within the community, rendering this issue of the role of anharmonicity unresolved due to the lack of consensus.

Over the last 25 years, a variety of methods have been developed,[14,15,17,18,20,28,68] but none of the methods that provide mode level details have fully included anharmonicity. Non-equilibrium MD (NEMD) fully includes anharmonicity and has been used extensively to analyze different interface materials and interface qualities.[67,69-72] However, a formalism that can be used to study the modal contributions to TIC in the context of NEMD is lacking. As a result, the predictive power of methods that provide mode-level detail has been limited to cryogenic temperatures, whereas most engineering applications involve temperatures near or above room temperature, at which anharmonic interactions have the potential to significantly impact interfacial heat transfer.[56,67] Until a method that includes

anharmonicity/inelastic scattering is tested, it is difficult to conclude whether or not anharmonicity is important.

1.3 Comparisons with experiments

Theoretical approaches for calculating the TC of different materials are now able to provide predictions with excellent agreement with experimental measurements.[58,73] However, when it comes to TIC, no general or consistent agreement between computation/theory and experiment has ever been reported. Figure 5 compares the theoretically predicted and experimentally measured values of TIC for a number of isolated interfaces at different temperatures. For all the examined interfaces, at least at some temperatures the theoretical predictions show $\geq$ 20% deviation from the experimental measurements. Therefore, a formalism capable of reliably predicting TIC values in reasonable agreement with experimental measurements is needed.

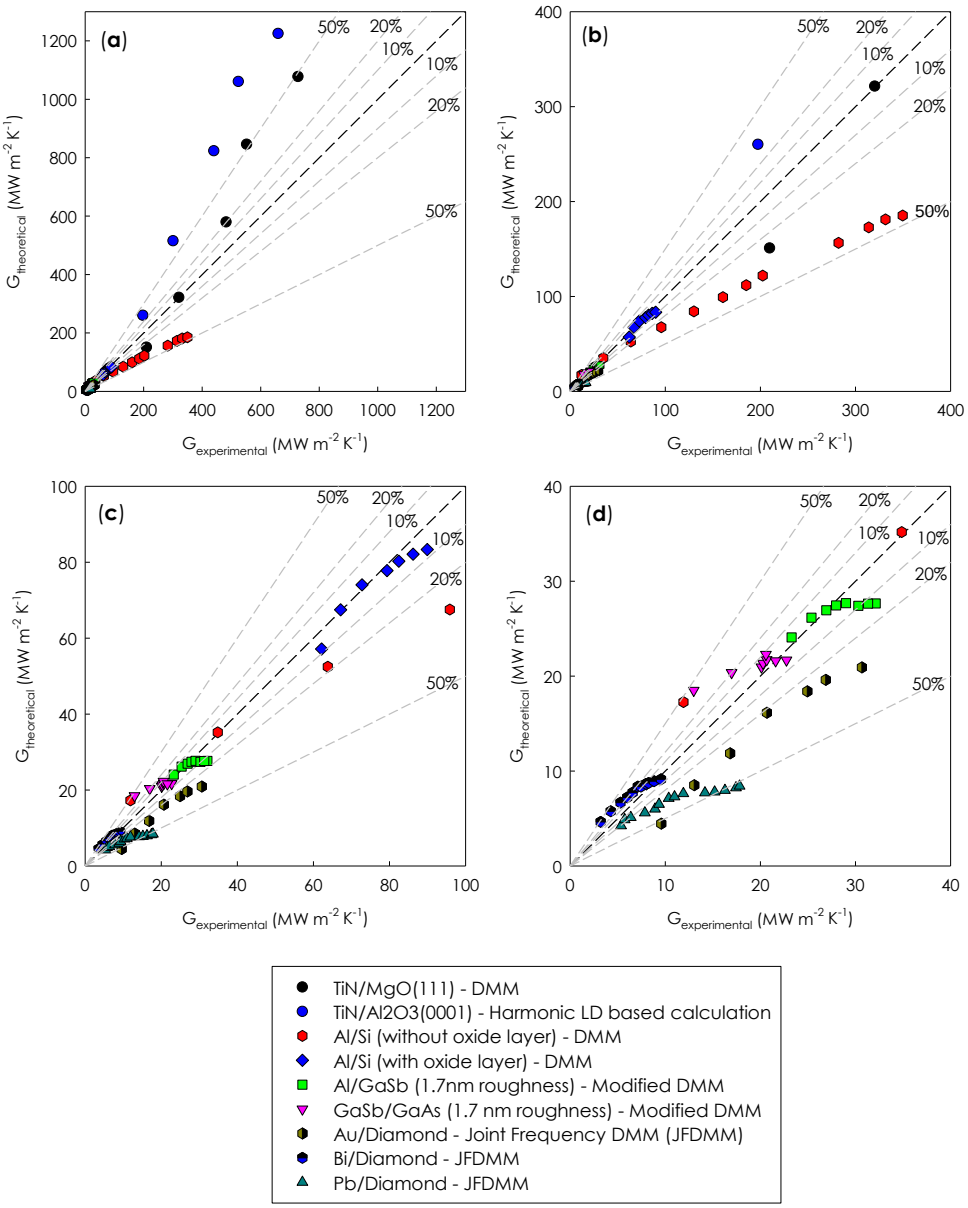

Figure 5 – Comparison of theoretical predictions of TIC across different interfaces with corresponding experimentally measured values. For each interface, each point represents a calculation/measurement at a different temperature. Each panel represents a different TIC range. The dashed lines represent the percent error associated with the theoretical predictions. The examined interfaces have references as follows: TiN/MgO,[74] TiN/Al2O3,[74] Al/Si with/without oxide layer,[75] Al/GaSb,[76] GaSb/GaAs,[76] Au/Diamond,[77] Bi/Diamond,[78] and Pb/Diamond.[78] Modified DMM referenced in the legend was proposed as a variation of DMM to predict TIC across interfaces with severe chemical and structural changes around the interface.[79,80] JFDMM is a variation of DMM, where the altered phonon frequencies in the interface region is also included in the calculations.[50]

1.4 The fundamental problem

For more than half a century, all investigations on heat transfer across interfaces have been conducted using methods that are inherently based on the PGM. Despite the prevalence of the PGM in the literature, predicted conductance values often disagree by 20% or more with experimentally reported values, as illustrated in Fig. 2. This lack of accuracy suggests our understanding of the physics needs revision and revisiting the underlying assumptions of the PGM is a logical starting point. Here we examine the possibility of devising a new formalism that can address the following issues with PGM based approaches:

1. Although the PGM has been utilized to study interfacial heat transfer for decades, no rigorous proof has ever been provided for Eqns. (6) and (11) to assure its correctness. Instead, Eqns. (6) and (11) have been simply derived by analogy to heat flow attributed to gas particles and was not rigorously derived from any first principles.
2. Studies have shown that anharmonicity plays a significant role in interfacial heat transfer at above cryogenic temperatures, however none of the PGM-based techniques has been ever able to capture anharmonicity to full order.
3. The position of atoms near the interface can significantly alter the characteristics of interfacial heat transfer. In spite of this, among the PGM based techniques, only the AGF and WP methods include the exact atomic positions/topography in the calculations, however these techniques are limited to harmonic interactions. Thus, no method has managed to

simultaneously include anharmonicity to full order and the atomic level topography/interface structure.

4. From the mathematical definition of the PGM in Eqs (6) and (11), it can be seen that all the PGM based approaches are dependent on well-defined group velocities for all the modes of vibrations in the system. This limits the applicability of the PGM based techniques to the cases of having only crystalline materials at the sides of the interface. Therefore, PGM based methods cannot be applied to the interface of disordered solids. Thus, a more general method that can treat any type of solid or rigid molecule is needed.

The above issues are potentially the origin of the discrepancies between the PGM predictions and experimental measurements. The PGM does not present a complete picture for the interfacial heat transfer. A new formalism, independent of any assumptions associated with the PGM is needed that can overcome all the above issues. Such a formalism can potentially provide a better agreement with experiment and is the main subject of this thesis.

MD simulations have the potential to solve the above issues as they (1) automatically incorporate inelastic interactions by fully including anharmonicity through finite temperature sampling of a naturally anharmonic interatomic potential; (2) they can be applied to different detailed atomic configurations around interface; and (3) they are completely independent of any definition of group velocity, thus have the potential to be applied to the interface of disordered solids as well. However, based on the existing formulations, MD simulations are only able to calculate the total TIC. It is known that

enlightening insights to future designs can only be achieved by understanding to the modal contributions. Knowing the contributions of specific eigen modes can enable rational design and selection of materials by crafting certain features that will target certain group of modes (*i.e.*, acoustic, optical, longitudinal or transverse), to either inhibit or enhance their transport.[81-83] In general, this quantitative capability has improved our ability to predict classical size effects [84] and other nanoscale phenomena,[85] which are important effects that ultimately limit heat dissipation in applications such as microelectronics.[6] Developing, testing, and extracting insight from a new formalism based on MD simulations to study the modal contributions to TIC is therefore the focus of the remainder of this thesis.

CHAPTER 2. A NEW PARADIGM BASED ON CORRELATION

The interaction between different modes of vibration in the PGM paradigm is described by the scattering picture. According to the scattering picture, incident phonons on the interface undergo specific scattering mechanisms, where they either combine with other phonons to make new phonons or become scattered themselves to generate new phonons – subject to energy conservation constraints. A similar scattering picture is also utilized by the PGM to describe TC. Such a scattering picture has been able to predict the TC of crystalline solids in great agreement with experimental values.[58-60] However, the scattering picture has not been successful in consistently predicting the TIC values even across crystalline interfaces (see Figure 5). Therefore, a new formalism with improved predictive abilities is needed. The critical question then becomes whether an alternative picture to the existing phonon scattering picture can be found.

MD simulations are inherently independent of any assumptions or conceptualizations of phonon behavior. Therefore, they can form a promising foundation for a new formalism independent of the PGM. For calculating TIC using MD simulations, two major approaches exist: (1) NEMD, and (2) equilibrium MD (EMD) formulations.

Calculation of TIC in NEMD simulations follows the direct definition of TIC. In this approach, a heat flow is transferred through the structure by placing hot and cold reservoirs in different positions in the system. At steady state, temperature profile develops in the structure (*e.g.*, similar to the one in Figure 1), and by directly measuring the temperature difference between the two sides of the interface, TIC can be calculated using the formula,

$$G = \frac{\overline{Q}}{\Delta T} \tag{15}$$

where $\overline{Q}$ is the steady state, time-averaged interfacial heat flux in the NEMD simulation, and ΔT is the temperature difference at the interface, determined by extrapolation of the temperature gradients in each respective material.[69,86-88]

In EMD simulations, calculation of TIC follows the fluctuation-dissipation theorem.[89] In this approach, TIC is proportional to the auto-correlation of the equilibrium fluctuations of heat flux across the interface based on the following formula,

$$G = \frac{1}{Ak_B T^2} \int_0^\infty \left\langle Q(t) \cdot Q(0) \right\rangle dt \tag{16}$$

where A is the interface contact area, k_B is the Boltzmann constant, T is the equilibrium temperature of the system, Q is the instantaneous interfacial heat flux, and $\langle \cdots \rangle$ represents the autocorrelation function. This EMD formulation suggests a possible alternative picture to the scattering one– a new picture based on correlation.

2.1 Interface conductance based on the fluctuation-dissipation theorem

The equilibrium approach for the calculation of TIC (Eq. (16)) is in concept similar to the Green-Kubo technique for the calculation of TC from EMD simulations and was first introduced by Puech *et al.*[90] The definition in Eq. (16) can be justified by the following derivation.[91] Consider the interface of two solid materials, denoted by A and B, coupled together. If $E_A(t)$ is the energy of the solid A at time t, the Langevin evolution of this variable can be written as,[91]

$$E_A(t) = Q(t) = GA\left(T_0 - T_A(t)\right) + f(t) \tag{17}$$

where $T_A(t)$ is the instantaneous temperature of solid A at time t, and T_0 is the time-averaged temperature of the system. In the Langevin description, the evolution of the slow variable (*i.e.*, energy) is separated into a systematic contribution (*i.e.*, a macroscopic evolution) and a random, δ correlated part $f(t)$. Writing $\langle f(t) f(t') \rangle = \gamma \delta(t - t')$ and $X = E_A(t) - \langle E_A \rangle = C_V \left(T_A(A) - T_0\right)$ one may rewrite Eq. (17) in the standard Langevin form,

$$\frac{dX}{dt} = -\alpha X(t) + f(t) \tag{18}$$

With $\alpha = AGC_V$, Eq. (18) is a standard Langevin equation for the variable X. The usual relations follow for the correlation functions

$$\langle X(t) X(0) \rangle = \frac{\gamma}{2\alpha} \exp\left(-\alpha |t|\right) \tag{19}$$

$$\langle q(t) q(0) \rangle = -\frac{d^2}{dt^2} \langle X(t) X \langle 0 \rangle \rangle = \gamma \delta(t) - \frac{\alpha \gamma}{2} \exp\left(-\alpha |t|\right) \tag{20}$$

In the thermodynamic limit $\left(C_V \to \infty\right)$, the second term vanishes (since $\alpha = 0$ in this limit), so that one may write

$$\gamma = 2 \int_0^\infty \langle q(t) q(0) \rangle \, dt \tag{21}$$

Using the relation $\left\langle X^2 \right\rangle = \gamma / 2\alpha$ which follows from Eq. (19) at $t = 0$, and the equilibrium distribution for X which yields the standard fluctuation formula $\left\langle X^2 \right\rangle = \left\langle \delta E^2 \right\rangle = k_B T^2 C_V$, the equilibrium definition of TIC in Eq. (16) is obtained immediately from Eq. (21).

Microscopically, any thermodynamic quantity exhibits local fluctuations in time. No matter how random these fluctuations might seem, there are patterns embedded within them associated with the patterns in the underlying atomic vibrations that contribute to the quantity. Correlation function quantifies these repetitive patterns in the existing fluctuations of the dynamic variable. According to Eq. (16), TIC is directly proportional to the auto-correlation of the interfacial heat flux. If interfacial heat flux shows stronger interdependence and stays correlated for a longer time it will result in larger TIC. The definition of TIC according to Eq. (16) is very similar to the definition of TC based on the Green-Kubo definition.[33] Calculating the modal contributions to Eq. (16) will allow analyzing the underlying physical mechanisms of interfacial heat transfer with a higher resolution. In this chapter, first the EMD definition of TIC in Eq. (16) will be proven, and then a new formalism, termed interface conductance modal analysis (ICMA), based on MD simulations capable of calculating the modal contributions with full inclusion of anharmonicity will be developed.

2.2 Derivation of interface conductance modal analysis (ICMA)

In this section, a new formalism based on MD simulations will be devised. Such a formalism will be able to extract the modal contributions to interface conductance with full inclusion of anharmonicity and detailed atomic positions around the interface into the calculations. Consider forming an interface by bringing two systems A and B into contact, each having N_A and N_B atoms. We can use the LD formalism [11] to obtain the complete $3N=3(N_A+N_B)$ eigen solutions to the equations of motion describing the vibrations of the

system when all the interactions are considered to be harmonic. These eigen solutions allow us to write the atomic displacements and velocities as,

$$\mathbf{x}_i = \sum_n \frac{1}{\left(Nm_i\right)^{1/2}} \mathbf{e}_{n,i} X_n \tag{22}$$

$$\dot{\mathbf{x}}_i = \sum_n \frac{1}{\left(Nm_i\right)^{1/2}} \mathbf{e}_{n,i} \dot{X}_n \tag{23}$$

where n is the index for the eigen mode, $\mathbf{x}_i$, $\dot{\mathbf{x}}_i$, and m_i are the displacement from equilibrium, velocity and mass of atom i respectively, and $\mathbf{e}_{n,i}$ is the eigen vector for mode n assigning the direction and displacement magnitude of atom i. From the inverse of the operations in Eqns. (22) and (23), we can define the normal mode coordinates of position and velocity for mode n (X_n and $\dot{X}_n$) as,

$$X_n = \sum_i \frac{m_i^{1/2}}{N^{1/2}} \mathbf{x}_i \cdot \mathbf{e}_{n,i}^* \tag{24}$$

$$\dot{X}_n = \sum_i \frac{m_i^{1/2}}{N^{1/2}} \dot{\mathbf{x}}_i \cdot \mathbf{e}_{n,i}^* \tag{25}$$

where i is the index for the atom in the system, and $*$ represents complex conjugate. A system of N atoms has a Hamiltonian given by,

$$H = \sum_i^N \frac{\mathbf{p}_i^{\,2}}{2m_i} + \Phi\left(\mathbf{r}_1, \mathbf{r}_2, \cdots, \mathbf{r}_n\right) \tag{26}$$

where Φ is the total potential energy of the system, and the position and momentum of atom i are denoted by $\mathbf{r}_i$ and $\mathbf{p}_i$, respectively. From Eq. (26), the individual Hamiltonian for atom i can be written as,

$$H_i = \frac{\mathbf{p}_i^{\,2}}{2m_i} + \Phi_i\left(\mathbf{r}_1, \mathbf{r}_2, \cdots, \mathbf{r}_n\right) \tag{27}$$

where Φ_i is the potential energy assigned to a single atom.[92,93] Using the above definition of the Hamiltonian for an individual atom, the energy exchanged between material A and B $\left(Q_{A\to B}\right)$ at each instant of time can be written as,

$$\begin{aligned} Q_{A\to B} &= -\sum_{i\in A}\sum_{j\in B}\left\{\frac{\mathbf{p}_i}{m_i}\cdot\left(\frac{-\partial H_j}{\partial \mathbf{r}_i}\right) + \frac{\mathbf{p}_j}{m_j}\cdot\left(\frac{\partial H_i}{\partial \mathbf{r}_j}\right)\right\} \\ &= -\sum_{i\in A}\sum_{j\in B}\left\{\frac{\mathbf{p}_i}{m_i}\cdot\left(\frac{-\partial \Phi_j}{\partial \mathbf{r}_i}\right) + \frac{\mathbf{p}_j}{m_j}\cdot\left(\frac{\partial \Phi_i}{\partial \mathbf{r}_j}\right)\right\} \end{aligned} \tag{28}$$

which is a general equation that is valid for any interatomic potential, including pairwise or even multi-body potentials, as long as the total potential energy of the system $\left(\Phi\right)$ can be written as a sum of individual atom potential energies $\left(\Phi_i\right)$ (i.e., $\Phi = \sum_i \Phi_i$). In Eq. (28) is a double summation, and the first summation (index i) is performed over all the atoms in material A, and the second summation (index j) is performed over all the atoms in material B. For the case of having pairwise interactions between material A and B, Eq. (28) is reduced to,

$$Q_{A\to B} = -\frac{1}{2}\sum_{i\in A}\sum_{j\in B}\mathbf{f}_{ij}\cdot\left(\dot{\mathbf{x}}_i + \dot{\mathbf{x}}_j\right) \tag{29}$$

where $\mathbf{f}_{ij}$ is the pairwise exchanged force between atoms i and j in the two materials.[65,94,95] Having pairwise interactions, half of the interaction energy is naturally partitioned with atom i and the other half with atom j. For simplicity, we will use Q instead of $Q_{A\to B}$ for interfacial heat flow in the ensuing discussion. Using Eq. (29) and fluctuation-dissipation theorem,[89] Puech *et al.* [90] as well as Domingues *et al.* [95] and Barrat *et al.* [91] showed that the conductance is proportional to the correlation between the equilibrium heat flow fluctuations via the equilibrium definition of TIC in Eq. (16). It can be seen from Eq. (16) that if one can obtain the modal contributions to the interfacial heat flow such that at each instant the obtained modal contributions sum to the total Q,

$$Q = \sum_n Q_n \tag{30}$$

then G can be rewritten as,

$$G = \frac{1}{Ak_BT^2}\int\left\langle\sum_n Q_n(t)\cdot Q(0)\right\rangle dt = \sum_n \frac{1}{Ak_BT^2}\int\left\langle Q_n(t)\cdot Q(0)\right\rangle dt \tag{31}$$

This then yields the individual modal contributions to G as,

$$G_n = \frac{1}{Ak_BT^2}\int\left\langle Q_n(t)\cdot Q(0)\right\rangle dt \tag{32}$$

where,

$$G = \sum_n G_n \tag{33}$$

Furthermore, the modal heat flux definition in Eq. (30) allows us to substitute for both of the total heat fluxes in Eq. (16) leading to another definition for G as,

$$G = \frac{1}{Ak_B T^2} \int \left\langle \sum_n Q_n(t) \cdot \sum_{n'} Q_{n'}(t) \right\rangle dt = \sum_n \sum_{n'} \frac{1}{Ak_B T^2} \int \left\langle Q_n(t) \cdot Q_{n'}(0) \right\rangle dt \tag{34}$$

where individual contributions from pairs of modes equal to,

$$G_{n,n'} = \frac{1}{Ak_B T^2} \int \left\langle Q_n(t) \cdot Q_{n'}(0) \right\rangle dt \tag{35}$$

To complete the formulation, the important step is then to determine Q_n, with the requirement of Eq. (30) (*i.e.*, $Q = \sum_n Q_n$), which can be accomplished by replacing the atomic velocities in Eq. (28) with their modal definition in Eq. (23),

$$\begin{aligned} Q &= \sum_{i \in A} \sum_{j \in B} \left\{ \left(\sum_n \frac{1}{\left(Nm_i\right)^{1/2}} \mathbf{e}_{n,i} \dot{X}_n \right) \cdot \left(\frac{\partial H_j}{\partial \mathbf{r}_i} \right) - \left(\sum_n \frac{1}{\left(Nm_j\right)^{1/2}} \mathbf{e}_{n,\mathrm{j}} \dot{X}_n \right) \cdot \left(\frac{\partial H_i}{\partial \mathbf{r}_j} \right) \right\} \\ Q_n &= \frac{1}{N^{1/2}} \sum_{i \in A} \sum_{j \in B} \left\{ \left(\frac{1}{\left(m_i\right)^{1/2}} \mathbf{e}_{n,i} \dot{X}_n \right) \cdot \left(\frac{\partial H_j}{\partial \mathbf{r}_i} \right) + \left(\frac{1}{\left(m_j\right)^{1/2}} \mathbf{e}_{n,\mathrm{j}} \dot{X}_n \right) \cdot \left(\frac{-\partial H_i}{\partial \mathbf{r}_j} \right) \right\} \end{aligned} \tag{36}$$

Eq. (36) is general and it can be simplified for pairwise interactions to,

$$Q_n = \sum_{i\in A}\sum_{j\in B}\frac{-\mathbf{f}_{ij}}{2}\cdot\left(\frac{1}{\left(Nm_i\right)^{1/2}}\mathbf{e}_{n,i}\dot{X}_n + \frac{1}{\left(Nm_j\right)^{1/2}}\mathbf{e}_{n,j}\dot{X}_n\right) \tag{37}$$

Eq. (36) and Eq. (37) are the definitions of modal contributions to interfacial heat flow.

The definition in Eq. (35) represents TIC as the summation of all the auto-correlations and cross-correlations between eigen mode pairs n and n' in the system ($G = \sum_{n,n'} G_{n,n'}$) and provides new insight into the degree to which each pair of modes interact and contribute to TIC. As a result, the ICMA method presented above, contains more detail and can potentially lead to deeper insights into the physics of TIC. This deeper insight is now accessible, because Eq. (35) elucidates the modal contributions to the correlation picture that was introduced in the equilibrium definition of TIC in Eq. (16). In this more detailed picture, the TIC is broken into pairwise contributions by all the pairs of modes in the system. Many modes of vibration exist in the structure and each pair can transfer the heat across the interface and contribute to TIC if correlated. This correlation picture and mathematical formulation (Eq. (35)) has the following significant outcomes that may not necessarily be in agreement with the existing paradigms:

1) In the PGM picture, each mode of vibration can have a maximum contribution to TIC, when the entire energy of the incident phonon is transmitted to the other side of the interface (*i.e.*, $\tau = 1$). However, according to the correlation picture and the provided in Eq. (35), no upper limit exists on the degree to which two modes of vibration can be correlated and contribute to TIC. In fact, as was shown in the simulations of thermal conductivity (from equilibrium Green-

Kubo calculations), some of the vibrational modes have the potential to show very long/strong correlations that can even lead to divergent thermal conductivities.[96]

2) The contribution of each mode of vibration to TIC is dependent on the presence of other modes of vibration in the system. In this view, modal contributions are mutual contributions originating from the presence of all the modes of vibrations in the system.

3) The mathematical formulation provided in Eq. (35) even allow for positive and negative contributions to TIC, because the fluctuations in the contribution to heat flux by two modes of vibration can become correlated and anti-correlated that can lead to positive and negative contribution to TIC, respectively.

2.3 ICMA application to NEMD simulations

The modal heat flux in Eq. (36) can also be readily used in NEMD simulations to obtain modal contributions to interface conductance. Here we used $G = \frac{\overline{Q}}{\Delta T}$ (similar to Eq. (15)). The modal contribution to the conductance (G_n) then becomes,

$$G_n = \frac{\overline{Q_n}}{\Delta T} \tag{38}$$

where the same ΔT is used for every mode.

CHAPTER 3. ICMA VALIDATION

3.1 Choosing the correct vibrational basis set

The modal contributions to interfacial heat flux formulated in Eq. (36) are based on atomic velocities and eigen modes of vibration from both sides of the interface. Such a description for interfacial heat flux is inconsistent with the dominant view of the PGM whereby, as a result of using the principle of detailed balance in deriving Landauer formalism (Eq. (9)), all the parameters required to describe the interfacial heat transfer are obtained from the vibrational information belonging to only one side of the interface (see Eq. (11)). To resolve this inconsistency, one can potentially use the following equations, which are only based on atomic velocities and eigen modes of vibration from one side of the interface,

$$Q = -\sum_{i\in A}\sum_{j\in B}\frac{\mathbf{p}_i}{m_i}\cdot\left(\frac{-\partial H_j}{\partial \mathbf{r}_i}\right) \tag{39}$$

$$Q_n = \frac{1}{N^{1/2}}\sum_{i\in A}\sum_{j\in B}\left(\frac{1}{\left(m_i\right)^{1/2}}\mathbf{e}_{n,i}\dot{X}_n\right)\cdot\left(\frac{\partial H_j}{\partial \mathbf{r}_i}\right) \tag{40}$$

where Q and Q_n are the total and modal instantaneous interfacial heat flux values, respectively. The difference between the above equations and Eqns. (29) and (36) can be better understood by reconsidering the general definition of interfacial heat flux in Eq. (28). Equation (28) is based on the potential energy of the interaction between atoms at the opposite sides of the interface. According to Eq. (28) different definitions for interfacial

heat flux can be obtained by partitioning this interaction potential energy in different formats.[43] For instance, Eqns. (39) and (40) are obtained by ascribing this interaction potential energy only to the atoms on one side of the interface (*e.g.*, side B), which allows the interfacial heat flux to be explained by only using the atomic velocities and eigen modes of vibration belonging to the other side of the interface (*e.g.*, side A). Calculating the modal contributions to heat flux from Eq. (40) requires eigen modes of vibration from only one side of the interface, which in agreement with Landauer formalism formulated in Eq. (11) can be obtained from the bulk vibrational modes on that side of the interface.

It should be noted that the modal contributions to interfacial heat flux can still be calculated using Eq. (36), but it requires one utilize a different set of vibrational modes than the ones associated with one material as eigen modes of vibration from both sides of the interfaces are incorporated in Eq. (36). The key question then becomes, which set of modes (i.e., basis set) should one use in the heat flow decomposition to calculate physically meaningful contributions? This is important, since mathematically there are infinite number of basis sets that are complete and can be used for modal analysis, meaning that they are guaranteed to return the same amount of total heat flow and total interface conductance (i.e., they are able to satisfy the $Q = \sum_n Q_n$ and $G = \sum_n G_n$ conditions). However, different choices might ascribe different amounts of contributions to heat flux and TIC to different frequencies (*i.e.*, each basis set calculating different values of Q_n and G_n). This is critical because different spectral contributions might then lead to different temperature dependent TIC predictions when quantum effects on the heat capacity are accounted for (*i.e.*, by applying approximate quantum corrections).[97,98] In reality, one must

account for quantum effects on the heat capacity of the different modes. Since the classical MD heat capacity is the same for every mode, as one approaches low temperatures the conductance would not approach zero as $T \to 0K$, which is qualitatively incorrect. Recently Lv and Henry have shown via the (Green-Kubo modal analysis) GKMA formalism [99] that one can extend the classical MD results to essentially any temperature accurately by simply correcting the heat capacity portion of the transport coefficient. Even though the MD simulation itself at low temperatures will still reflect the interactions between low frequency modes and higher frequency modes that should not be excited, for many systems it is likely that these interactions are weak or essentially negligible leading to quantitatively correct values for the modal contributions to the transport property. Lv and Henry's recent calculations [99,100] seem to suggest this is scheme works well and therefore, we apply a similar correction here to account for quantum effects on the heat capacity of vibrational modes with frequency (ω) at temperature (T) using the following relations,

$$G_Q(T) = \sum_{\omega} G_{MD}(\omega, T) \cdot \frac{C_Q(\omega, T)}{C_{MD}} \tag{41}$$

where,

$$\frac{C_Q(\omega, T)}{C_{MD}} = \frac{\hbar\omega}{k_B} \frac{df(\omega, T)}{dT} = \frac{x^2 e^x}{\left(e^x - 1\right)^2} \tag{42}$$

and indices Q and MD stand for quantum and molecular dynamics (classical), respectively. In Eqns. (41) and (42), k_B and $\hbar$ are Boltzmann constant and Planck's

constant divided by 2π, respectively, and $x = \frac{\hbar\omega}{k_B T}$. The key feature of Eq. (41) is the fact that the heat capacity of every mode is frequency dependent. Thus, for example, if the TIC is dominated by low frequency modes, the temperature regime where it will decrease towards zero at low temperatures may be quite low, versus if it is dominated by higher frequency modes, the temperature regime where TIC will decrease towards zero at low temperatures may occur at somewhat higher temperatures. In this section, we essentially examine the validity of the most basic assumption in the PGM treatment of heat transfer across interfaces that one can describe interfacial transport in terms of the bulk materials' modes (see Eq. (11)). Our analysis will show whether the PGM paradigm is correct or whether we need a new set for the contributing modes of vibration at the interface of two materials.

Towards finding the correct set of modes to be used in the heat flow decomposition, we have identified three potential options for the modal decomposition of the interfacial heat flow (Eqns. (36) and (37)). These three basis sets are schematically shown in Figure 6. If we consider two bulk materials labeled A and B respectively, when they are joined and form an interface, the three choices for describing the modes that contribute to heat flow through their interface are denoted by {A/B}, {A+B} and {AB}. The basis set {A/B} corresponds to the modes associated with the bulk of either material A or B, where one performs a LD calculation for each individual bulk material (see Figure 6a). The modal basis set {A+B} corresponds to the addition of the eigen solutions for each separate bulk material, whereby one simply assigns polarization vectors equal to zero for the atoms on side B, for modes on side A, and vice versa (see Figure 6b). The third choice is then basis

set {AB}, which corresponds to the modes obtained from a LD calculation for the entire structure, containing both materials A and B along with their interface (see Figure 6c). The basis set choices {A/B} and {A+B} are conceptually consistent with the PGM view of interface transport, since they correspond to the modes of the bulk material and for crystals are guaranteed to yield all propagating modes that have well-defined velocities. Using the bulk modes, which have well-defined velocities, is critical to the current paradigm, because the PGM description of TIC casts each mode's contribution as proportional to its velocity.[18,33] Thus, a non-propagating or localized mode's contribution is ill-defined in the PGM paradigm, and it is therefore of critical importance to determine if {A/B} and/or {A+B} can still be used to describe interfacial transport.

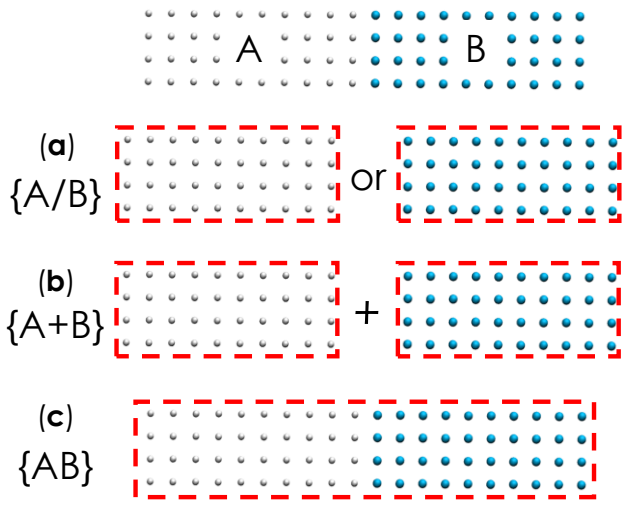

Figure 6 – For the interface between two solid materials A and B, three bases sets are chosen and examined for their physical correctness: (a) {A/B}, (b) {A+B}, and (c) {AB}. The red dashed lines show the region where the modes of vibration are calculated for using the LD formalism.

The correct basis set can be determined based on purely theoretical considerations, because it must reproduce the expected behavior in the harmonic limit (*e.g.*, as $T \to 0K$). As $T \to 0K$, the atomic interactions approach that of a perfectly harmonic potential, which

then leads to purely elastic interactions, whereby modes can only transfer their energy to other modes with the same frequency. We know this must be true, because in the harmonic limit, one can solve the equations of motion analytically and the elastic behavior at an interface can be described exactly. We therefore require that any new formalism and basis set reproduce this known behavior in the harmonic limit. In general, there could be modes on one side of the interface (denoted side A) that are above the maximum frequency that can be supported on side B, which we label as the heavier or weaker material with a lower maximum vibration frequency denoted by $\omega_{max,B}$. Modes with frequencies above $\omega_{max,B}$ on side A have no corresponding mode with the same frequency on side B to exchange energy with through elastic interactions. Therefore, in the $T \to 0K$ limit, these modes cannot contribute to the TIC when anharmonic coupling is disabled. It is important to note that this effect is correctly reproduced by MD simulations, as the WP method shows that modes above $\omega_{max,B}$ have 0% transmission.[27-30] This behavior is also well understood and reproduced by other established methods such as the AGF method, since the majority of implementations of the AGF method are based harmonic approximation.[19-23] Thus, by simply testing which basis sets show zero contributions to the TIC from modes above $\omega_{max,B}$ as $T \to 0K$, we can determine which basis is correct.

Here, we studied a simple interface between lattice matched Lennard-Jones (LJ) face-centered cubic (FCC) solids. The LJ potential is defined based on the following formula,[101]

$$\Phi = 4\varepsilon\left[\left(\frac{\sigma}{r}\right)^{12} - \left(\frac{\sigma}{r}\right)^{6}\right] \tag{43}$$

where ε and σ are the energy and distance parameters and r is the distance between two interacting atoms. We select equal values of ε and σ for both materials A and B, which results in equal lattice constants for the two sides. An acoustic mismatch exists at the interface because the mass of the atoms on side B are four times the mass of atoms on side A ($m_B = 4m_A$). Both sides have FCC lattice structures. In LJ systems the simulations can be performed in LJ dimensionless units,[102] but to have the results correspond to a physically meaningful system, we chose LJ parameters in our simulations to be equal to that of argon ($\varepsilon = 1.67\times10^{-21} J$, $\sigma = 3.405\text{Å}$, and $m_A = 6.6\times10^{-26} kg$ [103]). Thus, side A represents solid argon (mass m) and side B represents a fictitiously heavier solid argon (mass $4m$) and by averaging an isobaric-isothermal simulation at zero pressure and T=1K, the lattice constant was calculated as 5.26Å.

3.1.1 EMD simulations

In our EMD simulations for the interface between LJ crystals, the system consists of 3x3x60 FCC unit cells (each side 30 unit cells long), which includes 2160 atoms and 6480 eigen modes. We confirmed that increasing the size of cross section does not change the features observed in the results, which is in agreement with other reports.[23,94] Initially, an equilibration period equal to 2 ns is performed. Then, modal heat flux contributions (Q_n) are recorded for 5 ns in the micro-canonical ensemble. The modal contributions to the heat flow, Q_n, are then used in post processing, which leads to the calculation of modal

thermal conductance (G_n). A time step of 1 fs was chosen for the simulations and ten independent ensembles were simulated to reduce the standard deviation in TIC below 5% [104]. The TIC accumulation function was then computed for all three basis sets according to the ICMA formalism [105] and is shown in Figure 7. At a temperature of 1K, only the {AB} basis set shows the qualitatively correct behavior as all of the contributions above $\omega_{max,B}$ decay to zero. Both the {A/B} and {A+B} basis sets, however, still attribute large portions of the TIC to frequencies that only exist in the bulk of side A and cannot transmit any energy to side B.

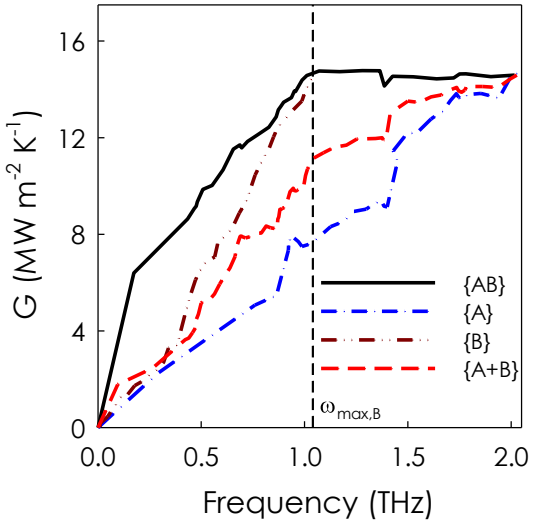

Figure 7 – Modal contributions to interface conductance at T=1K at the interface of two lattice matched, mass mismatched LJ solids calculated using different basis sets. {A/B} basis set can either express the modes on the bulk of side A or on the bulk of side B. The modal contributions from these two basis sets are shown in the figure using {A} and {B}, respectively. Since the {B} basis set is based on the heavier side of the interface, the maximum frequency in this basis set is $\omega_{max,B}$, therefore the contributions by higher frequencies cannot be calculated using the {B} basis set.

It should be noted that 0% transmission above $\omega_{max,B}$ was also observed for a perfectly smooth interface between two lattice matched diamond structured materials,

modeled with the Tersoff potential,[106] using parameters for silicon (Si) on both sides of the interface and Si with a 4X larger mass on the other. For this structure, we used EMD simulations to calculate the modal contributions to TIC. The system consists of 3x3x36 diamond unit cells (each side 18 unit cells long), which includes 2592 atoms and 7776 eigen modes of vibration. By averaging in an isobaric-isothermal simulation at zero pressure and T=1K, the lattice constant was calculated as $5.43\mathring{A}$. The temperature of the simulation is set to T=1K. Initially, an equilibration period of 5 ns under the NPT ensemble is performed. Then, modal heat flux contributions (Q_n) were recorded for 10 ns in the micro-canonical ensemble. The modal contributions to the heat flow, Q_n, are then used in post processing, which leads to the calculation of modal thermal conductance (G_n). A time step of 0.5 fs was chosen for the simulations and ten independent ensembles were simulated to reduce the standard deviation in TIC below 5%. The accumulations have been calculated for different basis sets and are presented in Figure 8. Again, by using the {AB} basis set, no contribution to TIC from frequencies above $\omega_{B,\max}$ was observed, yet for the {A/B} and {A+B} bases, the frequency dependence is qualitatively incorrect. Since only the {AB} basis set yields the qualitatively correct behavior in both cases, our conclusion is that {AB} is the correct choice.

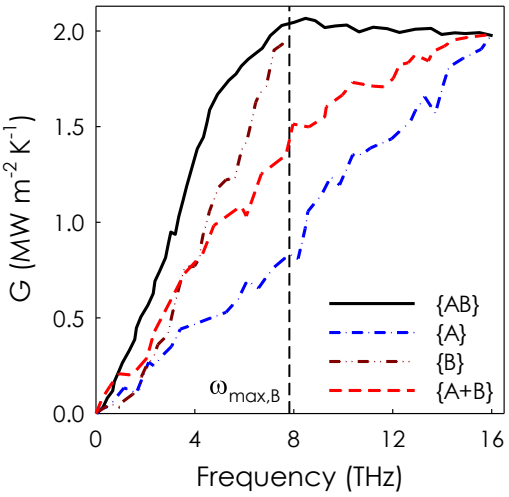

Figure 8 – TIC accumulation for different basis sets at the interface of a lattice matched, mass-mismatched Si diamond structured system. Accumulation is calculated at a temperature of T=1K. {A/B} basis set can either express the modes on the bulk of side A or on the bulk of side B. The modal contributions from these two basis sets are shown in the figure using {A} and {B}, respectively. Since the {B} basis set is based on the heavier side of the interface, the maximum frequency in this basis set is $\omega_{max,B}$, therefore the contributions by higher frequencies cannot be calculated using the {B} basis set.

3.1.2 Wave-packet simulations

To understand why {A/B} and {A+B} yield qualitatively incorrect behavior, a test was devised based on the WP method, whereby only a narrow range of frequencies with a single polarization is excited, and all other modes have zero amplitude which approximates $\mathrm{T}\to 0\mathrm{K}$. The WP is launched towards the interface [29,30] from bulk of side A, and when it reaches the interface it elastically scatters, and a fraction of its energy is transmitted into modes with similar frequency on side B. We form the WP from the longitudinal polarization by displacing the atoms in the system according to,[29]

$$u_i = A_0 e_i\left(k_0\right)\exp\left[ik_0\left(z-z_0\right)\right]\exp\left[-\eta^2\left(z_1-z_0\right)^2\right], \tag{44}$$

where the plane of the interface is perpendicular to the z-direction, A_0 is the amplitude of the wave packet, k_0 is the central wave vector for the WP, η is the spatial extent of the WP, and z_0 is the initial central location for the WP.[29] For the WP simulations in this study, we set the parameters to be $A = 0.00001a_0$, $k_0 = 0.2\frac{2\pi}{a_0}$, $\eta = 50a_0$, and $z_0 = 150a_0$, where a_0 is the lattice constant for solid argon. Initial atomic velocities are assigned based on the differentiation of Eq. (44) with respect to time.[29] Initially, the WP has a certain amount of energy ($E_{init.}$), and when it reaches the interface, part of its energy is transmitted ($E_{trans.}$) and the remainder is reflected ($E_{refl.}$). The polarization of both the reflected and the transmitted WPs can be different from the incident WP, however both should have the same frequencies as the incident WP.[29] In previous WP studies, the energy of different modes is studied and the transmission (τ) is computed from,[30]

$$\tau = \frac{E_{trans.}}{E_{init.}} \tag{45}$$

Using Eq. (37), the modal contributions to the interfacial heat flow are tracked in time for all three choices {A/B}, {A+B}, and {AB}. For a correct basis set, the following two features should be observed: (1) Since the scattering event will be purely elastic, as the WP reaches the interface, we should only observe heat flow contributions Q_n associated with the original modes in the WP on side A or the modes in the transmitted WP on side B. (2) If we integrate Q_n in time, we should see that only the modes that participate in the incoming or outgoing WPs contribute to the energy transfer across the interface. Figure 9

shows that {A/B} and {A+B} do not exhibit these features, as they both show frequency broadening when the WP reaches the interface. This is unphysical because the frequency content of all the atomic motions before, during, and after the scattering event all lie within the same frequency range as the original WP. Therefore, the broadening exhibited by {A/B} and {A+B} is not representative of actual excitation of those frequencies. Instead, this broadening is a type of aliasing, since the modes in {A/B} and {A+B} do not contain information about the interface condition or bonding. Therefore, {A/B} and {A+B} ascribe contributions to modes that are not actually excited, which is why they assign large TIC contributions to modes with frequencies > $\omega_{max,B}$ as $T \to 0K$ (45% and 22% respectively). However, only when the combined system {AB} is used, are all of the theoretical requirements satisfied.

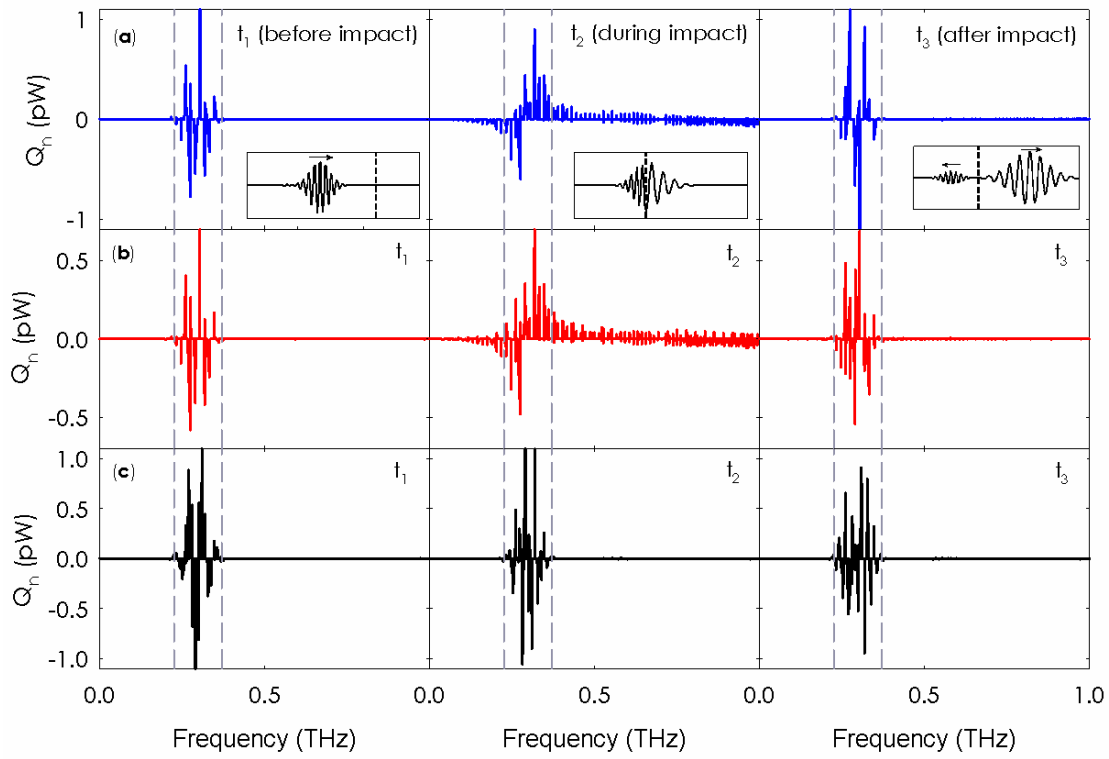

Figure 9 – Modal contributions to interfacial heat flow for the WP simulation at the interface of two lattice matched, mass mismatched LJ solids calculated using different basis sets of (a) {A}, (b) {B}, (c) {A+B}, and (d) {AB}. The data represents three different instants: before the impact (t_1), during the impact (t_2), and after the impact (t_3). The atomic displacement profiles at these three times are shown as insets in (a). The dashed lines show ($\Delta\omega$) the range of frequencies in the originally excited WP. Since the {B} basis set is based on the heavier side of the interface, the maximum frequency in this basis set is $\omega_{max,B} \approx 1.03 THz$, therefore the contributions by higher frequencies cannot be calculated using the {B} basis set.

3.2 Alternative Decompositions

The ICMA formulation [43,105] presented in the previous sections is based on the decomposition of velocities alone. However, another approach can be formulated based on the decomposition of forces. Similar to velocity decomposition, modal analysis based on force decomposition is also mathematically complete, meaning that the summation of calculated modal contributions will add up to the same total value of heat flux in each

instant of time. However, in addition to being mathematically complete, one needs to also check whether the calculated modal contributions from force decomposition are physically meaningful.

3.2.1 ICMA with force decomposition

The force decomposition of heat interfacial heat flux follows the following formulation. Instantaneous energy exchange at the interface of two solid materials A and B can be written as in Eq. (28). For simplicity we will write $\frac{\partial H_j}{\partial \mathbf{r}_i}$ and $\frac{\partial H_i}{\partial \mathbf{r}_j}$ in Eq. (28) in the form of $-\mathbf{F}_{ji}$ and $-\mathbf{F}_{ij}$, respectively. This allows us to rewrite Eq. (28) as,

$$Q = -\sum_{i\in A}\sum_{j\in B}\left\{\frac{\mathbf{p}_i}{m_i}\cdot\mathbf{F}_{ji} + \frac{\mathbf{p}_j}{m_j}\cdot\left(-\mathbf{F}_{ij}\right)\right\} \tag{46}$$

Eq. (46) can be further simplified to the following form,

$$Q = \sum_{i\in A}\frac{\mathbf{p}_i}{m_i}\cdot\mathbf{F}_i + \sum_{j\in B}\frac{\mathbf{p}_j}{m_j}\cdot\mathbf{F}_j \tag{47}$$

where $\mathbf{F}_i$ and $\mathbf{F}_j$ are force vectors attributed to atoms i and j that are summed over all the individual interactions with the atoms on the other side of the interface. Here, it is very important to realize that the instead of writing the individual forces between each pair or triplet, etc. of atoms, all of such individual forces have been summed. This results in a single force vector for each atom that represents the net interaction it has with the other side of the interface and allows for simplification of Eq. (47), whereby we can sum over

all atoms in the system at once. Similar to the momentum vector field, these resultant forces ($\mathbf{F}_i$ and $\mathbf{F}_j$) attributed to each atom in the system can also be considered as a vector field throughout the entire structure. In this view, Eq. (47) can be rewritten as a single summation using a single index (*e.g.*, i') going over all the atoms in the system,

$$Q = \sum_{i' \in A+B} \frac{\mathbf{p}_{i'}}{m_{i'}} \cdot \mathbf{F}_{i'} \tag{48}$$

Now, to perform the modal analysis based on the force decomposition, we first calculate the normal mode force amplitude for mode n (*e.g.*, Ξ_n) as follows,

$$\Xi_n = \sum_{i'} \sqrt{\frac{m_{i'}}{N}} \mathbf{F}_{i'} \cdot \mathbf{e}_{n,i'} \tag{49}$$

where, * represents complex conjugate, and $\mathbf{e}_{n,i'}$ is the eigen vector for mode n assigning the direction and displacement magnitude of atom i'. From the inverse of the operations in Eq. (49), we can describe the force on atom i' coming from the atoms on the other side of the interface as the summation of individual contributions by different modes of vibration in the system as,

$$\mathbf{F}_{i'} = \sum_{n} \frac{1}{\sqrt{N m_{i'}}} \mathbf{e}_{n,i'} \Xi_n \tag{50}$$

Then, replacing Eq. (50) in the definition for interfacial heat flux (Eq. (48)) results in the following definition, which is the contribution by mode of vibration n to the total interfacial heat flux derived from the force decomposition approach,

$$Q_n = \frac{1}{\sqrt{N}} \sum_{i'} \frac{\mathbf{p}_{i'}}{m_{i'}} \cdot \left(\frac{1}{\sqrt{N m_{i'}}} \mathbf{e}_{n,i'} \Xi_n \right) \tag{51}$$

Once implemented, we conducted a simple test simulation, whereby we only excited one mode of vibration in the system (*e.g.*, an extended mode at 4.61THz) by giving initial displacements to the atoms from their equilibrium position according to the eigen vectors belonging to that specific mode of vibration. The maximum initial displacement attributed to an atom to excite this mode of vibration was chosen to be small enough $\left(\sim 0.0001\mathring{A}\right)$ to make sure that no other mode of vibration becomes excited after the simulation begins. Nonetheless, we checked the frequency content of the system during the simulation and confirmed that our initially excited mode of vibration at the intended frequency of 4.61THz is indeed the only mode of vibration present in the system. Therefore, any physically meaningful scheme for modal decomposition should predict absolutely zero contributions for all modes of vibration in the system except for the one that was initially excited at the frequency of 4.61THz.

Figure 10 shows the modal contributions to the heat flux from the velocity and force decomposition approaches for a single snapshot in time during our simulation. It can be seen from Figure 10b that a number of non-zero contributions to heat flux have been calculated by force decomposition approach for frequencies that in reality do not even exist in our structure. The fact that we observe non-zero contributions from non-existent frequencies shows that the force decomposition does not correctly attribute the heat flux to the correct modes, since by construction, the only mode that can contribute is the one that is excited. Therefore, the force decomposition approach should not be used for modal

analysis. Furthermore, we have confirmed that velocity decomposition correctly predicts only one non-zero contribution at all times during the simulation, which indeed belongs to the only existing mode of vibration in the system at 4.61THz (see Figure 10a) and is consistent with our physical intuition. Therefore, the authors believe that the velocity decomposition is the only technique that is both mathematically and physically meaningful.

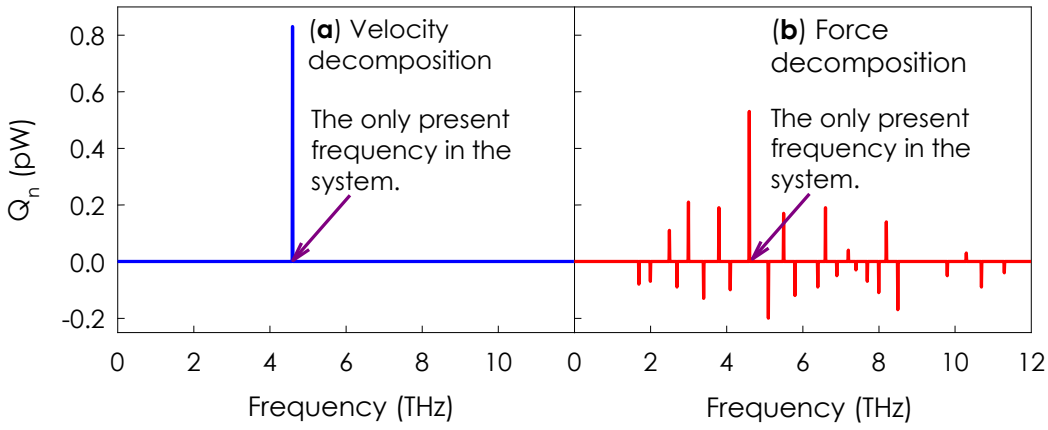

Figure 10 – Calculated modal contributions to heat flux (Q_n) by (a) velocity and (b) force decomposition approaches, for one instant of time, for the InP/InGaAs interface when there is only one mode of vibration (extended mode with the frequency of 4.61THz) is excited in the simulation.

CHAPTER 4. CLASSIFICATION OF THE MODES OF VIBRATION AT THE INTERFACE OF TWO MATERIALS

After establishing the correct choice of modes in the previous chapter, we turn our discussion to a deeper examination of the modes contained in the {AB} basis set. The interface itself acts as a compositional discontinuity that breaks the system's symmetry and changes the LD dynamical matrix in such a way that not all solutions can retain sinusoidally modulated eigen vectors for all of the atoms. Therefore, not all of the modes from the {AB} basis set correspond to propagating modes. Furthermore, since atoms near the interface have different dynamical matrix elements than the rest of the system, some of the eigen solutions become localized to the interfacial region (*i.e.*, similar to localization of vibrational modes near defects).[107] Given that some degree of localization is to be expected, new mode classifications can emerge. One can then envision developing a mode classification scheme based on the degree to which modes are localized to a given portion of the system. For example, Eqns. (36) and (37) indicate that a mode can only contribute substantively to the heat flow, if it includes participation (*e.g.*, significant eigen vectors) from atoms near the interface. Thus a mode with zero eigen vectors for the atoms near the interface will by definition have zero contribution to the heat flow and therefore zero contribution to the TIC. Also, a mode that can extend through both sides of the interface and deeply into both materials has a greater likelihood of exhibiting longer correlation times, resulting in larger contributions to the TIC (see Eq. (32)). From this perspective, one might obtain new and interesting insights by classifying the modes in the {AB} basis set according to (1) the degree of delocalization into both materials, (2) the degree of

localization in one material, (3) the degree of participation near the interface, or (4) the degree of localization near the interface.

We have tentatively classified the 3N solutions in the {AB} basis set into 4 distinct categories based on the region where they are most localized: <1> extended modes, <2> partially extended modes, <3> isolated modes and <4> interfacial modes. The criterion for classifying the modes in the LD calculation of the {AB} basis set is based on the answers to 2 questions motivated by inspection of Eqns. (36) and (37), namely:

1. Does the mode of vibration exhibit participation near the interface?
2. Is the mode of vibration localized to any particular part of the system?

These two questions are motivated from the fact that if a mode does not exhibit significant participation in the interfacial region, it cannot exhibit a significant contribution to the interfacial heat flow or TIC. Conversely, if the majority of its vibrations are localized to the interfacial region, it can exhibit a significant contribution. Also, if a mode is delocalized across the interface and extends through both materials it has a higher likelihood of exhibiting longer correlation times, which could lead to larger TIC contributions.

From LD calculations for the {AB} basis set, eigen vectors are defined for all the atoms and since we are interested in classifying eigen modes based on their vibrations with respect to the interface, we have defined four participation parameters (PP) to measure the magnitude of the eigen vectors for each atom in a given mode. The first PP sums the eigen vector magnitudes for eigen mode n in the entire structure (PP_{tot}^{n}). The second PP sums the eigen vector magnitudes for eigen mode n inside the interface region (PP_{int}^{n}), which is

shown in Figure 11. The third and fourth PP sums the eigen vector magnitudes for eigen mode n for side A, PP_A^n, and side B, PP_B^n, respectively. To define the interface region, we simply used a cutoff value, such that whenever the distance between an atom and the interface plane is less than x_{cut} (see Figure 11), the atom is considered inside the interface region. IN our classifications for the modes of vibration in the LJ and diamond systems, the cut off value was taken to be equal to two lattice constants. PP_{tot}^n, PP_{int}^n, PP_A^n, and PP_B^n for an eigen mode n are then defined as follows,

$$PP_{tot}^n = \sum_{i \in \text{entire system}} \left| \mathbf{e}_{n,i} \right| \tag{52}$$

$$PP_{int}^n = \sum_{i \in \text{interface region}} \left| \mathbf{e}_{n,i} \right| \tag{53}$$

$$PP_A^n = \sum_{i \in A} \left| \mathbf{e}_{n,i} \right| \tag{54}$$

$$PP_B^n = \sum_{i \in B} \left| \mathbf{e}_{n,i} \right| \tag{55}$$

The comparison of relative magnitudes for these four quantities are then used to classify each eigen mode n as one of the four types, based on answers to a series of questions. First, to answer the question: *"Is the mode present at the interface?"*, we require PP_{int}^n to be a significant fraction of PP_{tot}^n (*e.g.*, more than 0.1%), which leads to the requirement that $PP_{int}^n / PP_{tot}^n > 0.001$. To then answer the question: *"Is the majority of the vibration at the interface?"* we require that more than half of the vibrations be located within the interface region, which is mathematically expressed as the condition

$PP_{int}^{n} / PP_{tot}^{n} > 0.5$. To then determine *"Is the mode localized to side A"* or *"Is the mode localized to side B?"*, we require that one side of the interface exhibit at least 10 times larger portion of the vibrations (*e.g.*, more than 90% of the vibration is on one side of the interface). This is then expressed mathematically as $PP_{A}^{n} / PP_{B}^{n} > 10$ to be localized on side A and $PP_{B}^{n} / PP_{A}^{n} > 10$ to be localized on side B. Thus we then require $PP_{A}^{n} / PP_{B}^{n} \le 10$ and $PP_{B}^{n} / PP_{A}^{n} \le 10$ for delocalized modes. The four mode classifications are then defined by the following answers to the preceding questions and are summarized below using the corresponding mathematical statements:

Modes of type <1> are present at the interface, but the majority of the vibration is not at the interface, and they are delocalized into both materials.

Modes of type <2> are present at the interface, but the majority of the vibration is not at the interface, and they are localized on one side of the interface.

Modes of type <3> are not present at the interface.

Modes of type <4> have the majority of their vibration at the interface.

$$\begin{cases} PP_{int}^{n} / PP_{tot}^{n} > 0.001 \\ PP_{int}^{n} / PP_{tot}^{n} < 0.5 \\ PP_{A}^{n} / PP_{B}^{n} \le 10 \\ PP_{B}^{n} / PP_{A}^{n} \le 10 \end{cases}, \quad \text{mode } n \text{ is type <1>} \tag{56}$$

$$\begin{cases} PP_{int}^{n} / PP_{tot}^{n} \ge 0.001 \\ PP_{int}^{n} / PP_{tot}^{n} \le 0.5 \\ PP_{A}^{n} / PP_{B}^{n} > 10 \end{cases}, \quad \text{mode } n \text{ is type <2> present in side A} \tag{57}$$

$$\begin{cases} PP_{int}^{n} / PP_{tot}^{n} \geq 0.001 \\ PP_{int}^{n} / PP_{tot}^{n} \leq 0.5 \\ PP_{B}^{n} / PP_{A}^{n} > 10 \end{cases}, \quad \text{mode } n \text{ is type <2> present in side B} \tag{58}$$

$$\text{mode } n \text{ is type <3> if it is not <1>, <2>, or <4>} \tag{59}$$

$$PP_{int}^{n} / PP_{tot}^{n} > 0.5, \quad \text{mode } n \text{ is type <4>} \tag{60}$$

With this classification scheme every eigen solution falls uniquely into one type and it is to be reiterated that the taxonomy introduced herein is preliminary. Additional studies are needed to determine the extent to which these mode definitions should be revised or expanded and whether or not these classifications serve as useful descriptors for the TIC.

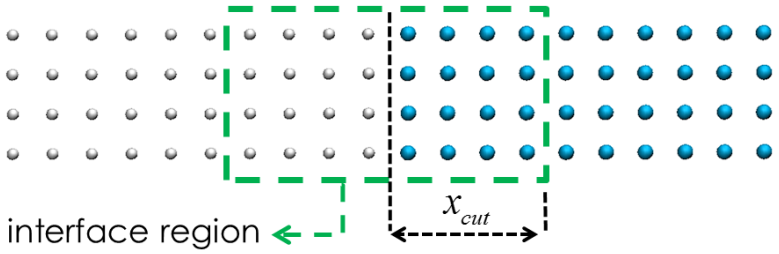

Figure 11 – Interface region. x_{cut} assigns the span of the interface region around the interface. For this study the value of x_{cut} has been chosen equal to 10Å, which is equivalent to the LJ cut-off. For the diamond Si system, the cutoff was equal to two lattice constants.

For the interface of two LJ solids (*e.g.*, the interface of a solid argon and a fictitiously heavier solid argon with four times the mass of real argon), Figure 12 shows examples of each of the four types of modes, and Figure 13 shows their respective density of states. Extended modes (type <1>) are delocalized over the entire system (Figure 12a)

and because both sides (A and B) vibrate at one frequency, their density of states has a sharp cutoff at $\omega_{max,B}$ (Figure 13). Partially extended modes (type <2>) vibrate on one side of the interface and only partially extend through to the other side (Figure 12b). These modes comprise the majority of the eigen solutions (see Figure 13). Isolated modes (type <3>) exist on one side of the interface, but do not include participation near the interface (Figure 12c). Interfacial modes (type <4>) are localized/peaked near the interface (Figure 12d) and they make up a small portion (0.3%) of the density of states, yet they play a significant role in the transport. The contributions to the TIC for each mode type are: 42.87% (extended), 53.20% (partially extended), 0.55% (isolated), and 3.16% (interfacial). This indicates that, despite their low population, interfacial modes have the highest contribution on a per mode basis (10X higher than the average contribution per mode $G_{Total}/3N$).

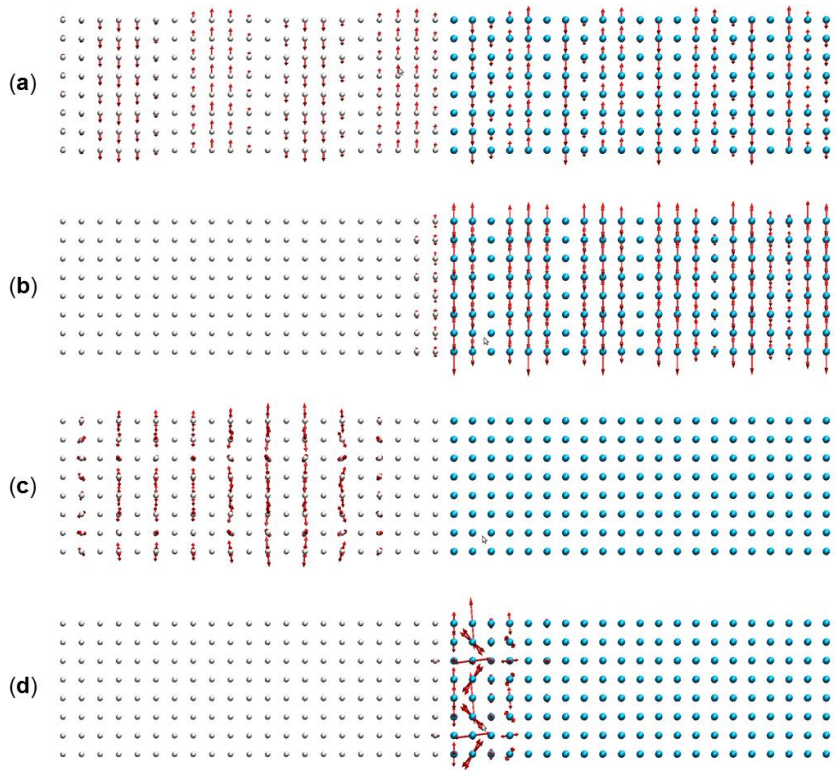

Figure 12 – Examples of the four classifications of eigen modes identified for the {AB} basis set for the interface of two lattice matched, mass mismatched LJ solids. Each panel shows eigen vector displacements for an example of each type of solution: (a) extended <1>, (b) partially extended <2>, (c) isolated <3>, and (d) interfacial <4> modes. The frequencies of vibration for these for examples of eigen modes of vibration are 0.34THz, 0.68THz, 0.96THz, and 0.47THz respectively.

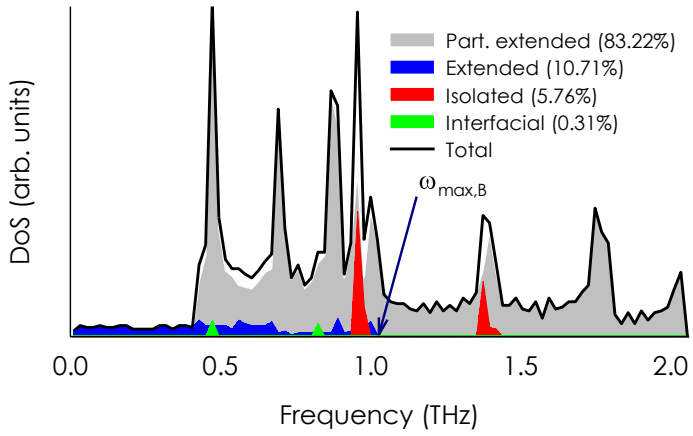

Figure 13 – DOS and population (i.e., percentage of the total number of modes) for the four classifications of eigen modes identified for the {AB} basis set for the interface of two lattice matched, mass mismatched LJ solids.

To confirm that these mode classifications are not just a peculiar artifact of the LJ system, we have also performed the same calculations on the interface of diamond Si with another diamond Si structure but with a fictitiously 4X larger mass than real Si. The atomic interactions are modeled with the Tersoff potential, where the interaction parameters are the same for both sides. LD calculations for such interfaces, as well as for interfaces where both the parameters and masses are different (*i.e.*, corresponding to Si-Ge), again revealed the same 4 classifications of modes. Furthermore, all studies to date of different interfaces have yielded the same behaviors and conclusions, with regards to the mode classifications.

CHAPTER 5. THE IMPORTANCE OF ANHARMONICITY

Up to now, no model has been able to quantify the true effect of anharmonicity on the heat transfer across interfaces. Some reports have reasoned that inelastic interactions across interfaces play a critical role in interfacial heat transfer,[56,67] however others have questioned the significance of anharmonic effects.[20] ICMA formalism is based on MD simulations and now has the capability to automatically include the anharmonicity into the calculations to its full order. Such a feature in ICMA technique allows for direct evaluation of anharmonic contributions to TIC, which can potentially settle all previous debates about the importance of anharmonicity.

Harmonic interactions can only transfer energy between modes of vibration that have equal frequencies, as is known from continuum mechanics.[108,109] Therefore, any contribution to interfacial heat transfer by a mode of vibration that has a frequency higher than the maximum frequency of vibration belonging to the bulk of the heavier or weaker side of the interface (*i.e.*, $\omega_{max,B}$) can only be attributed to the anharmonic interactions.

Previous reports have investigated the effect of temperature on TIC, however none of them have been able to study how the modal contributions and anharmonicity vary with temperature. Using ICMA, we investigated the effect of temperature on the modal contributions and anharmonic interactions across the interface of two LJ solids (*i.e.*, the interface of solid argon and a fictitious solid argon with a mass 4X the real mass of argon). The TIC accumulation functions at four different temperatures are calculated and shown in Figure 14. It can be seen that purely harmonic interfacial heat transfer is only present at

temperatures as low as 1K, where there is no contribution to TIC beyond $\omega_{max,B}$. Interestingly, at only slightly elevated temperatures, anharmonic interactions quickly become a major contributor to the TIC, where 18%, 23% and 21% of the contributions to TIC at temperatures 10K, 30K and 60K respectively are directly obtained from frequencies larger than $\omega_{max,B}$, which proves the significance of anharmonicity in the interfacial heat transfer across these interfaces. It is also important to note that at higher temperature it is also very possible that contributions below $\omega_{max,B}$ can also be associated with anharmonicity. However, currently a method for separately assessing/distinguishing the two parts is non-existent. Nonetheless, in Figure 10, one could conjecture that the contributions between 0.5-1.0 THz above 10K might also be affected by anharmonicity since they are higher than the contributions at 1K in the same frequency range. The similarity in the contributions below 0.5 THz at all temperatures also supports this possibility, but it remains to be confirmed by a more rigorous assessment.

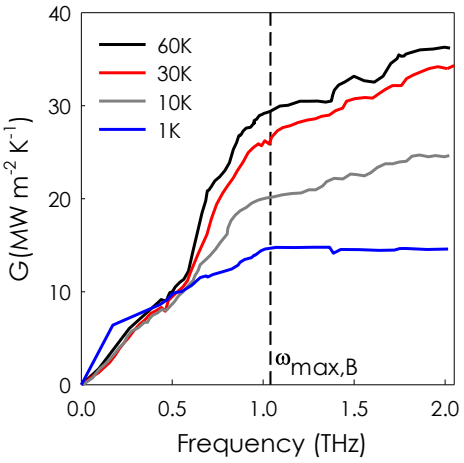

Figure 14 – TIC accumulation functions at the interface of two LJ solids calculated at different temperatures. $\omega_{max,B}$ represents the maximum frequency of the heavier side of the interface.

In addition to the interface of LJ solids, we have also studied the anharmonic contributions to the TIC across a number of more realistic interfaces at above cryogenic temperatures. Our investigated structures include the interface of (1) Si and fictitiously heavier Si with a mass 4X the real mass of Si, (2) Si and germanium (Ge) structures with all the possible variations in the crystallinity of the solids (*e.g.*, crystalline (henceforth denoted by the prefix c-) or amorphous (henceforth denoted by the prefix a-)), and (3) InP and InGaAs structures. The calculated modal contributions are shown in Figure 15 in the form of TIC accumulation functions. All the contributions to the TIC above $\omega_{max,B}$ is attributed to the anharmonic interactions. For InP/InGaAs interface, because of the phononic bandgap in InP structure (see Figure 16) no overlap of vibrational frequencies between the two sides is seen beyond 5.7THz. Therefore, all the contributions to the TIC for InP/InGaAs interface by frequencies higher than 5.7THz are caused by anharmonic interactions. Figure 15 clearly shows that except cSi/aSi and cGe/aGe interfaces, anharmonicity has at least 18% contribution to the TIC across all the other interfaces. For some reason that will be investigated later the harmonic contributions dominate the interfacial heat transfer across cSi/aSi and cGe/aGe interfaces. These results again support the significance of including anharmonic interactions into calculations.

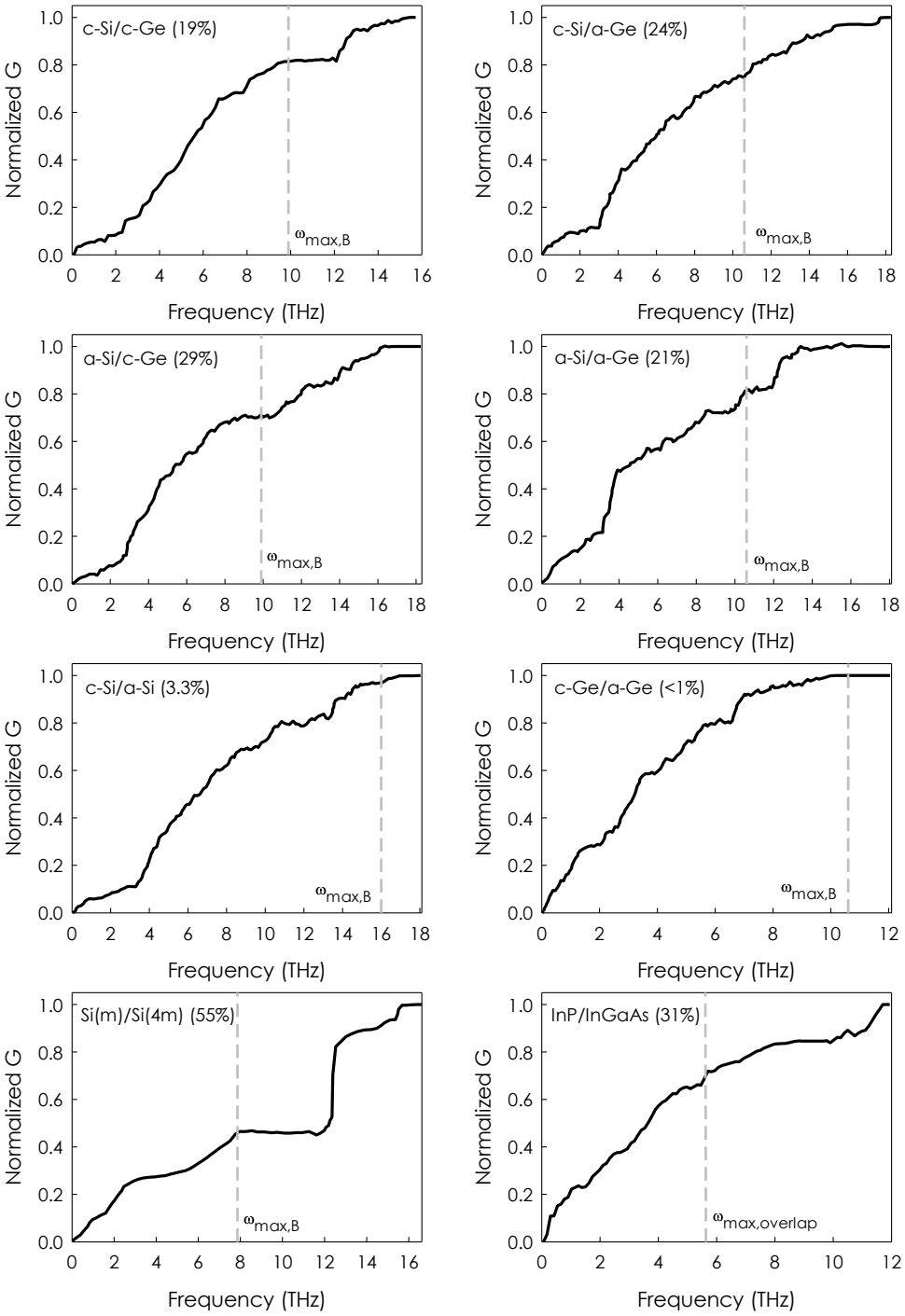

Figure 15 – TIC accumulation functions for eight different interfaces. Anharmonic contributions are present at frequencies higher than the maximum frequency of vibration at the bulk of the heavier/weaker side of the interface (denoted here by $\omega_{max,B}$). For InP/InGaAs interface anharmonic contributions are present at frequencies above the beginning of the InP bandgap (denoted here by $\omega_{\max,\text{overlap}}$) above which no overlap of frequencies exists between the two sides.

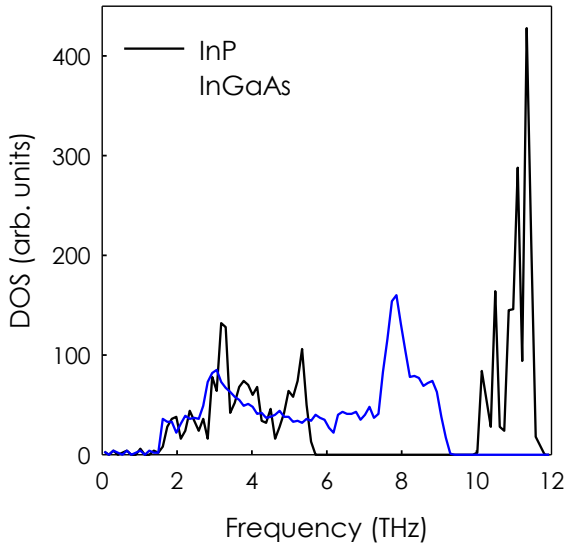

Figure 16 – Density of states (DOS) for the bulk InP and InGaAs structures.

5.1 Correlation Mapping

The ICMA formalism is not only able to quantify the anharmonic contributions across interfaces, but it also has the ability to elucidate the underlying mechanisms of heat transfer through interfaces. Using ICMA, we can examine the extent of correlation/interaction between different modes through a 2D mapping of $G_{n,n'}$ correlations (Figure 17) using Eqns. (35), (36) and (37). Here, we examine the interface of two LJ solids to understand the modal interactions/correlations in more detail. We calculated the 2D matrix of $G_{n,n'}$ correlations for different mode classifications as color maps (see Figure 17). Since elastic interactions are restricted to phonons of the same frequency, which are only associated with the values along the diagonal of the correlation map, all the off-diagonal contributions are attributed to the anharmonicity. Generally, the magnitude of auto-correlations ($n = n'$) is much larger than the cross-correlations ($n \neq n'$), therefore, removing auto-correlations from Figure 17a presents a clearer view of the

details of the cross-correlations (*i.e.*, anharmonic interactions) as shown in Figure 17b. All of the $G_{n,n'}$ plots in Figure 17 are symmetric about the diagonal, and examination of the plots leads one to notice interesting features that naturally emerge from the modal interactions. What is particularly interesting is that when analyzed with the {AB} basis set, features emerge at locations where mode character changes. For instance, in the LJ system, there is a region of minimal correlation in the frequency range 0.4-1.0 THz. Here, 0.4 THz corresponds to the onset of localization (Figure 13), where the first partially extended mode appears. Below 0.4 THz all of the modes extend through the entire structure. Interestingly, 1.0 THz corresponds to $\omega_{max,B}$, whereby modes that extend into the bulk of the heavier side B cease to exist, since the bulk of side B cannot support higher frequency vibrations. The fact that distinct features in the mode-mode correlation are observed where the mode character changes is a further indication that the four classifications are meaningful. The majority of the modes present in the 0.4-1.0 THz frequency band are partially extended modes (type <2>) that primarily exist on the heavier side of the interface (side B) and these partially extended modes exhibit much smaller correlations with other modes in the system, yet they contribute more than 25% to the TIC (see Figure 14). Also, interfacial modes show the strongest correlation/interaction with the low frequency extended modes and higher frequency partially extended modes on the lighter side (side A). This leads us to conjecture that interfacial modes may help facilitate the transfer of the energy between low frequency extended modes and high frequency partially extended modes on the lighter side (side A) and vice versa. If true, these modes could serve as an important bridge for inelastic interactions, whereby modes with frequencies above $\omega_{B,\max}$ transfer their energy to interfacial modes at lower frequencies, which then transfer the energy into extended modes

at even lower frequencies so it can propagate into the heavier side (side B). If true, this pathway provides a new physical picture for how interfacial transport can occur

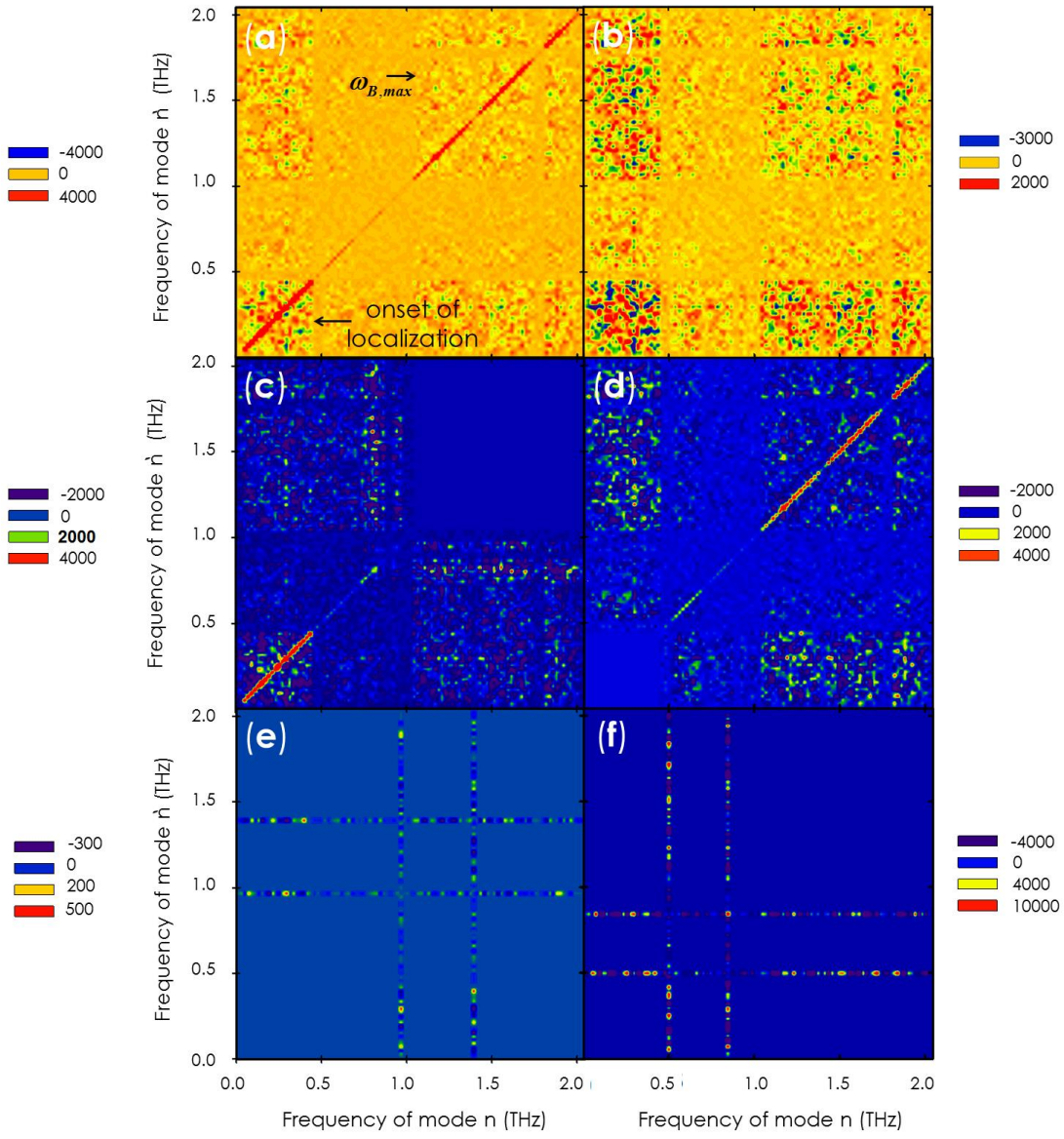

Figure 17 – Correlation contributions to TIC between eigen modes n and n', $G_{n,n'}(W\ m^{-2}\ K^{-1})$, at the interface of two lattice matched, mass mismatched LJ solids. The complete set of auto- and cross-correlations are in panel (a). Panel (b) shows only the cross-correlations after the auto-correlations have been artificially set to zero from the full set of correlations. (c-f) show correlations between the entire set of modes and the four classifications of vibrational modes (e.g., types <1>-<4>). (c) shows <1> extended mode correlations (d) shows <2> partially extended correlations (e) shows <3> isolated mode correlations and (f) shows <4> interfacial mode correlations.

CHAPTER 6. APPLICATION OF ICMA TO DIFFERENT EXAMPLE OF INTERFACES

6.1 Crystalline Si/Ge interface: Role of interfacial modes of vibration

Silicon-germanium (Si-Ge) is a prototypical system that has been studied extensively in the literature, largely due to its applications in thermoelectrics.[110,111] Amongst the extensive literature on Si/Ge interfaces, most studies have not been focused specifically on the modal contributions or do not include inelastic scattering,[21,23,29,94,112-115] except the recent studies by Chalopin and Volz [64] and Murakami *et al.*[116] Chalopin and Volz [64] where they calculated the anharmonic spectral contributions to thermal transport across Si/Ge interfaces. Their results showed a significant contribution to TIC by frequencies around 14 THz. They suggested such a large contribution could be due to localized and non-dispersive interface modes [64] and a similar observation has also been reported by Murakami *et al.*[116] In this section, we reexamine heat conduction at strained-lattice matched, atomically smooth interfaces between crystalline Si-Ge structures with the ICMA method and new techniques for quantifying the mode level anharmonicity to better understand these contributions. Using the two techniques together allowed for deeper understanding of the nature of interfacial modes and ultimately provided a new framework for interpreting their contributions. The key distinction from previous work is the ability to conduct individual mode level assessments of not only TIC, but also each mode's harmonic vs. anharmonic energy.

Using these techniques, we determined that the large contributions reported by Chalopin *et al.* [64] and Murakami *et al.* [116] are associated with modes that have amplified magnitudes of vibration for the atoms around the interface, but still extend through the bulk of the Si side (the eigen vectors belonging to the modes of vibration are shown in Figure 20). Furthermore, these modes only comprise < 0.1% of the total number of modes, yet their contributions are quite substantial. We show that the large contribution by these interfacial modes originates from their high tendency to couple to almost all other modes of vibration in the system. In addition, we examine the mechanism underlying their ability to couple so strongly using a new formulation that allows for the calculation of mode-level harmonic and anharmonic energy distributions amongst the atoms in the system.

Here, the ICMA method is employed in EMD.[105] The Tersoff potential [106] is used to describe the interactions between the atoms in the system. For both Si and Ge sides, the number of unit cells along x, y, and z directions are chosen to be equal to 3, 3, and 24, respectively. The interface is a plane perpendicular to the z direction, which is parallel to the [100] crystallographic direction. Periodic boundary conditions are applied to all 3 spatial directions, and a finite time step of 0.5 fs is chosen for the MD simulations. After relaxing the structure under the isobaric-isothermal ensemble (NPT) for 1 ns at zero pressure and the canonical ensemble (NVT) for another 1 ns at $T = 300K$, we simulate the structure in the microcanonical (NVE) ensemble for 10 ns during which the modal contributions to the heat flux across the interface are calculated. The heat flux contributions are saved and post processed to calculate the mode-mode heat flux correlation functions.[105] Statistical uncertainty, due to insufficient phase space averaging, has been reduced to less than 5% by considering 10 independent ensembles for each case.[104] All MD simulations

were conducted using the Large-scale Atomic/Molecular Massively Parallel Simulator (LAMMPS) package [117] and the eigen modes for each structure were determined from LD calculations using the General Utility Lattice Program (GULP).[118] The Tersoff force routine in LAMMPS was modified to include the modal decomposition of the heat flux across the interface, which allows the modal contributions to be computed concurrently with the trajectory, which is computationally efficient.

The DOS of the four classes of vibration as well as their population as the fraction of the total number of states ($\overline{DOS}$) are shown in Figure 18 and Table 1, respectively. It can be seen that the formation of the interface caused more than 2.5% of the modes to become localized near the interface, even though the entire system is crystalline and lattice matched.

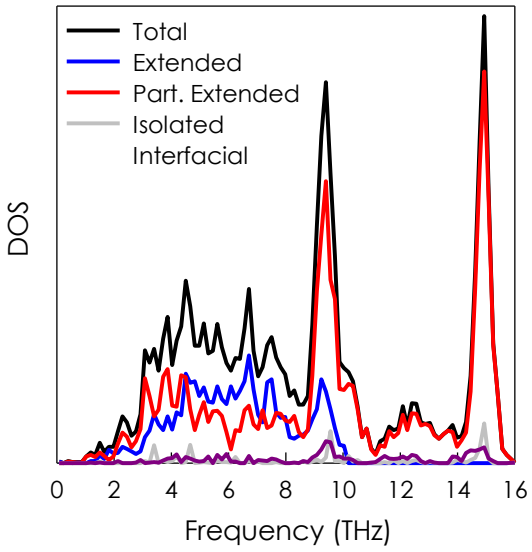

Figure 18 – DOS of the modes of vibration across the crystalline Si/Ge interface. Summation of the DOS for different classes of vibration (colored curves) are equal to the total DOS (black curve)

Table 1 – Number of states for the four different classes of vibration and their contribution to TIC across the Si/Ge interface. Columns 2-4 represent the fraction of the total number of states ($\overline{DOS}$), the percentage contribution to G ($\overline{G}$), and contribution to G divided by fraction of total number of states (i.e., contribution to G per mode) ($\overline{G}/\overline{DOS}$), respectively.

Mode Type	$\overline{DoS}(\%)$	$\overline{G}(\%)$	$\overline{G}/\overline{DOS}$
Extended	29.35	51.99	1.77
Partially extended	64.24	29.28	0.45
Isolated	3.50	< 0.01	< 0.01
Interfacial	2.90	18.73	6.45

Table 1 shows modal contributions to TIC associated with each class of vibration. The results show that interfacial modes have the highest contribution to TIC on a per mode basis (*e.g.*, here 6.5X higher than the average contribution per mode). The accumulation function for TIC is then shown in Figure 19a. The accumulation is interesting because it shows a steep increase between 12-13 THz. The large contribution of the modes in 12-13 THz region to TIC is both interesting and non-intuitive, because as Figure 18 shows, it does not correspond to a region where there is a large population of modes, as would be expected for rapid increase in the accumulation at high frequencies. Similar features in the modal contributions to TIC have been observed by Chalopin and Volz [64] and Murakami *et al.*[116] However, using ICMA we can now pinpoint exactly which normal modes are responsible for this portion of the TIC and we can examine their characteristics to look for deeper insights.

LD of the combined structure revealed that 12-13 THz region is comprised of large contributions from six special interfacial modes, which comprise < 0.1% of the all the modes, yet they are responsible for approximately 15% of the TIC (Figure 19a). Figure 20 shows pictures of the eigen vectors associated with this small group of six modes, which indicates that many of them extend through the bulk of the Si side, but have a predominant portion of their energy/vibration (~20%) at the interface (see the next subsection on how to calculate the energy distribution of one eigen mode over different atoms in the system). Furthermore, since the frequency of these interfacial modes are above the maximum frequency of the bulk Ge side (~ 10THz) their contribution must be the result of inelastic interactions enabled by the system's anharmonicity.[43,105]

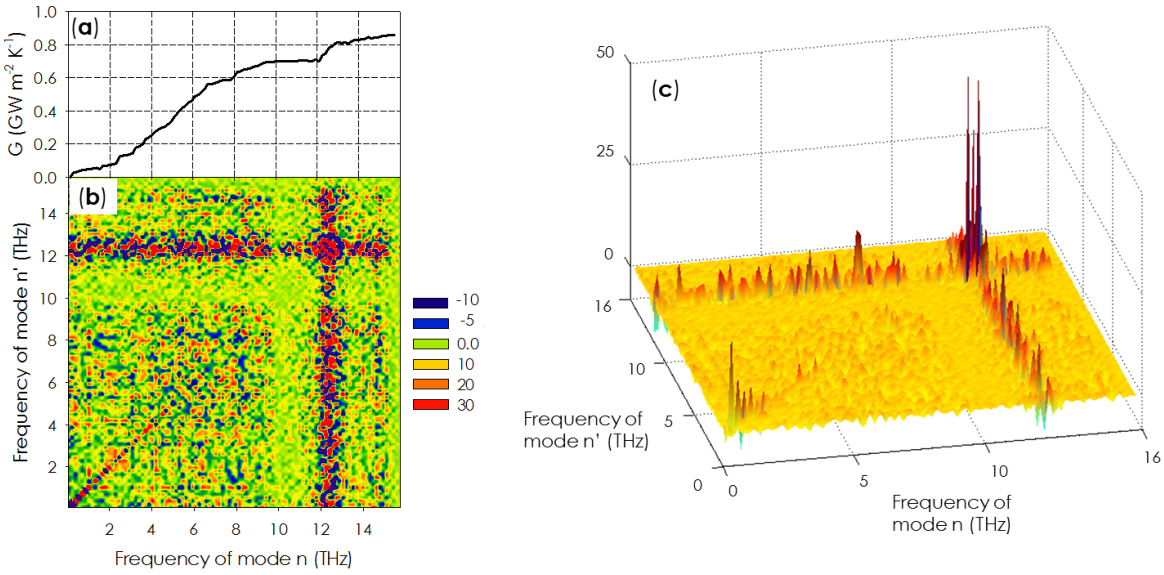

Figure 19 – Modal contributions to TIC for Si/Ge interface at T=300K. (a) TIC accumulation function, (b) 2D map and (c) 3D perspective depiction of the data in (b) showing the magnitudes of the correlations/interactions as elevations above the plane of two frequency axes. The values presented on the 2D and 3D maps have units of $\left(MW\ m^{-2}\ K^{-1}\right)$. Inelastic interactions occur between the modes with frequencies 12-13 THz and all the other modes in the system. Although panel (a) shows that interfacial modes in the frequency range of 12-13 THz contribute almost 15% to the TIC, the summation of the contribution of interfacial modes on the correlation maps of (b) and (c) show that when their affects/correlations with other modes are also included they are, in total, responsible for more than 26% of the total TIC.

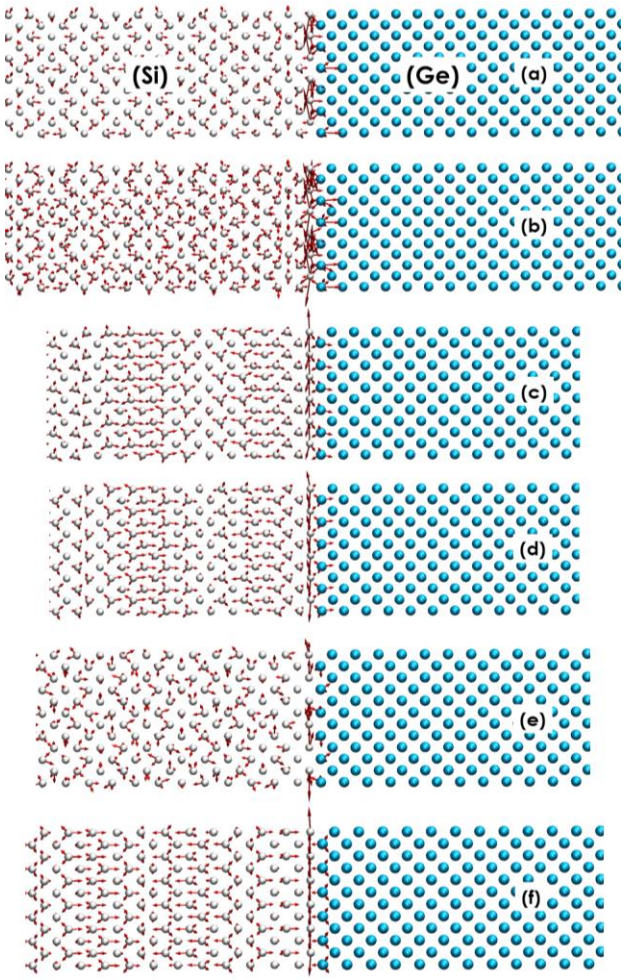

Figure 20 – Eigen vectors for six special interfacial modes in the 12-13THz region that comprise near 15% of the TIC. The frequencies of these eigen modes are (a) 12.01THz, (b) 12.01THz, (c) 12.10THz, (d) 12.10THz, (e) 12.25THz, and (f) 12.32THz. Si and Ge atoms are shown with white and cyan spheres respectively.

Using ICMA, the degree of interaction/correlation between each pair of vibrational modes in the system can be calculated and presented as a two-dimensional map of correlation,[43,105] shown in Figure 19b. Since elastic interactions are restricted to phonons of the same frequency, which are only associated with the values along the diagonal of the correlation map (Figure 19b), all the off-diagonal contributions are attributed to the anharmonicity. The 2D mapping shows that the interfacial modes between 12-13THz are strongly correlated with all others and their correlation is at least 1 order of magnitude

larger than the average correlation outside this regime (see Figure 19c for the 3D representation of the correlations).

Since the highly contributing modes of vibration shown in Figure 20 have relatively large frequencies (~12-13THz), one could suspect their contribution to TIC at room temperature to be partially suppressed by their reduced heat capacity. However, even after such quantum effects are accounted for [43] at T=300K, the interfacial modes of vibration at 12-13THz still contribute 12% to TIC (Figure 21b). Additionally, the modal contributions to TIC at higher temperatures (400K and 500K (Figure 21a-b)) show that interfacial modes still contribute 15% to the TIC, which confirms that for applications at room-temperature and above, interfacial modes maintain their contribution to TIC.

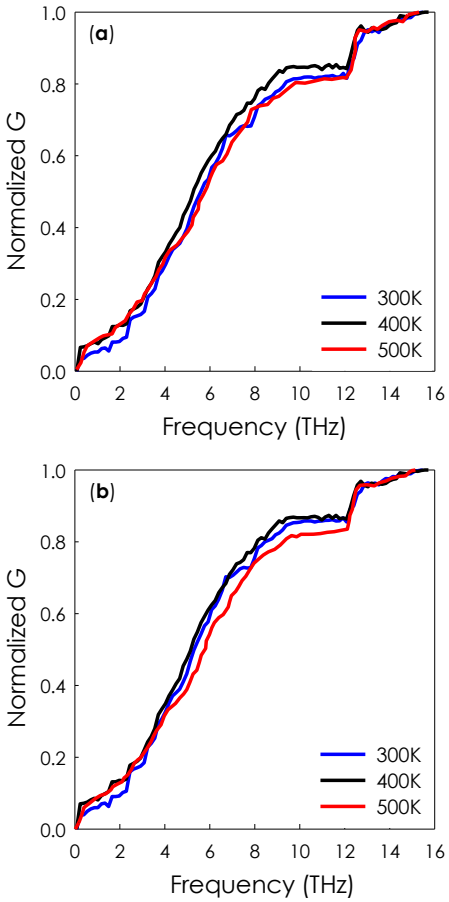

Figure 21 – Normalized modal contributions to TIC for Si/Ge interface at three different temperatures of 300K, 400K, and 500K (a) before quantum correction and (b) after quantum correction. The absolute values of TIC before quantum correction for 300K, 400K, and 500K are 0.84 $GWm^{-2}K^{-1}$, 0.87$GWm^{-2}K^{-1}$ and 0.88 $GWm^{-2}K^{-1}$, respectively. The absolute values of TIC after quantum correction for 300K, 400K, and 500K are 0.80 $GWm^{-2}K^{-1}$, 0.83$GWm^{-2}K^{-1}$ and 0.86 $GWm^{-2}K^{-1}$, respectively.

It is also important to note that if such a large contribution to the conductance is associated with a narrow range of frequencies for a real system, such a distinct feature could potentially be verified by measuring the TIC vs. temperature (*i.e.*, using transient thermoreflectance techniques [119,120]). The data in Figure 22 supports this idea by showing the effect of interfacial modes on the TIC accumulation function. It can be seen that by removing the entire contribution of interfacial modes (*e.g.*, by excluding all the points corresponding to interfacial modes on the correlation maps) the sharp increase at the

frequency range of 12-13THz disappears and the TIC accumulation function follows a smooth increase vs. frequency. Moreover, the exclusion of interfacial modes results in a noticeably different temperature dependence for the TIC when quantum corrections are applied, which can form a basis for the experimental evaluation of the existence of the reported interfacial modes in the 12-13THz frequency region.

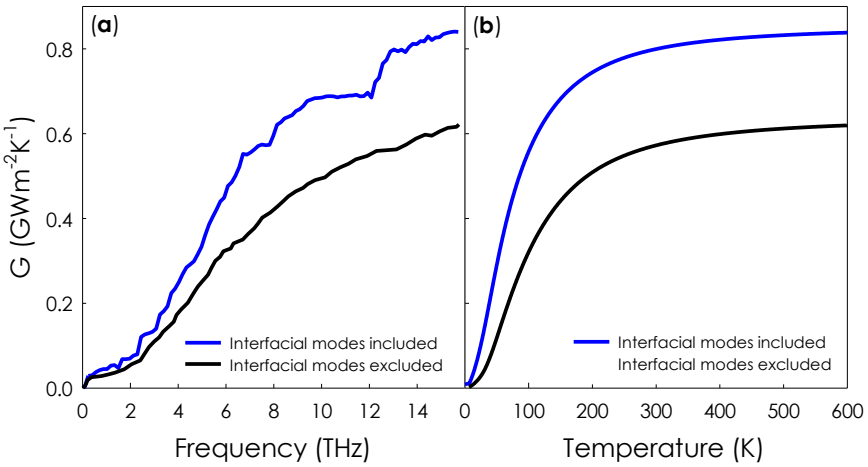

Figure 22 – Effect of excluding the contribution by interfacial modes at the frequency range of 12-13THz on (a) the TIC accumulation function and (b) the temperature dependence of TIC at the interface of crystalline Si/Ge. It should be noted that according to the correlation maps shown in Figure 19, the contribution/effect by interfacial modes is not limited to the narrow frequency region of 12-13THz and is in reality distributed all over the frequency spectrum. Transient thermoreflectance measurement techniques can potentially detect the decrease in TIC after the exclusion of interfacial modes, which can serve as an experimental basis for evaluating the existence of these modes.

6.1.1 Calculating harmonic and anharmonic energy distributions for modes

To understand how the interfacial modes between 12-13 THz couple to virtually all other modes, we compute the degree of anharmonicity sampled by different atoms at different locations in the structure (see Figure 23) based on the following procedure. The

potential energy for an oscillator can be written as arising from the sum of harmonic and anharmonic contributions,

$$\left\langle H_{pot} \right\rangle = \left\langle H_{harmonic} \right\rangle + \left\langle H_{anharmonic} \right\rangle \tag{61}$$

where $\langle \cdots \rangle$ represents the ensemble average.[104] The anharmonic portion represents the deviation of the potential energy of the system from its largest component which is the harmonic term. We are interested in calculating how the harmonic and anharmonic portions of the energy for an oscillator are distributed amongst the different atoms in the system. Based on the equipartition theorem, the average harmonic energy of a classical oscillator is equal to,

$$\left\langle H_{harmonic} \right\rangle = \frac{1}{2} k_B T \tag{62}$$

where k_B is the Boltzmann constant, and T is the temperature of the system. The potential energy for a harmonic oscillator can also be calculated from the normal mode amplitude analysis via,[11]

$$\left\langle H_{harmonic} \right\rangle = \frac{1}{2} X_n{}^2 \omega_n{}^2 \tag{63}$$

where X_n is the modal displacement coordinate, and ω_n is the frequency of the eigen mode. It should be noted that calculating the harmonic energy for an eigen mode using the knowledge of force constant matrix and the respective atomic displacements for an eigen

mode is equal to the approach based on the normal mode amplitude analysis (Eq. (63)). The modal displacement coordinate can be explicitly written as,[11]

$$X_n = \sum_i \sqrt{\frac{m_i}{N}} \mathbf{e}_{n,i} \cdot \mathbf{u}_i \tag{64}$$

where, N is the total number of unit cells in the system, i is the atom index, m_i is the mass of atom i, $\mathbf{e}_{n,i}$ is eigen vector associated with atom i for eigen mode n, and $\mathbf{u}_i$ is the displacement of atom i. By combining Eq. (62) and Eq. (63) we then have,

$$X_n{}^2 \omega_n{}^2 = k_B T \tag{65}$$

To determine the distribution of the harmonic energy for eigen mode n amongst the atoms in the system, one can envision a state of the system whereby all of the atoms in the system are displaced from equilibrium in the direction of their respective eigen vectors from mode n (i.e., $\mathbf{e}_{n,i}$). In this view, the attributed displacement to an atom would be equal to,

$$\mathbf{u}_i = \alpha_n \mathbf{e}_{n,i} \tag{66}$$

where α_n is a scaling factor that associates a certain degree of displacement with the mode's amplitude at a given temperature. The exact value of the scaling factor can then be calculated from the combination of Eqns. (64), (65) and (66). Replacing for the atomic displacement in Eq. (64) with the definition in Eq. (66), we would have,

$$X_n = \sum_i \sqrt{\frac{m_i}{N}} \mathbf{e}_{n,i} \cdot \alpha_n \mathbf{e}_{n,i} = \alpha_n \sum_i \sqrt{\frac{m_i}{N}} \mathbf{e}_{n,i} \cdot \mathbf{e}_{n,i} \tag{67}$$

which by the substitution of $X_{i,n} = \sqrt{\frac{m_i}{N}} \mathbf{e}_{n,i} \cdot \mathbf{e}_{n,i}$, yields a simpler form,

$$X_n = \alpha_n \left(\sum_i X_{i,n} \right) \tag{68}$$

Using Eq. (65) we then have $X_n \omega_n = \sqrt{k_B T}$ and by incorporating Eq. (68), we can calculate the scaling factor as,

$$\alpha_n = \frac{\sqrt{k_B T}}{\left(\sum_i X_{i,n} \right) \cdot \omega_n} \tag{69}$$

With this scaling factor (α_n), we then rewrite Eq. (65) as,

$$X_n \; X_n \; \omega_n{}^2 = k_B T \tag{70}$$

and substitute for X_n from Eq. (68), which yields,

$$\left[\alpha_n \left(\sum_i X_{i,n} \right) \right] \left[\alpha_n \left(\sum_{i'} X_{i',n} \right) \right] \omega_n^2 = k_B T \tag{71}$$

$$\sum_i X_{i,n} \left(\alpha_n^2 \right) \left(\sum_{i'} X_{i',n} \right) \omega_n^2 = k_B T \tag{72}$$

Replacing for α_n with its definition in Eq. (69) allows us to rewrite Eq. (72) as,

$$\sum_i X_{i,n} \frac{k_B T}{\left(\sum_{i''} X_{i'',n}\right)^2 \omega_n^2} \left(\sum_{i'} X_{i',n}\right) \omega_n^2 = k_B T \tag{73}$$

and finally,

$$\sum_i \frac{X_{i,n}}{\left(\sum_{i'} X_{i',n}\right)} k_B T = k_B T \tag{74}$$

Eq. (74) defines the harmonic energy attributed to atom i by eigenmode n $\left(\Omega_{i,n}\right)$,

$$\Omega_{i,n} = \frac{X_{i,n}}{\left(\sum_{i'} X_{i',n}\right)} k_B T \tag{75}$$

Through the definition of the scaling factor $\left(\alpha_n\right)$, we can determine the exact displacements for the atoms in the system when exactly one mode is excited. This then allows us to analyze the energy and anharmonicity associated with that single mode, where (according to Eq. (62)) the harmonic energy for eigen mode n is equal to $\frac{1}{2} k_B T$.

An atom's full potential energy contribution to a given eigenmode $\left(\Phi_{i,n}\right)$ is then determined by applying the associated displacements for a specific eigen mode [11] – e.g., the case where it is the only mode excited in the system. This total potential energy includes both the harmonic and anharmonic portions (anharmonic to full order). This is achieved by

writing the total potential energy of the system as the summation over the individual atomic potential energies as,[92,93]

$$\Phi = \sum_i \Phi_i \tag{76}$$

where Φ is the total potential energy and Φ_i is the potential energy assigned to atom i, such that all energy is equally partitioned amongst interacting pairs of atoms.[82,83] Following this method, by applying the displacements associated with a given mode, each individual atom's potential energy can be calculated statically, without having to execute an EMD simulation. For an eigenmode n, the difference between the total potential energy $\left(\Phi_{i,n}\right)$ and the harmonic potential energy $\left(\Omega_{i,n}\right)$ associated with atom i equals the anharmonic portion of the energy $\left(\Upsilon_{i,n}\right)$.

$$\Upsilon_{i,n} = \Phi_{i,n} - \Omega_{i,n} \tag{77}$$

This anharmonic energy can then be used to better understand how modes and regions of atoms interact and ultimately will help to quantify its effect on transport.

If one then sums $\Upsilon_{i,n}$ over all the eigen modes, the result is the total anharmonic energy of atom i and provides insight into the amount of anharmonicity it will experience. We can then sum the anharmonic energy contributions for all of the atoms in a specific region of the system which will provide insight into whether or not the presence of the interface causes different regions of the system experience more or less anharmonicity.

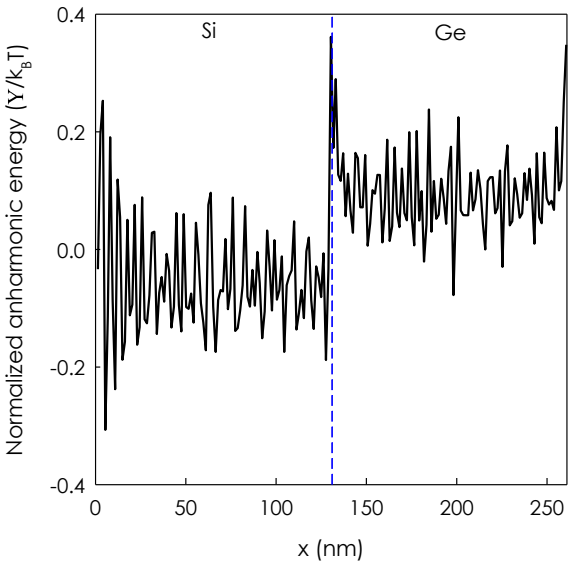

Figure 23 – Average anharmonic energy for the atoms at each layer along the Si/Ge structure normalized by k_BT. The largest peak belongs to the last layer of Si atoms at the interface. The position of the interface is shown by the dashed line.

Figure 23 shows that atoms near the interface experience the largest anharmonic contributions to their energy. This confirms that the presence of the interface increases the extent to which atoms access the anharmonic terms in the energy in certain regions. It should be noted, that by comparison, for a homogenous solid (no interface) the anharmonic energy terms would be uniform and homogenous throughout the entire structure. Thus, a deviation from constant anharmonicity is attributable to the presence of the interface itself. Also, since the interfacial modes hold 20% of their energy in this more anharmonic region, one might immediately assume that the motions associated with these modes must be the most strongly anharmonic. However, from the mode-level contributions to anharmonic energy for the interfacial atoms (see Eq. (77) and Figure 24), it appears that interfacial modes between 12-13THz are not the most notably anharmonic modes in the interfacial region. Nonetheless, they do comprise the predominant portion of the energy in the

interfacial region. Figure 25b shows that more than 30% of the energy for interfacial atoms comes from the interfacial modes with frequencies between 12-13 THz. Thus, despite their small population in the entire system DOS (Figure 18 or Figure 25a), they contribute considerably to the energy of the atoms in the interfacial region (Figure 25b), which matter most for the TIC. We then postulated that other modes, which could be somewhat more anharmonic (see Figure 24), tend to couple their energy from the bulk into these interfacial modes, which have the most energy in the interfacial region. These interfacial modes then facilitate energy transfer through the interface and into the other material. As a result, interfacial modes exhibit extremely strong correlation with all the other modes (Figure 19b and Figure 19c), as they effectively serve as a bridge for the energy to couple across the interface. This supports a new physical picture for describing the contributions of interfacial modes, whereby the energy in other modes couples to the most overall energetic modes in the interfacial region (*e.g.*, interfacial modes), which then move the energy across the interface to the other material, whereby it can couple to other modes that exist in the bulk of the other side.

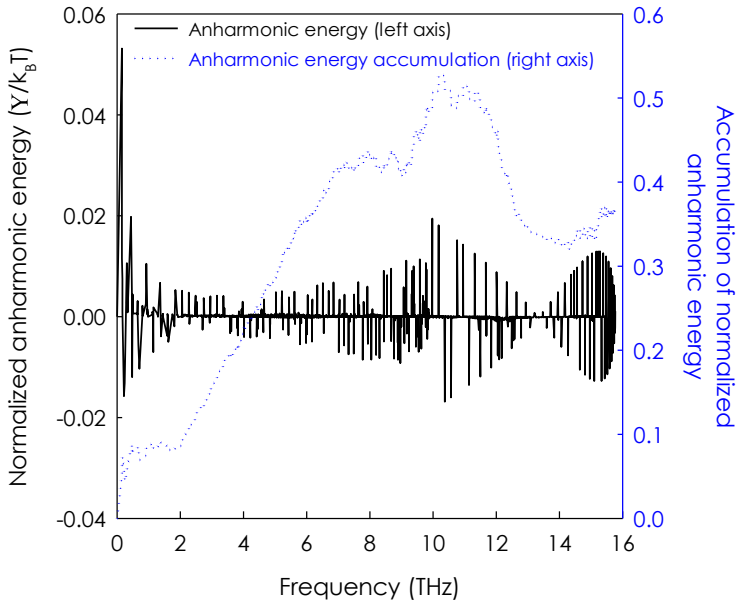

Figure 24 – Mode-level distribution of anharmonic energy, normalized by k_BT, averaged over the first layer of Si atoms at the interface that have Ge atoms as nearest neighbors. This layer is also the most anharmonic region in the structure (see Figure 23). Anharmonic energy accumulation function is also presented in the figure.

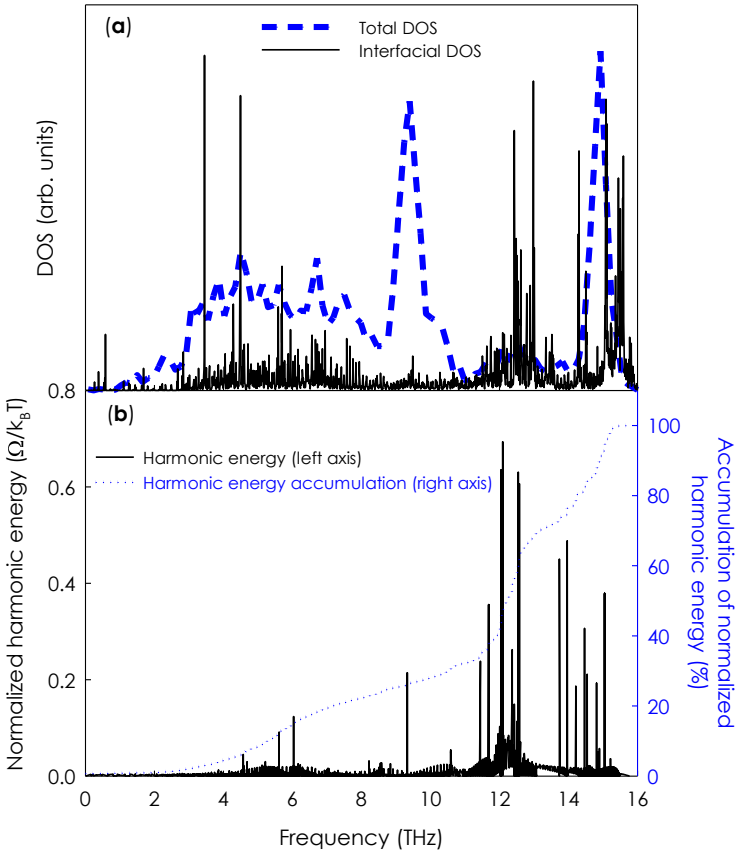

Figure 25 – (a) DOS and (b) Mode-level distribution of harmonic energy, normalized by k_BT, for the last layer of Si atoms at the interface, that has the largest anharmonicity (see Fig. 6) in the Si/Ge structure. Panel (a) also includes the DOS for the entire structure, which is equal to total DOS curve in Figure 18. Spectral energy distribution for the interfacial atoms in panel (a) is determined from the MD simulated atomic velocities [69,121]. The difference between the DOS of the interfacial atoms and the DOS for the entire structure is significant as it appears that the optical phonon peak in Ge between 8-10 THz is shifted to 12-13 THz in the interfacial region.

The scheme provided for calculating the mode-level anharmonic energy contributions from each atom in the system ($\Upsilon_{i,n}$) (Eq. (77)) is a simple and straightforward technique to quantitatively assess the degree of anharmonicity in the interactions in essentially all classes of solid materials.[122] It could be used, for example in crystalline solids or systems with interfaces, defects or even disordered solids. For instance, Figure 23 not only shows that the interface region is the most anharmonic region, but it also shows

that anharmonic energy in the bulk of the Ge side is on average higher than the Si side. This is interesting, because the higher anharmonic energy on the Ge side could be one of the factors that leads to the lower thermal conductivity of Ge compared to Si (*i.e.*, lower relaxation times).[58]

Using the ICMA method, we identified that the high contributions to TIC from modes with frequencies between 12-13THz at the interface of crystalline Si/Ge structures are caused by a small group of interfacial modes that occupy less than 0.1% of the total population of modes. These interfacial modes have extended vibrations on the bulk of Si side and have a strong tendency to couple to virtually all other modes in the system. Our calculations at T=300K show that at the interface ~ 23% of the potential energy is attributable to the anharmonic terms in the potential energy, which leads to strong coupling between modes with different frequencies. However, this relatively large degree of anharmonicity quickly decreases further into the bulk of each side (< 7% anharmonicity in the bulk). Furthermore, this degree of anharmonicity facilitates strong correlations between interfacial modes and virtually all other modes in the structure. By performing energy distribution calculations, we showed that although the interfacial modes are not the most anharmonic modes in the entire structure, but they are the most energetic modes in the most anharmonic region (*e.g.*, the interfacial region). Consequently, all the other modes tend to couple with them to transfer their energy to the other side of the interface. These results therefore provide a basis for developing a new and revised physical picture for thinking about the contributions of localized modes at interfaces.

6.2 Interfaces with disordered materials

It was mentioned previously that in the Landauer description of phonon transport across interfaces (Eq. (11)), v_g needs to be calculated for all the modes of vibration in the system and such a calculation is only possible for crystalline solids. Therefore, application of the PGM based methods to the interfaces of amorphous materials and alloys is highly questionable, since v_g cannot be defined for most of the vibrational modes, as most of the modes of vibration in amorphous materials are not of propagating nature.[42-47] Thus, based on these existing frameworks, there is no obvious insight one can derive from the governing model itself. Instead one can only resort to very approximate physical arguments. ICMA formalism is not dependent on the definition of the PGM and is therefore independent of any description of v_g, thus it has the potential to calculate the modal contributions to the TIC and provide deeper insight into the heat transfer across the amorphous and alloyed interfaces.

With respect to TC, different approaches such as the Allen-Feldman method (A-F) [42,123] or the virtual crystal approximation (VCA) [124] are able to provide some degree of insight into the heat transfer in amorphous solids and alloys, respectively. Using these techniques one can explain the order of magnitude difference between the TC of crystalline and amorphous solids. However, no similar methods exist to predict how TIC varies when one or both sides of an interface is amorphous. The only approximate physical insight one might be able to justify is possibly that an interface with an amorphous material is likely to exhibit low conductance since amorphous material thermal conductivities are typically very low by comparison to crystals. Thus, in essence, the only expectation one might derive

about an interface with an amorphous material is that the modes have short "effective mean free paths" and thus they are unlikely to be effective at moving heat across an interface. Furthermore, one might also argue that if the interface is between an amorphous material and a crystal, the modes in the crystal may have a strong likelihood of scattering at the interface, because the mode character is expected to change dramatically at the interface, thus requiring some type of mode conversion/exchange, which would require a scattering event. However, contrary to this approximate intuition, a recent study [125] measured a larger TIC at the interface of graphite and amorphous SiC than at the interface of graphite and crystalline SiC. The reason for such a non-intuitive result is currently unknown, but likely due to the action of very different mechanisms than what are normally understood to take place in crystalline materials.

On the one hand, in crystalline materials, phonon transport is described based on purely propagating modes of vibration (i.e., the PGM). On the other hand, in amorphous solids transport occurs because of interactions between three distinct types of vibrations: propagons, diffusions, and locons, among which only propagons exhibit a propagating nature.[42] None of the more well-established approaches [42,123,124] are able to explain how these different types of vibrations interact to transfer energy across an interface. For example, the mechanism whereby a propagating mode on the crystalline side couples with a diffuson on the amorphous side can be postulated but has never been studied in detail. In addition, it is unknown whether the localized modes at the interface can facilitate the transfer of energy at a disproportionally higher rate between the two sides in all situations similar to how they behaved at the interface of crystalline Si andGe.[64,122]

6.2.1 Crystalline and amorphous Si/Ge interfaces

To the best of our knowledge, none of the reports that have investigated non-crystalline Si/Ge interfaces have calculated the conductance for an individual interface. In a recent study, Giri *et al.* examined the effect of crystalline/amorphous Si/Ge interfaces on heat transfer through confined films and superlattices.[126] In their study, the reported resistances are the total resistance for the film (*i.e.*, the summation of resistances at the bulk and at the interfaces). In another study Giri *et al.* study the amorphous Si/Ge superlattices and utilize a thermal circuit model (based on separate calculations for bulk resistances) to calculate the resistance at the interfaces.[127] In this study, however we focus on direct calculation of conductance across individual interfaces, which as will be shown can provide additional insights that could not be captured by investigating the thermal transport properties from other approaches. We also extend our investigations beyond the c-Si/c-Ge interface and examine all the various combinations of crystalline and amorphous Si and Ge to evaluate the effects of different phases of solids on interfacial heat transfer.[128] In this regard, six interfaces have been considered: c-Si/c-Ge, c-Si/a-Ge, a-Si/c-Ge, a-Si/a-Ge, c-Si/a-Si, and c-Ge/a-Ge. Table 1 shows how these combinations are chosen, and Figure 26 shows an example supercell used for each of these configurations. In the following, the TIC across these interfaces are calculated and compared and to better understand the contributions by different modes of vibration, the ICMA technique [43,105] is employed.

Table 2 – Six distinct interfaces can be formed by joining the c-Si, c-Ge, a-Si, a-Ge structures: c-Si/c-Ge, c-Si/a-Ge, a-Si/c-Ge, a-Si/a-Ge, c-Si/a-Si, and c-Ge/a-Ge. Only the interfaces on one side of the diagonal are unique.

	c-Si	c-Ge	a-Si	a-Ge
c-Si		*	*	*
c-Ge	*		*	*
a-Si	*	*		*
a-Ge	*	*	*	

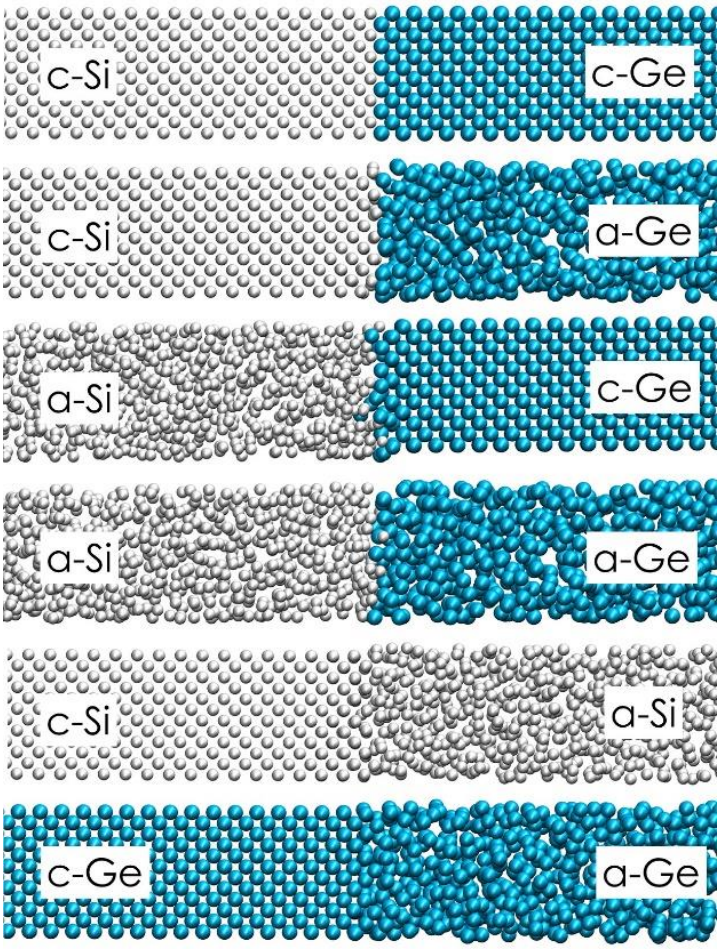

Figure 26 – Schematics of the six formed interfaces between c-Si, a-Si, c-Ge and a-Ge structures. White and cyan spheres represent Si and Ge atoms, respectively.

One of the key benefits of using ICMA is that it can describe any of the modes that exist in an interfacial structure, which can have a variety of different types of mode character. However, because the PGM based descriptions require that all modes be treated as propagating modes, they are unable to account for the effect that an interface has on the mode character in a given structure. Therefore, in this study the ICMA method not only quantifies, but also provides a rigorous and unified platform for understanding the various contributions to TIC from different phonons in all of the Si/Ge systems described in Table 2 and Figure 26.

Here, the ICMA method is first employed in EMD, but is later used in NEMD as well.[105] The Tersoff potential [106] is used to describe the interactions between the atoms in the system. In the case that one side of the interface was crystalline, the number of unit cells along x, y, z directions are 3, 3, and 24, respectively. In previous studies of similar system we showed that the TIC values are converged with less than 5% standard deviation utilizing this system size [43,105,122,129] (see Figure 31 for further discussions). The interface is a plane perpendicular to the z direction, which is parallel to the [100] crystallographic direction. To generate the structure for the amorphous side, the number of atoms corresponding to the densities of a-Si (~2.29 g/cm^3 [130]) and a-Ge (~5.32 g/cm^3 [131]) are initially randomly positioned in a simulation box with the same dimensions as the crystalline side. The system is then heated to a temperature above its melting point, after which it is quenched to 0K over a 50 ns simulation time. The two sides are then brought into contact, and the entire system is annealed at 1000K for 2 ns. This annealing/sintering process is required to ensure the correct positioning of the atoms around their equilibrium sites.[132] Figure 27 shows the radial distribution function (RDF) of the generated amorphous

structures based on this generation scheme. It can be seen that the calculated RDFs show reasonable agreement with experimental values. Periodic boundary conditions are applied in all 3 spatial directions, and a time step of 0.5 fs is used for all simulations. After first relaxing the structures under isobaric-isothermal conditions (NPT) for 1 ns at zero pressure and then at isochoric-isothermal conditions (NVT) for another 1 ns at $T = 300K$, we simulate the structures in the microcanonical (NVE) ensemble for 10 ns at which point the modal contributions to the heat flux across the interface are calculated. The heat flux contributions are saved and post processed to calculate the mode-mode heat flux correlation functions.[105] Statistical uncertainty, due to insufficient phase space averaging, has been reduced to less than 5% by considering 10 independent ensembles for each case.[104,133] All MD simulations were conducted using the LAMMPS package [117] and the eigen modes for each structure were determined from lattice dynamics calculations using the GULP package.[118] It should be noted that zero pressure constraint used in our simulations have also been utilized in other MD studies,[126,127] and it helps to more easily find the finite-temperature relaxed structure and volume. However, because of the lattice-mismatch condition that is common in finite size MD simulations, using such a zero pressure constraint does not ensure zero pressure along all the three Cartesian coordinates, but at least can provide the minimum stress structure. After the relaxation procedure is complete the MD simulations, the authors confirmed that the final densities of the amorphous structures have less than 2% variation from the initial densities mentioned above.

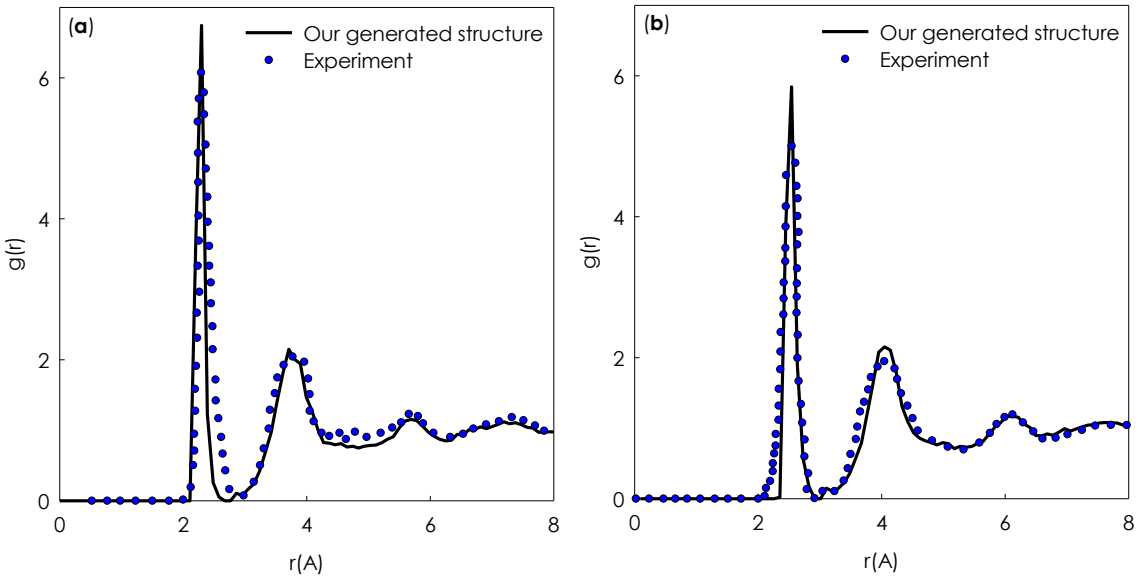

Figure 27 – RDFs for (a) a-Si and (b) a-Ge structures compared to experimental measurements by Alvarez *et al.*[134]

The TIC values for all the interfaces were calculated using EMD at 300K and are presented in Table 3. It can be seen that, except for the c-Ge/a-Ge interface, all of the obtained TIC values differ by less than 40%. This is interesting for two reasons: (1) the TCs of the materials on either side of the interfaces vary greatly – at 300K, the TCs of naturally occurring c-Si (150W/m-K [135-137]) and c-Ge (70W/m-K [138]) are two orders of magnitude larger than a-Si (1 W/m-K [139]) and a-Ge (0.5 W/m-K [140]); (2) the DOS for different modes of vibration across these interfaces are significantly different from each other (see Figure 28). Particularly, the degree of localization to one side of the interface (i.e., the total population of partially extended, isolated and interfacial modes) is ~70% across c-Si/c-Ge interface, while it is only ~25% across c-Si/a-Si interface (see Table 4), yet these interfaces have comparable values of conductance. Although, the overlap in the vibrational density of states has been successful to explain the TIC in many reported instances,[53,67,125-127,141,142] this is not the first time that overlap in the vibrational density of

states has served as a poor descriptor for TIC. In addition to others,[69,87] we also observed similar results for LJ systems.[143] Further investigations are needed to determine what parameters can explain the TIC variations with a better consistency and accuracy compared to density of states overlap.

Table 3 – TIC values for Si/Ge interfaces at 300K ($GWm^{-2}K^{-1}$).

c-Si/c-Ge	0.84
c-Si/a-Ge	0.77
a-Si/c-Ge	0.89
a-Si/a-Ge	1.06
c-Si/a-Si	0.98
c-Ge/a-Ge	0.29

Among the available literature where methods that include anharmonicity are used in calculating the conductance across crystalline/amorphous Si/Ge interfaces, Giri *et al.* have reported the conductance of a-Si/a-Ge interface to be 1.92 $GWm^{-2}K^{-1}$ [127] using NEMD combined with thermal circuit model to decompose bulk and interfacial resistances, which can explain the difference between their value and our reported EMD values. For c-Si/c-Ge interface, using NEMD simulations Giri *et al.* [126] and Landry and McGaughey [70] reported the conductance to be 0.36 $GWm^{-2}K^{-1}$ and 0.34 $GWm^{-2}K^{-1}$ respectively, which are in better agreement with our NEMD calculated conductances (see Figure 33). Additionally, for the c-Si/c-Ge interface, using EMD and Stillinger-Weber interatomic potential,[144] Chalopin *et al.* [94] reported a conductance of 0.63 $GWm^{-2}K^{-1}$, the difference of which from our reported value can be attributed to different interatomic-potentials.

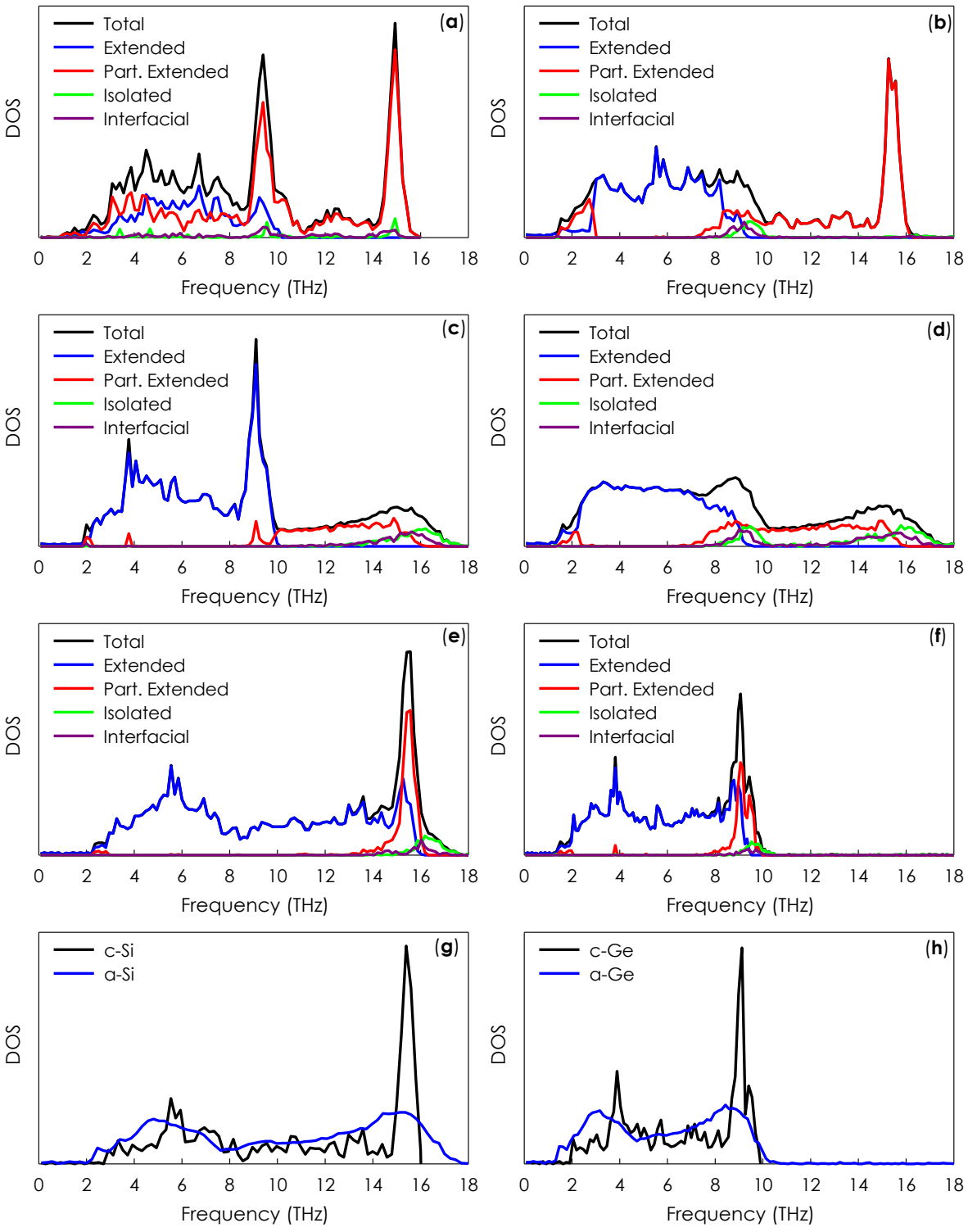

Figure 28 – DOS for the modes of vibration across the (a) c-Si/c-Ge, (b) c-Si/a-Ge, (c) a-Si/c-Ge, (d) a-Si/a-Ge, (e) c-Si/a-Si, and (f) c-Ge/a-Ge interfaces. For comparison, DOS of the bulk crystalline/amorphous Si and crystalline/amorphous Ge structures have also been shown in panels (g) and (h).

Table 4 – Number of states for the four different classes of vibration and their contribution to TIC across the c-Si/c-Ge, c-Si/a-Ge, a-Si/c-Ge, a-Si/a-Ge, c-Si/a-Si, and c-Ge/a-Ge interfaces. Columns 2-4 describe the fraction of the total number of states ($\overline{DOS}$), the percentage contribution to G ($\overline{G}$), and contribution to G divided by fraction of total number of states (i.e., contribution to G per mode) ($\overline{G}/\overline{DOS}$), respectively. In agreement with our previous observations,[43,122,129] interfacial modes in all of the structures have the highest per mode contribution to the TIC. The TIC value for each interface from Table 3 is also included for ease of comparison.

	c-Si/c-Ge $\left(G = 0.84 GWm^{-2}K^{-1}\right)$		
Mode	$\overline{DoS}(\%)$	$\overline{G}(\%)$	$\overline{G}/\overline{DOS}$
Extended	29.35	51.99	1.77
Partially	64.24	29.28	0.45
Isolated	3.50	<	< 0.01
Interfacia	2.90	18.73	6.45

	c-Si/a-Ge $\left(G = 0.77 GWm^{-2}K^{-1}\right)$		
Mode	$\overline{DoS}(\%)$	$\overline{G}(\%)$	$\overline{G}/\overline{DOS}$
Extended	51.27	52.22	1.02
Partially	43.11	40.25	0.93
Isolated	3.21	<	< 0.01
Interfacia	2.39	7.53	3.15

	a-Si/c-Ge $\left(G = 0.89 GWm^{-2}K^{-1}\right)$		
Mode	$\overline{DoS}(\%)$	$\overline{G}(\%)$	$\overline{G}/\overline{DOS}$
Extended	69.16	62.26	0.90
Partially	19.19	25.72	1.34
Isolated	6.62	< 0.01	< 0.01
Interfacia	5.01	12.02	2.40

	a-Si/a-Ge $\left(G = 1.06 GWm^{-2}K^{-1}\right)$		
Mode	$\overline{DoS}(\%)$	$\overline{G}(\%)$	$\overline{G}/\overline{DOS}$
Extended	56.23	54.71	0.97
Partially	24.36	25.99	1.07
Isolated	11.24	<	< 0.01
Interfacia	8.16	19.30	2.33

	c-Si/a-Si $\left(G = 0.98 GWm^{-2}K^{-1}\right)$		
Mode	$\overline{DoS}(\%)$	$\overline{G}(\%)$	$\overline{G}/\overline{DOS}$
Extended	77.73	83.61	1.08
Partially	16.20	7.70	0.48
Isolated	4.00	<	< 0.01
Interfacia	2.05	8.69	4.24

	c-Ge/a-Ge $\left(G = 0.29 GWm^{-2}K^{-1}\right)$		
Mode	$\overline{DoS}(\%)$	$\overline{G}(\%)$	$\overline{G}/\overline{DOS}$
Extended	79.93	85.75	1.07
Partially	15.30	7.94	0.52
Isolated	3.36	<	< 0.01
Interfacia	1.38	6.31	4.57

The TIC accumulation functions for each of the six configurations were calculated and are shown in Figure 29. In addition, by using ICMA, the degree of coupling/interaction between each pair of vibrational modes across the interface [43] was calculated and is presented as 2D maps of correlation in Figure 30. As was pointed out in the previous section, for the c-Si/c-Ge interface, the modes of vibration in the frequency range of 12-13THz show a large degree of coupling with all the other modes of vibration in the system (Figure 30a) and contribute almost 15% to the TIC (Figure 29) [122]. The population of these modes in this 12-13THz region was shown to be less than 0.1% of the total population of modes.[122] Additionally, it was shown that while these modes have extended vibrations on the Si side, they also exhibit a large portion of their vibrational energy at the interface [122] – hence they are considered interfacial modes of vibration [43] (see Figure 20 for a representation of these modes of vibration). By changing the crystallinity of each side of the interface, the highly interacting frequency region of 12-13THz (Figure 30a) seems to shift to a broader frequency region of vibrations around 10-14THz for c-Si/a-Ge, a-Si/c-Ge and a-Si/a-Ge interfaces (Figure 30b-d). Although the frequency region of 10-14THz

also contributes largely to the TIC across c-Si/a-Ge, a-Si/c-Ge and a-Si/a-Ge interfaces (see Figure 29), all the modes of vibration present within this region contribute on average equally to the TIC. Therefore, unlike the c-Si/c-Ge interface, contributions to interfacial heat transfer across the c-Si/a-Ge, a-Si/c-Ge and a-Si/a-Ge interfaces are not dominated by small subset of modes. It is also interesting to note that the highly interacting frequency region of 12-13THz in the c-Si/c-Ge interface is absent in the c-Si/a-Si and c-Ge/a-Ge interfaces (Figure 30e-f). In fact, the TIC for these interfaces is largely dependent on the elastic interactions (i.e., auto-correlations) present along the diagonal of the 2D maps of correlation (Figure 30e-f), which can possibly be attributed to the large population of extended modes in the c-Si/a-Si and c-Ge/a-Ge structures (in which more than 75% of the modes are extended) (see Table 4). Extended modes are delocalized; thus they potentially can transfer heat to the other side of the interface without the need to couple to other modes of vibration.[43] Although c-Si/a-Si and c-Ge/a-Ge interfaces seemingly follow similar mechanisms of interfacial heat transfer (see Figure 28e-f, Table 4 and Figure 30e-f), the conductance across c-Ge/a-Ge interface is 3.38 times smaller than c-Si/a-Si interface. Such a lower conductance for c-Ge/a-Ge interface can be understood by considering the fact that the absolute of values of heat flux across this interface are on average smaller than the ones across the c-Si/a-Si interface. In fact, in our simulations, the average of the absolute values of heat flux at the c-Si/a-Si interface was 2.36 times larger than that of the c-Ge/a-Ge interface. These lower values of interfacial heat flux naturally result in lower values of conductance using both equilibrium and non-equilibrium definition of interface conductance for the c-Ge/a-Ge interface and they arise due to the simple fact that Ge is heavier than Si. Thus, at the same temperature Ge atoms have lower velocities than Si, and

since the heat flux itself is directly proportional to the atom velocities on both sides, the low velocities for both a-Ge and c-Ge yield lower overall heat fluxes and conductances.

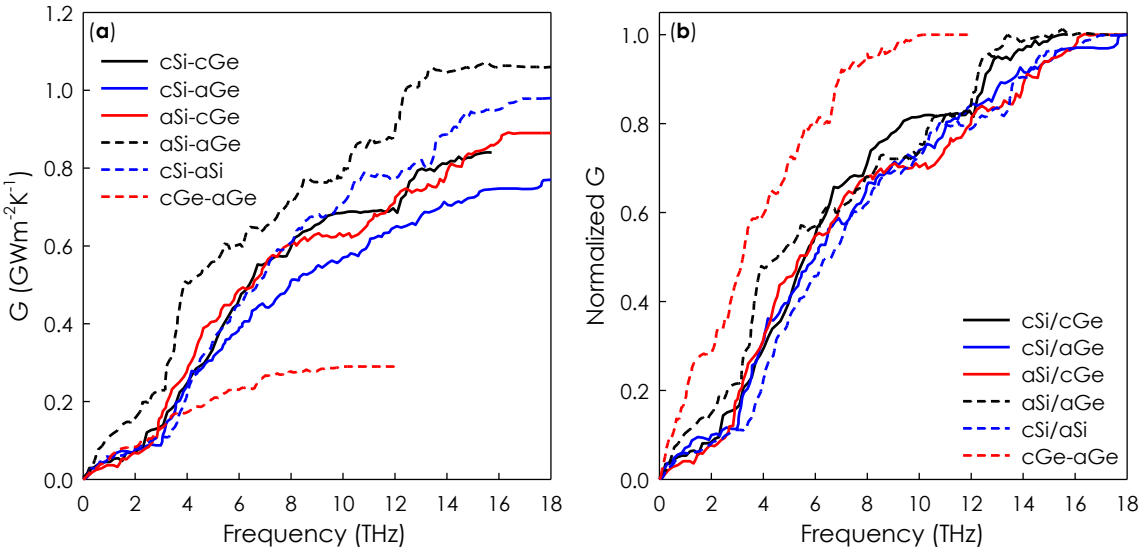

Figure 29 – (a) Non-normalized and (b) normalized TIC accumulation functions for Si/Ge interfaces at T=300K.

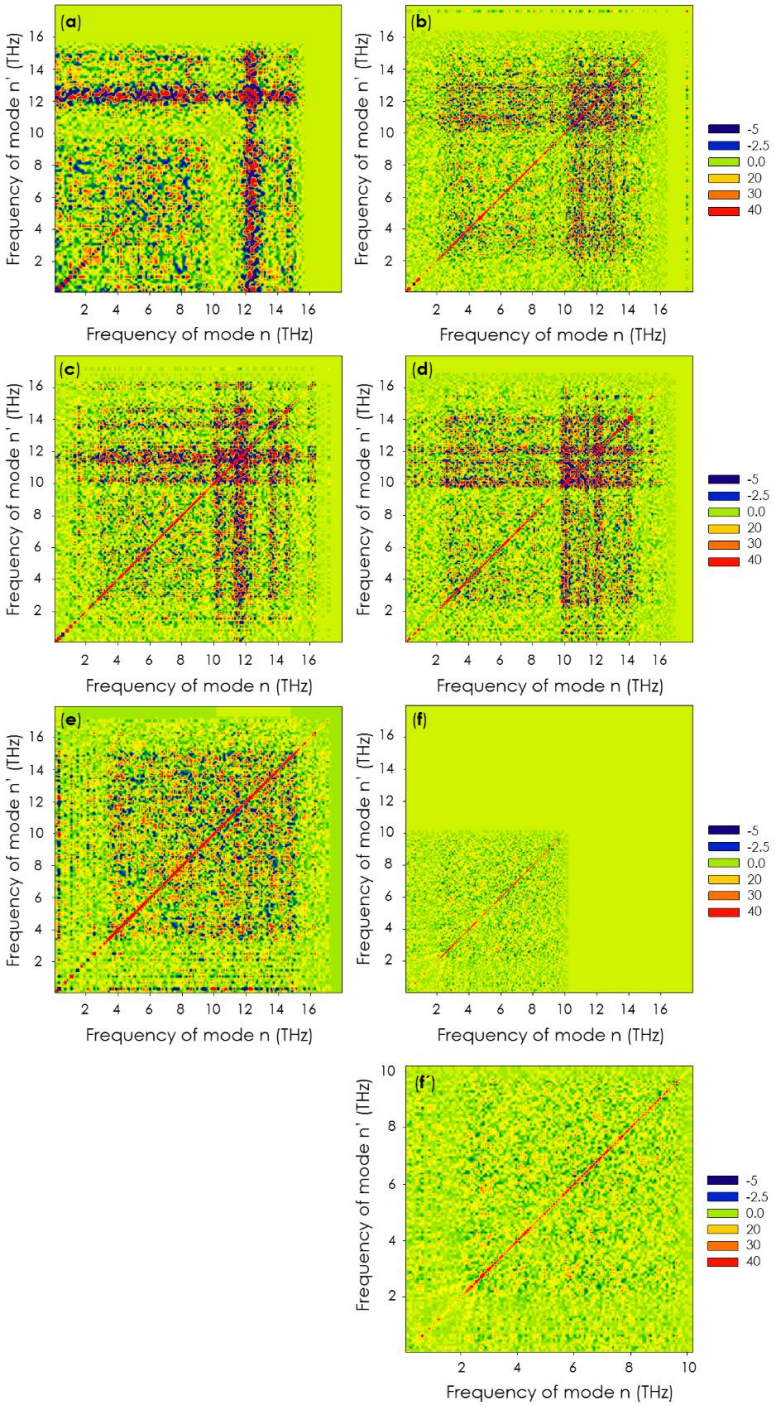

Figure 30 – 2D maps showing the magnitude of correlations/interactions across the (a) c-Si/c-Ge, (b) c-Si/a-Ge, (c) a-Si/c-Ge, (d) a-Si/a-Ge, (e) c-Si/a-Si, and (f) c-Ge/a-Ge interfaces as elevations above the plane of two frequency axes. (f´) shows a magnified view for the interactions across the c-Ge/a-Ge interface (panel (f)). The values presented on the maps have units of $MWm^{-2}K^{-1}$.

6.2.1.1 Understanding size effects in NEMD simulations.

As was shown in Figure 28 and Figure 29, the c-Si/c-Ge case is heavily dependent on the interfacial modes present in the 12-13THz frequency region. Using ICMA formalism, we also know that these interfacial modes have a long tail of vibration on the bulk Si side. Since a substantial portion of their vibration extends through the Si side, we postulated that if one were to perform NEMD simulations of this structure, the heat baths might actually perturb these modes. Particularly because the TIC depends so strongly on the presence of these interfacial modes, the unnatural perturbations associated with velocity rescaling in the heat baths can hypothetically affect the TIC across c-Si/c-Ge. Such an effect is interesting because it cannot be described by a scattering based paradigm. In theory, if TIC is truly governed by phonon scattering at the interface, then scattering away from the interface should not affect it.

It should be noted that based on the Landauer formalism (Eq. (11)) there should be no size dependence associated with TIC. No length dependent properties, such as mean free path, enter the Landauer description. The only length dependent property is the number of modes in Eq. (11), which are the allowed modes of vibration in the system.[33] Regarding this issue, Figure 31 shows that our conducted EMD simulations are effectively size-independent, which is in agreement with other reports on Si/Ge interfaces.[94] Therefore, it seems that even a small structure with ~3x3x24 unit cells on each side of the interface includes sufficient number of modes that TIC varies by less than 5%. (See Figure 31). Therefore, according to the standard picture, for system sizes beyond 3x3x24, there should not be any size dependence for the TIC. However, in concept, when one performs velocity rescaling during NEMD simulations, one effectively disrupts mode amplitudes artificially,

which can hinder a mode's ability to naturally couple to other modes of vibration and transfer energy. Thus, even though the scattering picture may be useful in many contexts, the existence of an effect on TIC by perturbing modes far away from the interface would serve as evidence to support the notion that the true picture is instead one of correlation/coupling between modes, and not scattering. However, this effect might be reduced for larger and larger structures as the perturbations (*e.g.*, the region of heat input) are moved farther from the interface. Nonetheless, it is also possible that the effect may never completely vanish, since these modes penetrate through the body of the silicon portion (Figure 20). If true, this would be the first report of such a size effect and would be quite notable, since it would strongly confirm the concept that the interfacial modes exist and can be affected by perturbative stimuli far away from the interface.

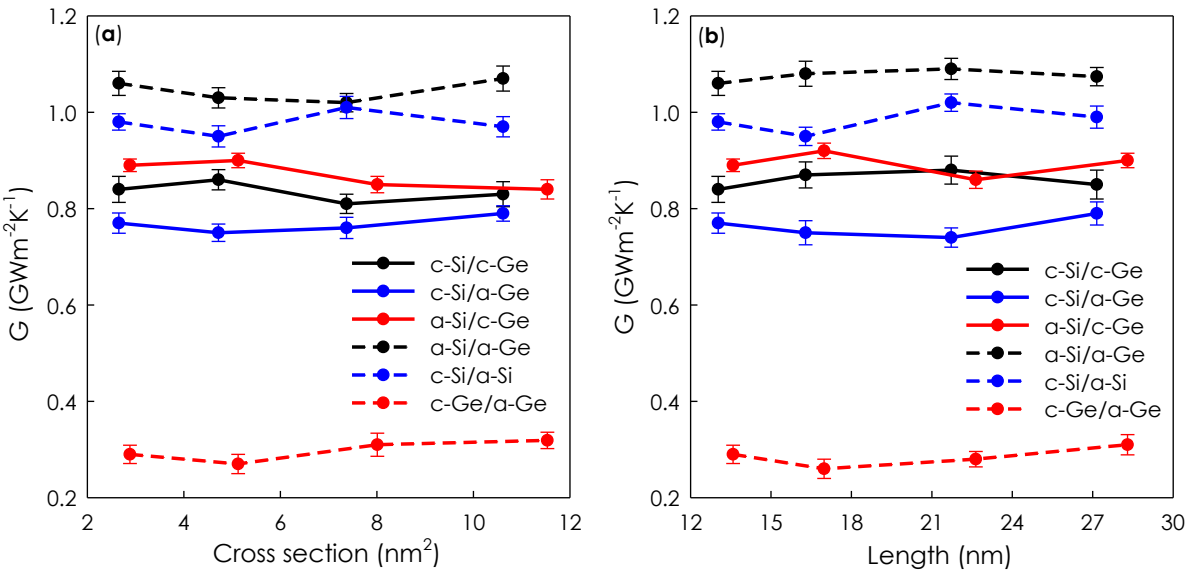

Figure 31 – The effects of increasing the (a) cross section and (b) length of the structure on the TIC of different Si/Ge interfaces from EMD simulations.

To investigate this potential phenomenon, we conducted NEMD simulations using periodic boundary conditions in all Cartesian directions. The cross sections of the structures

in the NEMD simulations are of equal dimensions as the supercells used in the EMD simulations. Hot and cold heat baths were placed at midpoints between the (periodic) interface (Figure 32). A thermal power equal to 220 nW is input to the system at the hot bath and removed from the system at the cold bath. The system is simulated for 4 ns to reach steady state, after which the temperature profile (see Figure 32) remains constant throughout the structure. The temperature profile was then averaged for 2 ns, from which the temperature jump (ΔT_K) at the interface was calculated across the interface. The TIC at the interface can then be calculated from,

$$G = \frac{\overline{Q}}{\Delta T_K} \tag{78}$$

where $\overline{Q}$ is the time-averaged heat flux through the interface. Five independent ensembles were simulated for improved phase-space averaging.

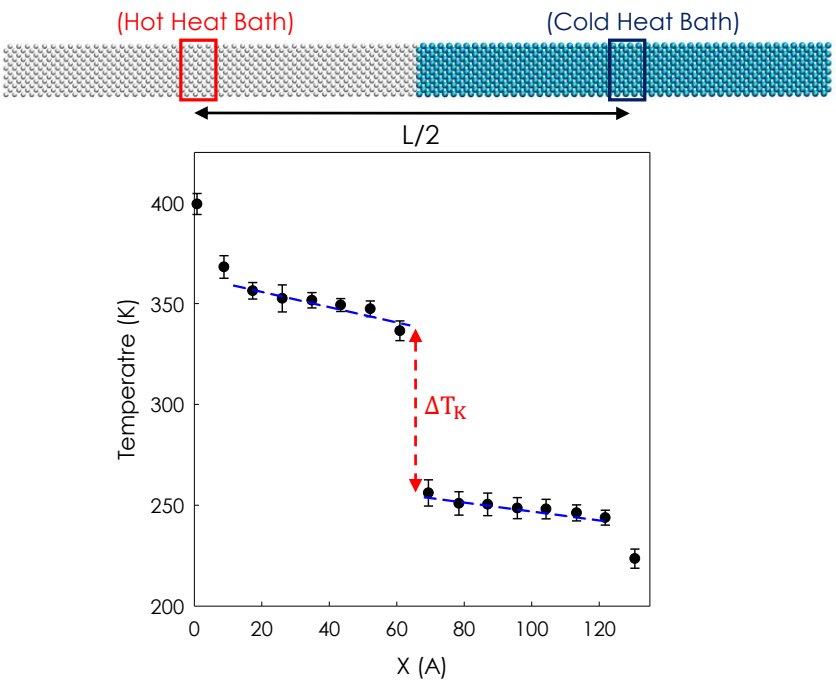

Figure 32 – Schematic of the NEMD implementation to calculate TIC. Hot and cold heat baths are assigned by red and blue blocks, respectively. White and cyan spheres represent Si and Ge atoms, respectively. Temperature distribution is also provided, which clearly shows the temperature drop (Kapitza resistance) around the interface.

The results are presented in Figure 33 and confirm the hypothesis that size effects can have a significant impact on TIC. All the NEMD calculated TIC values except for the a-Si/a-Ge interface were found to be significantly lower than the values calculated from EMD. Since the EMD values are independent of the system size (see Figure 31), for a clearer comparison with NEMD values, they are shown normalized to the corresponding EMD value for the same structure. The large difference between the EMD and NEMD values for conductance across the a-Si/a-Ge interface is surprising. One reason for such discrepancy can be attributed to the fact that due to the low thermal conductivities of amorphous structures no clear temperature drop could be detected across the a-Si/a-Ge interface. This can be the reason this interface appears to have a higher TIC than the equilibrium value, as the uncertainty associated with the calculation is larger. In this regard,

as was pointed out in a recent study by Giri *et al.* [126] EMD calculations can provide better predictions for TIC across such interfaces. It may also be possible that the mechanism for transport between diffusons and locons is enhanced by the heat bath perturbation while it is suppressed for propagating modes existing in a crystalline material. Further study would be needed to determine if this is true, but it if so this study would provide some supporting evidence to that effect. In addition, Figure 33 shows that the NEMD TIC values for the c-Si/c-Ge interface exhibit the largest discrepancy with the EMD values and exhibit the strongest size dependence. Perturbing the vibrations by placing the heat baths at the bulk of the materials, even far from the interface (*e.g.*, > 60 nm), can have a noticeable effect on TIC, even for a system with a length > 60 nm. This observation cannot be understood through the standard PGM/Landauer formalism, since it would be difficult to rationalize how perturbing a mode far from the interface would affect its transmissivity at the interface. Landry and McGaughey [70] have shown that by simulating longer structures (*e.g.*, >150nm) convergence for conductance across c-Si/c-Ge interface using NEMD approach can be achieved. They also observed convergence between their NEMD calculations and a Landauer-based approach for interface analysis and observed good agreement.

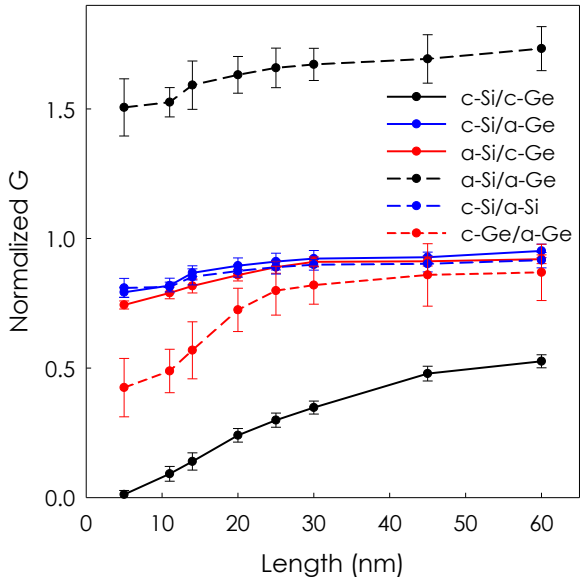

Figure 33 – Normalized TIC values for Si/Ge interfaces obtained from NEMD simulations as a function of the system length. The NEMD values are normalized to the corresponding EMD value for the same structure.

To further confirm that this effect is in fact caused by the aforementioned mechanism, we computed the conductance accumulations using the NEMD implementation of ICMA.[105] The TIC accumulation function from this approach is calculated and presented in Figure 34, which shows that in the NEMD simulation, the ability of interfacial modes to couple to other modes is hampered by the heat bath. Here it is interesting to see that it is primarily the contributions of other modes that would have coupled to the 12-13 THz interfacial modes that is mostly affected. Thus, the observations indicate that mode-mode correlation/coupling in the bulk of a material may be a core mechanism for interfacial heat transfer, as was also suggested by Wu and Luo.[86] This is particularly interesting because it suggests a rather different physical picture is needed as compared to the standard PGM/Landauer model. Having observed this effect, to further test our understanding, we constructed an alternative system by separating the heat baths

by 2 additional layers of c-Si and c-Ge, effectively simulating three periods of a superlattice structure (Figure 35). If our understanding of the effect of the heat baths is correct, then for this larger structure, we would expect markedly reduced effect from heat baths on the middle interface, which does not contain materials in contact that are directly perturbed by the heat baths. In this way, the heat bath effect should be most pronounced for the other two interfaces, but possibly negligible for the middle interface.

Such a test is again a potentially strong indicator that the scattering based interpretation of interfacial heat flow may be problematic, even in the case of two crystals, where the PGM is most well justified. This is because the three periods of the superlattice structure are identical, thus one would expect by all scattering based arguments they should all exhibit the same TIC. This perspective is based on the fact that the most prevalent picture for interfacial transport is based on the PGM/Landauer formalism, which in no way suggests that transmission at an interface should in any way be coupled to or affected by scattering away from the interface. In the current view the bulk and interface scattering are viewed as essentially independent phenomena, and thus the effect that heat bath would have 10's of nanometers away from the interface should be negligible, thereby leading to the same TIC for all three superlattice period interfaces.

The results of this test are shown in Figure 35, which confirms our hypothesis by showing that the unperturbed interface in the middle has a higher TIC, as visibly evidenced by the noticeably larger temperature drop at the other interfaces (Figure 35). This result is quite remarkable because the NEMD version of the ICMA formalism does not even involve the calculation of correlation functions. Instead, it is proportional to each mode's average heat flux, and thus it is quite interesting to see that the average mode heat flux itself is

actually affected by the heat baths. This then strongly suggests that a coupling/correlation based perspective is actually in more correct alignment with the actual transport that happens at interfaces, rather than a scattering based perspective. Furthermore, this result also suggests that one may be able to affect transport at a faraway interface, by modifying or perturbing modes artificially in another part of the system. To our knowledge this is the first report of such an observation, and it can provide a new pathway to dynamic control or influence over TIC, by indirect means in certain material systems, which is quite non-intuitive based on the prevalent PGM paradigm.

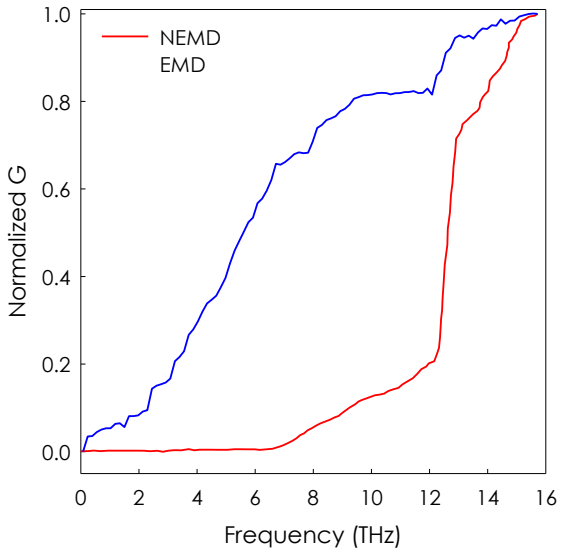

Figure 34 – Modal contributions to TIC for the c-Si/c-Ge interface calculated from the NEMD and EMD implementations of ICMA.

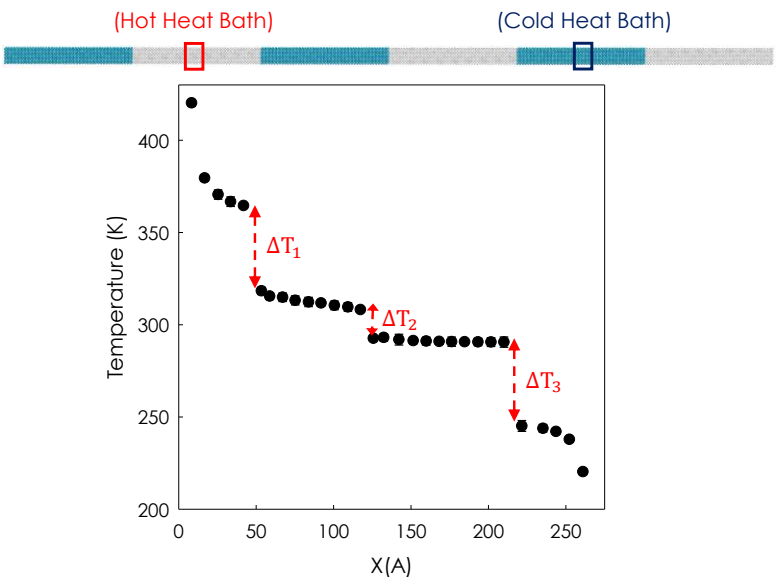

Figure 35 – Schematic of the NEMD implementation across the superlattice structure. Hot and cold heat baths are assigned by red and blue blocks respectively. White and cyan spheres represent Si and Ge atoms, respectively. Temperature distribution is also provided, which clearly shows that the temperature drop across the interface with unperturbed vibrations (ΔT_2) is smaller than the drop across the interfaces with perturbed vibrations (ΔT_1 and ΔT_3).

6.2.2 InP/InGaAs interface

Indium-gallium-arsenide alloys ($In_xGa_{1-x}As$) are of significant interest for thermophotovoltaics (TPV) [145,146] and other electronic systems.[147,148] In many instances there is specific interest in the $In_{0.53}Ga_{0.47}As$ alloy, because it is lattice matched with InP [149], which is commercially available as a single crystal substrate. This lattice matching makes this system an ideal platform for growing high quality single crystal devices, since there is minimal strain to drive the formation of defects, which can negatively affect the device performance.[150] Furthermore, since $In_{0.53}Ga_{0.47}As$ has an electronic band gap of 0.74 eV, it is an ideal candidate for TPV, since this band gap is close to the peak in the Black body spectrum at temperatures commensurate with many high temperature heat sources.

In many applications the devices consist of many successive layers with thicknesses ranging from as low as 10 nm up to 10 micron, and the temperature of the devices can often have a major influence on the performance. These devices therefore have to consider thermal management issues and one important quantity can be the thermal interface conductance (TIC) between the two materials.

Depending upon the device, low values of TIC could be highly important, if it presents a significant resistance to heat flow out of the system. In this study we used the ICMA method to not only quantify, but understand the various contributions to TIC from different phonons in the $In_{0.53}Ga_{0.47}As$/InP system.

We used ICMA and equilibrium MD to calculate the modal contributions to TIC. The interactions are described by Tersoff interatomic potential [106] based on the parameters by Powell *et al.* [151] to model different III-V semiconductor compounds, and we used mixing rules [106] to describe the cross species interactions. Periodic boundary conditions have been applied to all three Cartesian coordinates, and a time step of 0.5 fs is chosen for the MD simulations. The number of unit cells along the xyz directions have been chosen to be equal to 3, 3 and 24 (3x3x24). We examined the effect of larger cross sections up to 5-5 unit cells and longer systems up to 50 unit cells, and neither resulted in changes larger than 5% to both the mode distributions from LD or modal contributions to TIC calculated from MD. The interface is situated normal to the z direction, which is parallel to the [100] crystallographic direction, and the simulation temperature was set equal to 300K. After relaxing the structure under the isobaric-isothermal ensemble (NPT) for 1 ns at zero pressure and $T = 300K$ and under the canonical ensemble (NVT) for another 1 ns at $T = 300K$, we simulated the structure in the microcanonical (NVE) ensemble for 10 ns

during which the modal contributions to the heat flux across the interface are calculated. The heat flux contributions are saved and post processed to calculate the mode-mode heat flux correlation functions.[105] The effect of different configurations on the InGaAs side has been accounted for by averaging the results over five different random alloy configurations. Statistical uncertainty, due to insufficient phase space averaging, has been reduced to less than 5% by considering 10 independent ensembles.[104] The MD simulations were performed using the LAMMPS [117] and the LD calculations were performed using the GULP package [118]. The low-temperature LD information used in this study is justified because the simulation temperature of 300K is lower than the temperatures (e.g., 800K) at which Feng *et al.* [152] and Gill-Comeau and Lewis [153] have reported noticeable changes in frequencies and eigen vectors for their modal analysis. This effect is also not expected to dramatically change the results for this system.

Similar to previous studies, we observed four different types of modes arising from the LD of the entire structure of InGaAs/InP interface. Interestingly, unlike previous systems,[43,122] these modes are actually segregated into well-defined regions based on their frequencies. Figure 36b shows the total DOS and DOS for each type of vibration at the interface of InGaAs/InP. In addition, the eigen vectors of vibration for a sample eigen mode of vibration belonging to each class of vibration are provided in Figure 37. The segregation of the modes according to their frequencies is different from previous observations of Ar based interfaces,[43,143] Si interfaces with mass difference,[43] or Si/Ge interfaces [122] in which different types of vibrational modes appear in overlapping regions of the DOS. It is also peculiar that even the partially extended modes on InP side and partially extended modes on InGaAs side occupy separate sections on DOS. The primary cause of the mode

segregation is the phonon band gap in InP. InP has a large gap in its vibrations between ~5.9-10 THz (see Figure 36a), largely due to the significant mass difference in the basis (~ 3.5X). The lack of vibrational states between 5.9-10 THz in InP forces the system to segregate the modes of the full structure into distinct regimes.

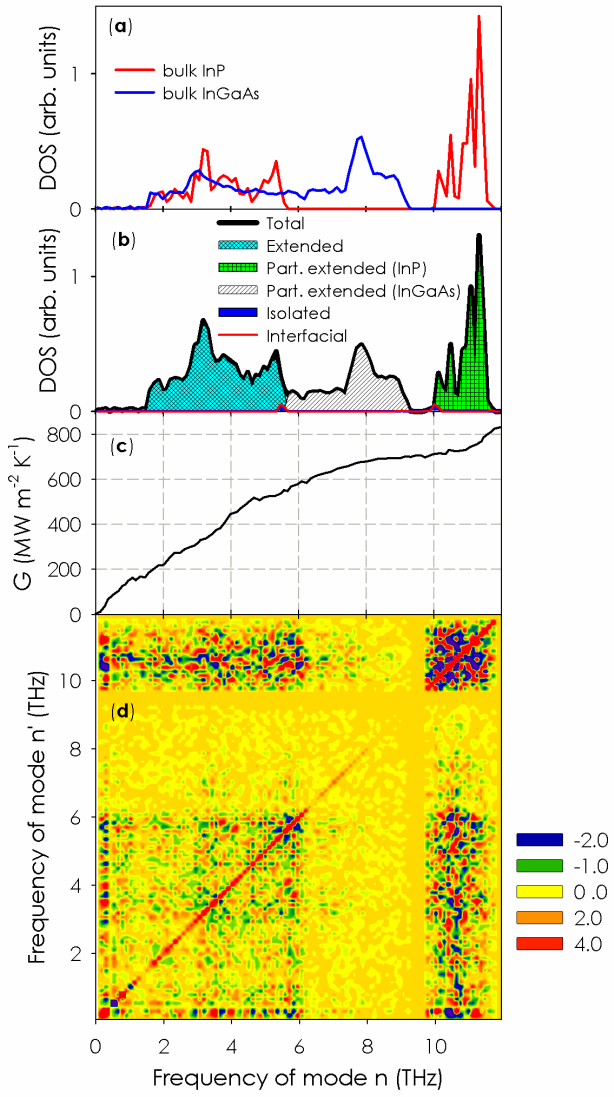

Figure 36 – DOS and modal contributions to TIC for InGaAs/InP interface at T=300K. (a) DOS for isolated InP and isolated InGaAs before making interface, (b) total DOS and DOS for different mode classifications across the interface, (c) TIC accumulation function, and (d) 2D map showing the magnitudes of the correlations/interactions on the plane of two frequency axes. The values presented on the 2D map have units of $MWm^{-2}K^{-1}$ **.**

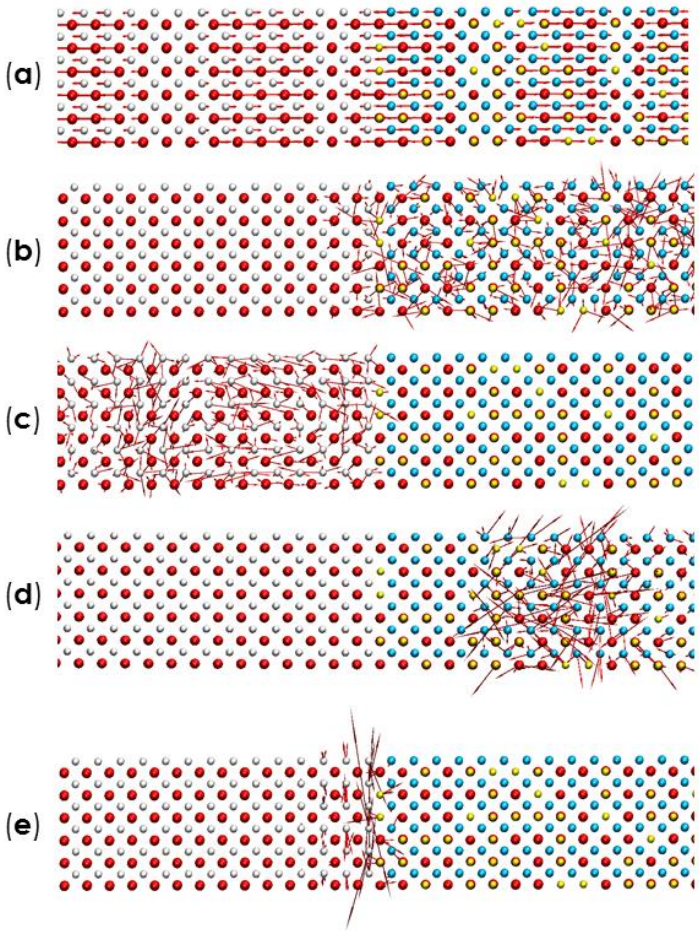

Figure 37 – Eigen vectors for different examples of the four classes of vibration present at the interface of InGaAs/InP. In, Ga, As, and P atoms are represented by red, yellow, cyan, and white spheres respectively. The examples and their frequencies are (a) extended mode at 3.86THz, (b) partially extended mode centered on InGaAs side at 8.11THz, (c) partially extended mode centered on InP side at 10.61THz, (d) isolated mode at 5.48THz, and (e) interfacial mode at 9.96THz.

Table 5 – Number of states for the four different classes of vibration and their contribution to TIC across the InGaAs/InP interface. Columns 2-4 represent the fraction of the total number of states ($\overline{DOS}$), the percentage contribution to G ($\overline{G}$), and contribution to G divided by fraction of total number of states (i.e., contribution to G per mode) ($\overline{G}/\overline{DOS}$), respectively.

Mode Type	$\overline{DOS}$(%)	$\overline{G}$(%)	$\overline{G}/\overline{DOS}$
Extended	47.1	70.6	1.50
Partially extended	52.6	23.1	0.44
Isolated	0.1	< 0.01	< 0.01
Interfacial	0.2	6.3	31.5

From Figure 36a, it can be seen that the interfacial modes exist at two narrow bands of frequencies: (1) the point where extended modes transition into partially extended modes on InGaAs side, and (2) the onset of partially extended modes on InP side. Also, interestingly Table 5 shows that, by comparison to previously studied structures, the $In_{0.53}Ga_{0.47}As$/InP structure has significantly more extended modes ~ 47%, which is larger than a previously studied Ar/4Ar interface ~10% [43] and Si/Ge interface ~30%.[122] In essence, since extended modes correspond to collective vibrations of the entire system (*e.g.*, including both bulk materials together) at a single frequency, their fraction of the total number of states is commensurate with the bulk DOS overlap. However, previously we showed that for instance at the interface of Ar(m)/Ar(4m) a large population of partially extended modes exist even at the region of frequency overlap between the two sides of the interface.[43] This observation showed that DoS overlap does not automatically guarantee that the states will be extended. Nonetheless, for the $In_{0.53}Ga_{0.47}As$/InP structure,

interestingly all of the eigen modes in the regions of DoS overlap fall into class <1> and are extended. Thus, the $In_{0.53}Ga_{0.47}As$/InP structure appears to have the maximum number of extended modes possible.

After calculating the modal contributions to TIC it was found that again, the interfacial modes have the highest per mode contribution (see Table 5), similar to Ar/4Ar [43] and Si/Ge interfaces.[122] Figure 36c shows that the conductance accumulation associated with the low frequency modes (e.g., between 0 and 1THz) is large, ~20% of the total TIC. The large value observed for the total TIC also suggests that in InGaAs/InP devices, this particular interface likely contributes negligible resistance to the overall device resistance.

Using ICMA, the degree of interaction/correlation between each pair of vibrational modes in the system can be calculated and presented as a two-dimensional map of correlation,[43,105] shown in Figure 36d. Since elastic interactions are restricted to phonons of the same frequency, which are only associated with the values along the diagonal of the correlation map (Figure 36d), all the off-diagonal contributions are attributed to the anharmonicity. It is interesting to note that the large contribution by extended modes (~70%) including the contribution by low frequency modes between 0-1THz mainly arises from the auto-correlations, while for partially extended modes, particularly the ones that are located on the InP side, the major contributions to TIC are caused by cross-correlations. In fact, since the frequency of vibration for the partially extended modes on InP side is larger than the maximum frequency of vibration on InGaAs side, the contribution by these modes are attributed to anharmonicity. Particularly, it can be seen from 2D correlation map that partially extended modes on InP side are primarily correlated with lower frequency extended modes in the system. Moreover, not only because of their considerable

contribution to conductance (~12%), but also because of their strong band of anharmonic coupling, the contributions by partially extended modes on the InP side, to a great degree, resemble the contributions by interfacial modes in crystalline Si/Ge interfaces.[122] In addition, the degree of cross-correlations for partially extended modes primarily located on InP side seem much stronger compared to the cross-correlations for partially extended modes primarily located in InGaAs. It can also be seen from Figure 36d that the frequency-doubling and frequency-halving processes that was reported to be significant for Ar(m)/Ar(4m) interface [154] do not seem to be the dominant correlations for the interface of InP/InGaAs.

These observations lead to the following interpretations (1) The extended modes behave almost as their own subsystem and exhibit minimal interaction with other modes in the system. Since they extend through the entire structure, it is as if they do not recognize the presence of the interface and thus, their contributions may not be well explained by a picture framed upon the PGM, *e.g.*, it is as if they simply contribute directly to the total thermal conductivity of the full structure based on their respective mean free paths. (2) The fact that the partially extended mode contributions are dominated by their cross-correlations suggests that these mode's contributions may be well described by the PGM transmission paradigm. This is because cross-correlation is a signal of interaction and therefore these modes, which on the InP side are essentially propagating modes, carry energy to the interface and then exchange it with other modes on the other side via scattering. (3) The fact that the high frequency modes, above the phonon band gap in InP, contribute primarily via cross correlation is consistent with the conventional PGM model, since there are no modes on with the same frequencies on the other side that they can

exchange energy with. Therefore, all of their contributions can be associated with inelastic interactions/anharmonic effects. Furthermore, the fact that their contributions are non-negligible ~ 12%, suggests that, again, as was observed for other systems [16,56,64,65,154] anharmonicity is non-negligible at room temperature.

After studying this interface, we have noted first that that remarkably, the normal modes of vibration segregate into distinct regions of frequency. Secondly the TIC is very high and is not likely to be limiting in devices with layer thicknesses greater than ~15 nm. The majority of the TIC comes from the extended modes and various correlations for each group of modes indicates that the extended modes behave as if the interface is non-existent, while the partially extended modes behave in a manner more consistent with the conventional paradigm based on the PGM. This application of the ICMA method provides insight and useful data for future studies focused on thermal management in systems containing InGaAs/InP interfaces, as there is now evidence to suggest that the TIC is large and may be negligible by comparison to the thermal resistance of the respective device layers.

CHAPTER 7. CONCLUSIONS AND FUTURE DIRECTIONS

7.1 Conclusions

PGM has been the dominant method of choice for studying heat transfer across interfaces for almost a century. However, using PGM based approaches, the predicted conductance values show large deviations from experimental measurements. In addition, none of the PGM based techniques has been successful in fully including the important effect of anharmonicity in the calculations. Furthermore, by being based on Landauer formalism, PGM based approaches can only be applied to the interfaces between pure crystalline materials. In this thesis, we devised the ICMA formalism to calculate the anharmonic modal contributions to interfacial heat transfer. Unlike all the other existing methods, our model is not based on the PGM, therefore it does not suffer from the limitations of Landauer formalism. In fact, since ICMA is fundamentally based on the fluctuation-dissipation theorem, the physical intuition that it offers for interfacial heat transfer follows a correlation approach, which is different from the scattering approach that the PGM offers. The following are the important features of ICMA:

- Using ICMA, for the first time, the exact eigen vectors of vibration around the interface could be calculated. In fact, some of these vibrational modes are localized and non-propagating, which is very different in nature than the modes of vibration that PGM based approaches are based on.
- By not being based on any limiting assumptions, ICMA can be applied to interfaces between all phases of solids (*i.e.*, crystalline, amorphous, alloyed,

etc.). All the other existing techniques can only be applied to the interfaces between pure crystalline solids.

- Using ICMA, for the first time, the exact anharmonic contributions by an individual mode of vibration to the interface conductance could be calculated. In this sense, the resolution provided by ICMA is even higher than techniques that can calculate the contributions for different frequencies of vibration (*i.e.*, spectral techniques [64,66,154]).
- By being based on MD simulations, ICMA includes anharmonicity to its fullest order in the calculations; this could not be achieved using any of the previously exiting techniques.
- ICMA allows for inclusion of the desired atomic positions around the interface in the calculations. For instance, ICMA can calculate the anharmonic modal contributions for both smooth and rough interfaces. This is a crucial improvement, since most of the actual interfaces are not smooth/perfect and contain various forms of defects such as dislocations, vacancies, and interdiffusions, and by having the ability to exactly describe the atomic positions, ICMA can systematically quantify the effect of each type of defect on the interfacial heat transfer. Before ICMA no other modal analysis technique could incorporate the exact atomic positions in the calculations.

After the development of ICMA, it was applied to several interfaces. The results helped obtain a deeper understanding of the true mechanisms of heat transfer across the interface of two materials. A number of the important obtained insights can be summarized as follows:

- Although interfacial modes are localized and do not have a well-defined group velocity, they contribute significantly to the interface heat transfer. In fact, it was shown that only a small population of interfacial modes (*e.g.*, less 0.1% of the entire population of modes) at the interface of c-Si/c-Ge contribute directly more than 15% to the interfacial heat transfer.
- For all our examined interfaces, interfacial modes had the largest per mode contribution to the interfacial heat transfer.
- Using Landauer formalism, one can define a maximum theoretical limit for the heat transfer across interfaces. However, using ICMA, it was shown that interfacial heat transfer (*i.e.*, interface conductance) does not necessarily follow a maximum theoretical limit. In fact, several of our examined interfaces (*e.g.*, Si(m)/Si(4m), InP/InGaAs, and GaAs/Ge) showed conductance values even larger than the previously established maximum theoretical limit by the PGM.

7.2 Future directions

After developing ICMA and showing that it provides deeper insights into the interfacial heat transfer than other existing techniques, the future step would be to assess its predictive ability against experimental measurements. To this goal, two approaches can be followed. First is to experimentally measure the conductance across interfaces that ICMA has already provided predictions. Second is to apply ICMA to the interfaces for which experimental measurements already exist. In the following, the challenges in both approaches will be discussed.

7.2.1 Experimentally measuring the conductance across interfaces

Using ICMA, the TIC across several interfaces were examined in this thesis. However, as will be argued, experimental measurement of the TIC is a challenging task. The main challenge arises because TIR is generally much smaller than the other thermal resistances in the structure. For instance, for c-Si/a-SiO_2 interface structure shown in Figure 38a, in addition to the TIR, two other thermal resistances in the bulk of the materials are also present, and because of the small TIR values, the measurements by techniques such as 3-omega [2] will not be sensitive to the interface resistance to report any reliable TIC. The following quick calculation based on comparing the resistances in the bulk to the TIR can explain this more clearly. By assuming an average TIC of $G = 0.5 GWm^{-2}K^{-1}$ for c-Si/a-SiO_2 interface, the TIR would be $1/G = 2(nW)^{-1} m^2K^1$. The bulk thermal resistance is L/K, where L and K are the thickness and thermal conductivity of the material, respectively (for a-SiO_2, $K \approx 1 Wm^{-1}K^{-1}$ and for Si $K \approx 150 Wm^{-1}K^{-1}$). By choosing a 2nm thickness for a-SiO_2 layer, its thermal resistance can be lowered to the point that it becomes equal to the TIR; this is a very small thickness that by introducing additional uncertainties to the analysis complicates the calculations even further. Another option that can be envisioned is transfer bonding the Si layer on top of the a-SiO_2 substrate (*i.e.*, similar to silicon on insulator (SOI) technology). Now, a ~300nm thickness of Si results in a resistance equal to the TIR; this is a more reasonable thickness resulting in lower uncertainties. However, the quick analysis explained above merely provides a first guess, and the actual sensitivity analyses are much more involved. In fact, conducting those

rigorous sensitivity calculations shows that even if Si is transfer bonded to a-SiO_2 substrate, the sensitivity is still not large enough to extract any reliable TIC values.

In addition to 3-omega, other experimental techniques can also be utilized, such as time-domain thermoreflectance (TDTR) [155] and frequency domain thermoreflectance (FDTR).[120,156,157] However, for these techniques a transducer layer (Al for TDTR and Au for FDTR) should be grown on top of the structure shown in Figure 38a, which now transforms the interface of c-Si/a-SiO_2 to a *buried interface* (see Figure 38b). Measuring reliable TIC values for this buried interface (*i.e.*, $R_{int,1}$), is even more complicated, because the sensitivity is even lower than the previous structure (Figure 38a) due to the additional resistances (such as $R_{int,2}$ shown in Figure 38b) that are now introduced to the system.

The discussion above shows that new measurement techniques need to be devised to experimentally measure the TIC across different interfaces. For instance, by devising measurement techniques that do not require a transducer (*i.e.*, transducer less techniques), sensitivity to the desired interface can potentially be improved significantly. Such new measurement approaches are essential if further coupling between theory and experiment is desired, which is crucial in deepening our understanding of the interfacial heat transfer and ultimately realizing improved thermal management designs in future.

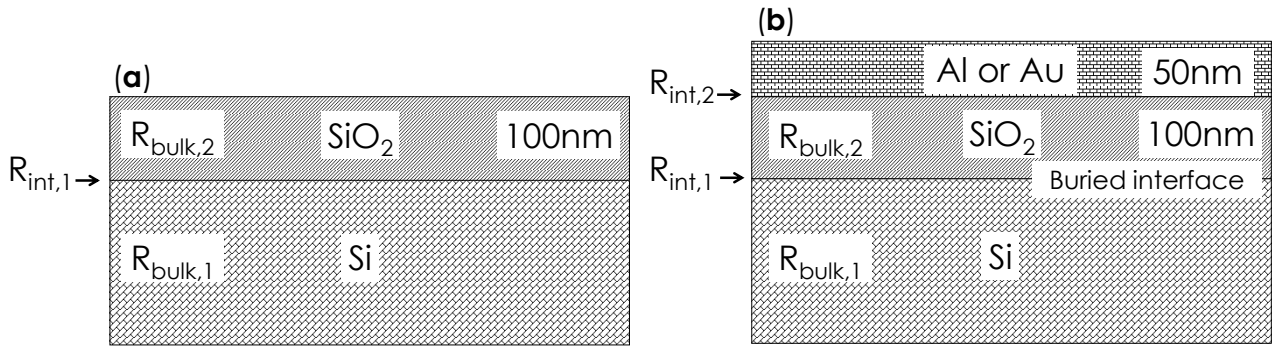

Figure 38 – Schematic for c-Si/a-SiO_2 interface structure that can be used for different experimental techniques such as (a) 3-omega and (b) TDTR and FDTR (with grown AL and Au transducers). $R_{int,1}$ the resistance across the c-Si/a-SiO_2 interface, and $R_{bulk,1}$ and $R_{bulk,2}$, and $R_{int,2}$ represent the resistances in the bulk of Si and SiO_2 and interface resistance across SiO_2/transducer interface, respectively.

7.2.2 Applying ICMA to interfaces for which experimental values exist

Another approach to validate ICMA is to apply it to interfaces for which experimentally measured TIC values already exist. Among the existing measurements that were previously shown in Figure 5, TiN/MgO [74] seems to be good a candidate for performing MD simulations, since it is a smooth interface (*i.e.*, epitaxially grown) between two lattice matched solids (both TiN and MgO have lattice constants equal to ~4.20A°). However, the problem here is that no accurate interatomic potentials exists for TiN, MgO and the interactions between them across the interface to perform the MD simulations needed for ICMA calculations.

To generate the needed interatomic potentials to conduct the required MD simulations, Atomistic, Simulation & Energy (A.S.E) Laboratory has developed an optimization code based on the genetic algorithm, termed phonon optimized potentials (POPs).[158] To use POPs, first quantum calculations are conducted on different atomic configurations for the material under study. Then, after the functional form for the

interatomic potential is chosen, POPs finds the best set of parameters in this functional form by directly fitting to the atomic forces, atomic energies, and atomic stress values that were obtained from the previously conducted quantum calculations. In this way, POPs can accurately obtain the quantum calculated properties from the much faster interatomic potentials, which are suitable for MD simulations. The reason that atomic forces, energies, and stress values were chosen to find the parameters in the functional form is that lowering the errors in predicting these values potentially results in the most accurate descriptions of (1) dispersion curve (*i.e.*, modes of vibration), (2) anharmonicity, and (3) stability in the system, which are three independent parameters that are crucial to having an accurate MD simulation.

After POPs is finalized in near future, not only it allows for generating the required interatomic potentials to validate ICMA against the existing experimental measurements, but also by having access to such a powerful code, interatomic potentials for almost any material can be accurately created; this ultimately allows ICMA to be applied to any interface that can be envisioned, which further expands the scientific and technological significance of the ICMA approach that was developed and utilized in this thesis.

REFERENCES

1 Cahill, D. G. *et al.* Nanoscale thermal transport. II. 2003–2012. *Applied Physics Reviews* **1**, 011305 (2014).

2 Cahill, D. G. *et al.* Nanoscale thermal transport. *J. Appl. Phys.* **93**, 793-818 (2002).

3 Kim, P., Shi, L., Majumdar, A. & McEuen, P. Thermal transport measurements of individual multiwalled nanotubes. *Phys. Rev. Lett.* **87**, 215502 (2001).

4 Yee, S. K., Malen, J. A., Majumdar, A. & Segalman, R. A. Thermoelectricity in fullerene–metal heterojunctions. *Nano Lett.* **11**, 4089-4094 (2011).

5 Catalan, G., Seidel, J., Ramesh, R. & Scott, J. F. Domain wall nanoelectronics. *Rev. Mod. Phys.* **84**, 119 (2012).

6 Pop, E. Energy dissipation and transport in nanoscale devices. *Nano Research* **3**, 147-169 (2010).

7 Tien, C.-L. & Chen, G. Challenges in microscale conductive and radiative heat transfer. *J. Heat Transfer* **116**, 799-807 (1994).

8 Min, C. *et al.* Thermal analysis and test for single concentrator solar cells. *Journal of Semiconductors* **30**, 044011 (2009).

9 Katz, E. A., Gordon, J. M. & Feuermann, D. Effects of ultra-high flux and intensity distribution in multi-junction solar cells. *Progress in photovoltaics* **14**, 297-304 (2006).

10 Minnich, A., Dresselhaus, M., Ren, Z. & Chen, G. Bulk nanostructured thermoelectric materials: current research and future prospects. *Energy & Environmental Science* **2**, 466-479 (2009).

11 Dove, M. T. *Introduction to lattice dynamics*. Vol. 4 (Cambridge university press, 1993).

12 Kapitza, P. The study of heat transfer in helium II. *J. Phys.(USSR)* **4**, 181-210 (1941).

13 Neeper, D. A. & Dillinger, J. Thermal resistance at indium-sapphire boundaries between 1.1 and 2.1 K. *Phys. Rev.* **135**, A1028 (1964).

14 Khalatnikov, I. M. *Teploobmen Mezhdu Tverdym Telom I Geliem-Ii. *Zhurnal Eksperimentalnoi I Teoreticheskoi Fiziki* **22**, 687-704 (1952).

15 Little, W. The transport of heat between dissimilar solids at low temperatures. *Can. J. Phys.* **37**, 334-349 (1959).

16 Hopkins, P. E., Norris, P. M. & Duda, J. C. Anharmonic phonon interactions at interfaces and contributions to thermal boundary conductance. *J. Heat Transfer* **133**, 062401 (2011).

17 Swartz, E. & Pohl, R. Thermal resistance at interfaces. *Appl. Phys. Lett.* **51**, 2200-2202 (1987).

18 Swartz, E. T. & Pohl, R. O. Thermal boundary resistance. *Rev. Mod. Phys.* **61**, 605 (1989).

19 Mingo, N. & Yang, L. Phonon transport in nanowires coated with an amorphous material: An atomistic Green's function approach. *Phys. Rev. B* **68**, 245406 (2003).

20 Zhang, W., Fisher, T. & Mingo, N. The atomistic Green's function method: An efficient simulation approach for nanoscale phonon transport. *Numer. Heat TR B-Fund.* **51**, 333-349 (2007).

21 Zhang, W., Mingo, N. & Fisher, T. Simulation of interfacial phonon transport in Si–Ge heterostructures using an atomistic Green's function method. *J. Heat Transfer* **129**, 483-491 (2007).

22 Mingo, N. in *Thermal nanosystems and nanomaterials* 63-94 (Springer, 2009).

23 Tian, Z., Esfarjani, K. & Chen, G. Enhancing phonon transmission across a Si/Ge interface by atomic roughness: First-principles study with the Green's function method. *Phys. Rev. B* **86**, 235304 (2012).

24 Young, D. & Maris, H. Lattice-dynamical calculation of the Kapitza resistance between fcc lattices. *Phys. Rev. B* **40**, 3685 (1989).

25 Sun, H. & Pipe, K. P. Perturbation analysis of acoustic wave scattering at rough solid-solid interfaces. *J. Appl. Phys.* **111**, 023510 (2012).

26 Zhao, H. & Freund, J. B. Phonon scattering at a rough interface between two fcc lattices. *J. Appl. Phys.* **105**, 013515 (2009).

27 Baker, C. H., Jordan, D. A. & Norris, P. M. Application of the wavelet transform to nanoscale thermal transport. *Phys. Rev. B* **86**, 104306 (2012).

28 Schelling, P., Phillpot, S. & Keblinski, P. Kapitza conductance and phonon scattering at grain boundaries by simulation. *J. Appl. Phys.* **95**, 6082-6091 (2004).

29 Schelling, P. K., Phillpot, S. R. & Keblinski, P. Phonon wave-packet dynamics at semiconductor interfaces by molecular-dynamics simulation. *Appl. Phys. Lett.* **80**, 2484-2486 (2002).

30 Roberts, N. A. & Walker, D. Phonon wave-packet simulations of Ar/Kr interfaces for thermal rectification. *J. Appl. Phys.* **108**, 123515 (2010).

31 Kakodkar, R. R. & Feser, J. P. A framework for solving atomistic phonon-structure scattering problems in the frequency domain using perfectly matched layer boundaries. *J. Appl. Phys.* **118**, 094301 (2015).

32 Kakodkar, R. R. & Feser, J. P. Probing the validity of the diffuse mismatch model for phonons using atomistic simulations. *arXiv preprint arXiv:1607.08572* (2016).

33 Chen, G. *Nanoscale energy transport and conversion: a parallel treatment of electrons, molecules, phonons, and photons*. (Oxford University Press, USA, 2005).

34 Zhang, Z. M. *Nano/microscale heat transfer*. (McGraw-Hill New York, 2007).

35 Landauer, R. Spatial variation of currents and fields due to localized scatterers in metallic conduction. *IBM J. Res. Dev.* **1**, 223-231 (1957).

36 Fourier, J. *Theorie analytique de la chaleur, par M. Fourier*. (Chez Firmin Didot, père et fils, 1822).

37 Narasimhan, T. Fourier's heat conduction equation: History, influence, and connections. *Proceedings of the Indian Academy of Sciences-Earth and Planetary Sciences* **108**, 117-148 (1999).

38 Itô, K. *Diffusion processes*. (Wiley Online Library, 1974).

39 Peierls, R. On the kinetic theory of thermal conduction in crystals. *Ann. Phys.(NY)* **3**, 1055-1101 (1929).

40 Uhlenbeck, G. E. & Ornstein, L. S. On the theory of the Brownian motion. *Phys. Rev.* **36**, 823 (1930).

41 Kittel, C. & McEuen, P. *Introduction to solid state physics*. Vol. 8 (Wiley New York, 1986).

42 Allen, P. B., Feldman, J. L., Fabian, J. & Wooten, F. Diffusons, locons and propagons: Character of atomie yibrations in amorphous Si. *Philos. Mag. B* **79**, 1715-1731 (1999).

43 Gordiz, K. & Henry, A. Phonon transport at interfaces: Determining the correct modes of vibration. *J. Appl. Phys.* **119**, 015101 (2016).

44 Gibbons, T., Bebek, M., Stanley, C. & Estreicher, S. Phonon-phonon interactions: First principles theory. *J. Appl. Phys.* **118**, 085103 (2015).

45 Estreicher, S., Gibbons, T. & Bebek, M. Phonons and defects in semiconductors and nanostructures: Phonon trapping, phonon scattering, and heat flow at heterojunctions. *J. Appl. Phys.* **115**, 012012 (2014).

46 Estreicher, S., Gibbons, T. & Bebek, M. Thermal phonons and defects in semiconductors: The physical reason why defects reduce heat flow, and how to control it. *J. Appl. Phys.* **117**, 112801 (2015).

47 Estreicher, S. K., Gibbons, T. M., Bebek, M. B. & Cardona, A. L. in *Solid State Phenomena*. 335-343 (Trans Tech Publ).

48 Seyf, H. R. & Henry, A. A method for distinguishing between propagons, diffusions, and locons. *J. Appl. Phys.* **120**, 025101 (2016).

49 Hopkins, P. E. Multiple phonon processes contributing to inelastic scattering during thermal boundary conductance at solid interfaces. *J. Appl. Phys.* **106**, 013528 (2009).

50 Hopkins, P. E. & Norris, P. M. Effects of joint vibrational states on thermal boundary conductance. *Nanosc. Microsc. Therm.* **11**, 247-257 (2007).

51 Prasher, R. Acoustic mismatch model for thermal contact resistance of van der Waals contacts. *Appl. Phys. Lett.* **94**, 041905-041905-041903 (2009).

52 Reddy, P., Castelino, K. & Majumdar, A. Diffuse mismatch model of thermal boundary conductance using exact phonon dispersion. *Appl. Phys. Lett.* **87**, 211908 (2005).

53 Shin, S., Kaviany, M., Desai, T. & Bonner, R. Roles of atomic restructuring in interfacial phonon transport. *Phys. Rev. B* **82**, 081302 (2010).

54 Minnich, A. J. Towards a microscopic understanding of phonon heat conduction. *arXiv preprint arXiv:1405.0532* (2014).

55 Duda, J. C., Beechem, T. E., Smoyer, J. L., Norris, P. M. & Hopkins, P. E. Role of dispersion on phononic thermal boundary conductance. *J. Appl. Phys.* **108**, 073515 (2010).

56 Stevens, R. J., Zhigilei, L. V. & Norris, P. M. Effects of temperature and disorder on thermal boundary conductance at solid–solid interfaces: Nonequilibrium molecular dynamics simulations. *Int. J. Heat Mass Transfer* **50**, 3977-3989 (2007).

57 Hopkins, P. E., Stevens, R. J. & Norris, P. M. Influence of inelastic scattering at metal-dielectric interfaces. *J. Heat Transfer* **130**, 022401 (2008).

58 Broido, D., Malorny, M., Birner, G., Mingo, N. & Stewart, D. Intrinsic lattice thermal conductivity of semiconductors from first principles. *Appl. Phys. Lett.* **91**, 231922 (2007).

59 Jain, A. & McGaughey, A. J. Strongly anisotropic in-plane thermal transport in single-layer black phosphorene. *Scientific reports* **5** (2015).

60 Garg, J., Bonini, N., Kozinsky, B. & Marzari, N. Role of disorder and anharmonicity in the thermal conductivity of silicon-germanium alloys: A first-principles study. (2011).

61 Dresselhaus, M. *et al.* New composite thermoelectric materials for energy harvesting applications. *JOM* **61**, 86-90 (2009).

62 Lindsay, L., Broido, D. & Reinecke, T. First-principles determination of ultrahigh thermal conductivity of boron arsenide: a competitor for diamond? *Phys. Rev. Lett.* **111**, 025901 (2013).

63 Esfarjani, K. & Stokes, H. T. Method to extract anharmonic force constants from first principles calculations. *Phys. Rev. B* **77**, 144112 (2008).

64 Chalopin, Y. & Volz, S. A microscopic formulation of the phonon transmission at the nanoscale. *Appl. Phys. Lett.* **103**, 051602 (2013).

65 Ong, Z.-Y. & Pop, E. Frequency and polarization dependence of thermal coupling between carbon nanotubes and SiO2. *J. Appl. Phys.* **108**, 103502 (2010).

66 Chalopin, Y., Mingo, N., Diao, J., Srivastava, D. & Volz, S. Large effects of pressure induced inelastic channels on interface thermal conductance. *Appl. Phys. Lett.* **101**, 221903 (2012).

67 English, T. S. *et al.* Enhancing and tuning phonon transport at vibrationally mismatched solid-solid interfaces. *Phys. Rev. B* **85**, 035438 (2012).

68 Mingo, N. Calculation of Si nanowire thermal conductivity using complete phonon dispersion relations. *Phys. Rev. B* **68**, 113308 (2003).

69 Gordiz, K. & Allaei, S. M. V. Thermal rectification in pristine-hydrogenated carbon nanotube junction: A molecular dynamics study. *J. Appl. Phys.* **115**, 163512 (2014).

70 Landry, E. & McGaughey, A. Thermal boundary resistance predictions from molecular dynamics simulations and theoretical calculations. *Phys. Rev. B* **80**, 165304 (2009).

71 Luo, T. & Lloyd, J. R. Enhancement of thermal energy transport across graphene/graphite and polymer interfaces: a molecular dynamics study. *Adv. Funct. Mater.* **22**, 2495-2502 (2012).

72 Zhong, H. L. & Lukes, J. R. Interfacial thermal resistance between carbon nanotubes: Molecular dynamics simulations and analytical thermal modeling. *Phys. Rev. B* **74** (2006).

73 Lindsay, L., Broido, D. & Mingo, N. Lattice thermal conductivity of single-walled carbon nanotubes: Beyond the relaxation time approximation and phonon-phonon scattering selection rules. *Phys. Rev. B* **80**, 125407 (2009).

74 Costescu, R. M., Wall, M. A. & Cahill, D. G. Thermal conductance of epitaxial interfaces. *Phys. Rev. B* **67**, 054302 (2003).

75 Hopkins, P. E., Phinney, L. M., Serrano, J. R. & Beechem, T. E. in *2010 14th International Heat Transfer Conference*. 313-319 (American Society of Mechanical Engineers).

76 Hopkins, P. E. *et al.* Effect of dislocation density on thermal boundary conductance across GaSb/GaAs interfaces. *Appl. Phys. Lett.* **98**, 161913 (2011).

77 Stoner, R. & Maris, H. Kapitza conductance and heat flow between solids at temperatures from 50 to 300 K. *Phys. Rev. B* **48**, 16373 (1993).

78 Lyeo, H.-K. & Cahill, D. G. Thermal conductance of interfaces between highly dissimilar materials. *Phys. Rev. B* **73**, 144301 (2006).

79 Beechem, T., Graham, S., Hopkins, P. & Norris, P. Role of interface disorder on thermal boundary conductance using a virtual crystal approach. *Appl. Phys. Lett.* **90**, 054104 (2007).

80 Hopkins, P. E. & Beechem, T. E. Phonon scattering and velocity considerations in the minimum phonon thermal conductivity of layered solids above the plateau. *Nanosc. Microsc. Therm.* **14**, 51-61 (2010).

81 Shen, S., Henry, A., Tong, J., Zheng, R. & Chen, G. Polyethylene nanofibres with very high thermal conductivities. *Nature nanotechnology* **5**, 251-255 (2010).

82 Dresselhaus, M. S. *et al.* New Directions for Low-Dimensional Thermoelectric Materials. *Adv. Mater.* **19**, 1043-1053 (2007).

83 Yang, R., Chen, G. & Dresselhaus, M. S. Thermal conductivity of simple and tubular nanowire composites in the longitudinal direction. *Phys. Rev. B* **72**, 125418 (2005).

84 Li, D. *et al.* Thermal conductivity of individual silicon nanowires. *Appl. Phys. Lett.* **83**, 2934-2936 (2003).

85 Yang, R. & Chen, G. Thermal conductivity modeling of periodic two-dimensional nanocomposites. *Phys. Rev. B* **69**, 195316 (2004).

86 Wu, X. & Luo, T. The importance of anharmonicity in thermal transport across solid-solid interfaces. *J. Appl. Phys.* **115**, 014901 (2014).

87 Rajabpour, A., Allaei, S. V. & Kowsary, F. Interface thermal resistance and thermal rectification in hybrid graphene-graphane nanoribbons: A nonequilibrium molecular dynamics study. *Appl. Phys. Lett.* **99**, 051917 (2011).

88 Hu, M., Keblinski, P. & Schelling, P. K. Kapitza conductance of silicon–amorphous polyethylene interfaces by molecular dynamics simulations. *Phys. Rev. B* **79**, 104305 (2009).

89 Kubo, R. The fluctuation-dissipation theorem. *Rep. Prog. Phys.* **29**, 255 (1966).

90 Puech, L., Bonfait, G. & Castaing, B. Mobility of the3He solid-liquid interface: Experiment and theory. *J. Low Temp. Phys.* **62**, 315-327 (1986).

91 Barrat, J.-L. & Chiaruttini, F. Kapitza resistance at the liquid—solid interface. *Mol. Phys.* **101**, 1605-1610 (2003).

92 Hardy, R. J. Energy-flux operator for a lattice. *Phys. Rev.* **132**, 168 (1963).

93 Henry, A. S. & Chen, G. Spectral phonon transport properties of silicon based on molecular dynamics simulations and lattice dynamics. *J. Comput. Theor. Nanos.* **5**, 141-152 (2008).

94 Chalopin, Y., Esfarjani, K., Henry, A., Volz, S. & Chen, G. Thermal interface conductance in Si/Ge superlattices by equilibrium molecular dynamics. *Phys. Rev. B* **85**, 195302 (2012).

95 Domingues, G., Volz, S., Joulain, K. & Greffet, J.-J. Heat transfer between two nanoparticles through near field interaction. *Phys. Rev. Lett.* **94**, 085901 (2005).

96 Henry, A. & Chen, G. High Thermal Conductivity of Single Polyethylene Chains Using Molecular Dynamics Simulations. *Phys. Rev. Lett.* **101** (2008).

97 Turney, J., McGaughey, A. & Amon, C. Assessing the applicability of quantum corrections to classical thermal conductivity predictions. *Phys. Rev. B* **79**, 224305 (2009).

98 Lv, W. & Henry, A. Direct Calculation of Modal Contributions to Thermal Conductivity via Green-Kubo Modal Analysis: Crystalline and Amorphous Silicon. *Accepted in New Journal of Physics* (2015).

99 Lv, W. & Henry, A. Direct calculation of modal contributions to thermal conductivity via Green–Kubo modal analysis. *New J. Phys.* **18**, 013028 (2016).

100 Lv, W. & Henry, A. Non-negligible contributions to thermal conductivity from localized modes in amorphous silicon dioxide. *Scientific reports* **6** (2016).

101 Rafii-Tabar, H. *Computational physics of carbon nanotubes*. (Cambridge University Press, 2008).

102 Rajabpour, A. & Volz, S. Thermal boundary resistance from mode energy relaxation times: Case study of argon-like crystals by molecular dynamics. *J. Appl. Phys.* **108**, 094324 (2010).

103 Sarkar, S. & Selvam, R. P. Molecular dynamics simulation of effective thermal conductivity and study of enhanced thermal transport mechanism in nanofluids. *J. Appl. Phys.* **102**, 074302 (2007).

104 Gordiz, K., Singh, D. J. & Henry, A. Ensemble averaging vs. time averaging in molecular dynamics simulations of thermal conductivity. *J. Appl. Phys.* **117**, 045104 (2015).

105 Gordiz, K. & Henry, A. A formalism for calculating the modal contributions to thermal interface conductance. *New J. Phys.* **17**, 103002 (2015).

106 Tersoff, J. Modeling solid-state chemistry: Interatomic potentials for multicomponent systems. *Phys. Rev. B* **39**, 5566 (1989).

107 Kosevich, A. M. Localization of Vibrations Near Extended Defects. *The Crystal Lattice: Phonons, Solitons, Dislocations, Superlattices, Second Edition*, 279-296.

108 Pike, E. R. & Sabatier, P. C. *Scattering, Two-Volume Set: Scattering and inverse scattering in Pure and Applied Science*. (Academic press, 2001).

109 Varadan, V. V. in *Acoustic, Electromagnetic and Elastic Wave Scattering-Focus on the T-Matrix Approach.* 33-59.

110 Cecchi, S. *et al.* Ge/SiGe Superlattices for Thermoelectric Devices Grown by Low-Energy Plasma-Enhanced Chemical Vapor Deposition. *J. Electron. Mater.* **42**, 2030-2034 (2013).

111 Wang, X. *et al.* Enhanced thermoelectric figure of merit in nanostructured n-type silicon germanium bulk alloy. *Appl. Phys. Lett.* **93**, 193121-193121-193123 (2008).

112 Landry, E. & McGaughey, A. Effect of interfacial species mixing on phonon transport in semiconductor superlattices. *Phys. Rev. B* **79**, 075316 (2009).

113 Huberman, S. C., Larkin, J. M., McGaughey, A. J. & Amon, C. H. Disruption of superlattice phonons by interfacial mixing. *Phys. Rev. B* **88**, 155311 (2013).

114 Sun, L. & Murthy, J. Y. Molecular dynamics simulation of phonon scattering at silicon/germanium interfaces. *J. Heat Transfer* **132**, 102403 (2010).

115 Li, X. & Yang, R. Effect of lattice mismatch on phonon transmission and interface thermal conductance across dissimilar material interfaces. *Phys. Rev. B* **86**, 054305 (2012).

116 Murakami, T., Hori, T., Shiga, T. & Shiomi, J. Probing and tuning inelastic phonon conductance across finite-thickness interface. *Applied Physics Express* **7**, 121801 (2014).

117 Plimpton, S. Fast parallel algorithms for short-range molecular dynamics. *J. Comput. Phys.* **117**, 1-19 (1995).

118 Gale, J. D. GULP: A computer program for the symmetry-adapted simulation of solids. *J. Chem. Soc., Faraday Trans.* **93**, 629-637 (1997).

119 Cahill, D. G., Goodson, K. & Majumdar, A. Thermometry and thermal transport in micro/nanoscale solid-state devices and structures. *J. Heat Transfer* **124**, 223-241 (2002).

120 Regner, K. T. *et al*. Broadband phonon mean free path contributions to thermal conductivity measured using frequency domain thermoreflectance. *Nature communications* **4**, 1640 (2013).

121 Padgett, C. W. & Brenner, D. W. Influence of chemisorption on the thermal conductivity of single-wall carbon nanotubes. *Nano Lett.* **4**, 1051-1053 (2004).

122 Gordiz, K. & Henry, A. Phonon Transport at Crystalline Si/Ge Interfaces: The Role of Interfacial Modes of Vibration. *Scientific Reports* **6** (2016).

123 Allen, P. B. & Feldman, J. L. Thermal conductivity of disordered harmonic solids. *Phys. Rev. B* **48**, 12581 (1993).

124 Larkin, J. M. & McGaughey, A. J. Predicting alloy vibrational mode properties using lattice dynamics calculations, molecular dynamics simulations, and the virtual crystal approximation. *J. Appl. Phys.* **114**, 023507 (2013).

125 Li, M., Zhang, J., Hu, X. & Yue, Y. Thermal transport across graphene/SiC interface: effects of atomic bond and crystallinity of substrate. *Appl. Phys. A*, 1-10.

126 Giri, A., Braun, J. L. & Hopkins, P. E. Effect of crystalline/amorphous interfaces on thermal transport across confined thin films and superlattices. *J. Appl. Phys.* **119**, 235305 (2016).

127 Giri, A., Hopkins, P. E., Wessel, J. G. & Duda, J. C. Kapitza resistance and the thermal conductivity of amorphous superlattices. *J. Appl. Phys.* **118**, 165303 (2015).

128 Gordiz, K. & Henry, A. Phonon transport at interfaces between different phases of silicon and germanium. *J. Appl. Phys.* **121**, 025102 (2017).

129 Gordiz, K. & Henry, A. Interface conductance modal analysis of lattice matched InGaAs/InP. *Appl. Phys. Lett.* **108**, 181606 (2016).

130 Custer, J. *et al.* Density of amorphous Si. *Appl. Phys. Lett.* **64**, 437-439 (1994).

131 Light, T. Density of" Amorphous" Ge. *Phys. Rev. Lett.* **22**, 999 (1969).

132 Deng, B., Chernatynskiy, A., Khafizov, M., Hurley, D. H. & Phillpot, S. R. Kapitza resistance of Si/SiO2 interface. *J. Appl. Phys.* **115**, 084910 (2014).

133 Jones, R. E. & Mandadapu, K. K. Adaptive Green-Kubo estimates of transport coefficients from molecular dynamics based on robust error analysis. *The Journal of chemical physics* **136**, 154102 (2012).

134 Alvarez, F., Díaz, C., Valladares, A. A. & Valladares, R. Radial distribution functions of ab initio generated amorphous covalent networks. *Phys. Rev. B* **65**, 113108 (2002).

135 Ruf, T. *et al.* Thermal conductivity of isotopically enriched silicon. *Solid State Commun.* **115**, 243-247 (2000).

136 Inyushkin, A., Taldenkov, A., Gibin, A., Gusev, A. & Pohl, H. J. On the isotope effect in thermal conductivity of silicon. *physica status solidi (c)* **1**, 2995-2998 (2004).

137 Kremer, R. *et al.* Thermal conductivity of isotopically enriched 28 Si: revisited. *Solid State Commun.* **131**, 499-503 (2004).

138 Ozhogin, V. *et al.* Isotope effect in the thermal conductivity of germanium single crystals. *Journal of Experimental and Theoretical Physics Letters* **63**, 490-494 (1996).

139 Cahill, D. G., Fischer, H. E., Klitsner, T., Swartz, E. & Pohl, R. Thermal conductivity of thin films: measurements and understanding. *Journal of Vacuum Science & Technology A* **7**, 1259-1266 (1989).

140 Cahill, D. G., Watson, S. K. & Pohl, R. O. Lower limit to the thermal conductivity of disordered crystals. *Phys. Rev. B* **46**, 6131 (1992).

141 Gordiz, K., Allaei, S. V. & Kowsary, F. Thermal rectification in multi-walled carbon nanotubes: A molecular dynamics study. *Appl. Phys. Lett.* **99**, 251901 (2011).

142 Duda, J. C. *et al.* Implications of cross-species interactions on the temperature dependence of Kapitza conductance. *Phys. Rev. B* **84**, 193301 (2011).

143 Gordiz, K. & Henry, A. Examining the Effects of Stiffness and Mass Difference on the Thermal Interface Conductance Between Lennard-Jones Solids. *Scientific reports* **5** (2015).

144 Stillinger, F. H. & Weber, T. A. Computer simulation of local order in condensed phases of silicon. *Phys. Rev. B* **31**, 5262 (1985).

145 Charache, G. *et al.* Infrared materials for thermophotovoltaic applications. *J. Electron. Mater.* **27**, 1038-1042 (1998).

146 Coutts, T. J. An overview of thermophotovoltaic generation of electricity. *Sol. Energy Mater. Sol. Cells* **66**, 443-452 (2001).

147 Tosi, A., Della Frera, A., Shehata, A. B. & Scarcella, C. Fully programmable single-photon detection module for InGaAs/InP single-photon avalanche diodes with clean and sub-nanosecond gating transitions. *Rev. Sci. Instrum.* **83**, 013104 (2012).

148 Ito, H., Furuta, T., Kodama, S. & Ishibashi, T. InP/InGaAs uni-travelling-carrier photodiode with 310 GHz bandwidth. *Electron. Lett.* **36**, 1809-1810 (2000).

149 Forrest, S., Kim, O. & Smith, R. Optical response time of In0. 53Ga0. 47As/InP avalanche photodiodes. *Appl. Phys. Lett.* **41**, 95-98 (1982).

150 Cederberg, J. *et al.* The development of (InGa) As thermophotovoltaic cells on InP using strain-relaxed In (PAs) buffers. *J. Cryst. Growth* **310**, 3453-3458 (2008).

151 Powell, D., Migliorato, M. & Cullis, A. Optimized Tersoff potential parameters for tetrahedrally bonded III-V semiconductors. *Phys. Rev. B* **75**, 115202 (2007).

152 Feng, T., Qiu, B. & Ruan, X. Anharmonicity and necessity of phonon eigenvectors in the phonon normal mode analysis. *J. Appl. Phys.* **117**, 195102 (2015).

153 Gill-Comeau, M. & Lewis, L. J. Heat conductivity in graphene and related materials: A time-domain modal analysis. *Phys. Rev. B* **92**, 195404 (2015).

154 Sääskilahti, K., Oksanen, J., Tulkki, J. & Volz, S. Role of anharmonic phonon scattering in the spectrally decomposed thermal conductance at planar interfaces. *Phys. Rev. B* **90**, 134312 (2014).

155 Cahill, D. G. Analysis of heat flow in layered structures for time-domain thermoreflectance. *Rev. Sci. Instrum.* **75**, 5119-5122 (2004).

156 Schmidt, A. J., Cheaito, R. & Chiesa, M. A frequency-domain thermoreflectance method for the characterization of thermal properties. *Rev. Sci. Instrum.* **80**, 094901 (2009).

157 Rodin, D. & Yee, S. K. Simultaneous measurement of in-plane and through-plane thermal conductivity using beam-offset frequency domain thermoreflectance. *Rev. Sci. Instrum.* **88**, 014902 (2017).

158 Rohskopf, A., Seyf, H. R., Gordiz, K. & Henry, A. Phonon Optimized Potentials. *arXiv preprint arXiv:1610.02353* (2016).